High Pressure Study of Magnetic Quantum Phase Transitions in Transition Metal Materials

Christopher W. Harrison

Royal Holloway and Bedford New College
University of London

A dissertation submitted to the University of London
for the degree of Doctor of Philosophy

September 2012

Declaration

This dissertation is the result of work carried out at the Department of Physics, Royal Holloway College, University of London, between September 2008 and September 2012. This Dissertation is my own work and contains nothing which is the outcome of work in collaboration with others, except as specified in the text and Acknowledgements. No part of this dissertation has been submitted for a degree, diploma or other qualification at this or any other university. The total length of this dissertation does not exceed one hundred thousand words.

Christopher W Harrison *September 2012*

Abstract

In this thesis magnetic materials are tuned towards quantum critical points by the application of hydrostatic pressure. A novel method for measuring magnetic susceptibility in a Bridgman anvil cell is developed, which allows for counterwound detection and compensation coils to be located within the sample space. This enables magnetic susceptibility to be measured up to 20 GPa with excellent signal to noise ratios. This technique along with electrical transport measurements have been used to study three magnetic d-metal materials. $FePt_3$ which shows two antiferromagnetic transitions at ambient pressure has been found to be very weakly pressure dependent. A pressure study of Mo_3Sb_7, a superconducting material with additionally reported antiferromagnetic order has shown an increase in the superconducting transition temperature from $T_c = 2.1 \pm 0.1$ K at zero pressure to $T_c = 3.4 \pm 0.1$ K at the highest pressure measured of 8.5 GPa. Measurements of single crystals of $NbFe_2$ under pressure have shown good agreement between the pressure phase diagram and the chemical composition phase diagram. A ratio for chemical substitution to pressure was determined to be $2.4 \pm 0.1 * 10^{-3}$ (%Nb)GPa^{-1}. In the tempreture dependence of the electric resistivity above 4 K non Fermi liquid type behaviour is seen over all pressures measured, up to the maximum pressure of 13 GPa.

Acknowledgements

I would firstly like to thank Dr. Philipp Niklowitz for giving me the opportunity to study for PhD and for his continuing supervision and motivation over the four years. I would like to thank Will for his influence, patience and guidance in the first few years of my PhD and to Terence for his huge help in the last stages. To Oliver who's support and advice in the lab was so greatly appreciated and to James for his help over the summer. To Dan, Rich and Dave for the countless discussions over cups of teas and games of chess. To Dan and Connor for being excellent house mates over the years. Many thanks to Uthay and Rais for all their advise. To my fellow members of Calgary '88, Chris, Jana, Aya, Steve and Neema thanks for all the great quizzing over the years. Thanks to all my other fellow PhD students at Royal Holloway Jim, Kris, Rob, Lev, Paco, Lawrence, Lorraine, Dan, Frankie, Will, Frank, George, Ray, Dave and Vish. Id like to thank my friends from Crowborough for their unfaltering friendship and support over the years. Finally I would like to thank my parents, my sister Emma and Tom for all their love and support.

Contents

List of Figures

Chapter 1

Introduction

1.1 Motivation

The suppression of the magnetic order eventually leads to a magnetic quantum phase transition [2], a transition between two ordered states at zero temperature. If these transitions are continuous it is called second order. A second-order phase transition at 0 K is called a quantum critical point (QCP) [3]. Around a QCP the behaviour of physical properties does not follow [4, 5, 6, 7, 8] what is expected from Landau's Theory of Fermi liquids [9]. For the last 50 years the Fermi liquid model has shaped our understanding of metallics systems and is often cited as the standard model of metals. Materials which show a breakdown of the Fermi liquid model, so called non-Fermi liquids are of great interest. With more than 50 known systems [10] the qualitative reasons for the breakdown are generally well understood. However, the specific quantum states which replace the Fermi-liquid remain in many cases unclear [11].

As a system is tuned to a quantum critical point novel phases may emerge. These can be centred above where a QCP would exist. The most common manifestation of a novel phase is superconductivity. This is often seen near the suppression of the antiferromagnetic state and occurs in a range of materials. Examples include heavy fermion systems [7], low-dimensional organic metals [12], alkali metal fullerides [13] and, the high-T_C iron pnictides [14] and iron chalcogenides [15].

Several examples of QPTs in heavy fermion systems are shown in Figure 1.1 with the image taken from [16].

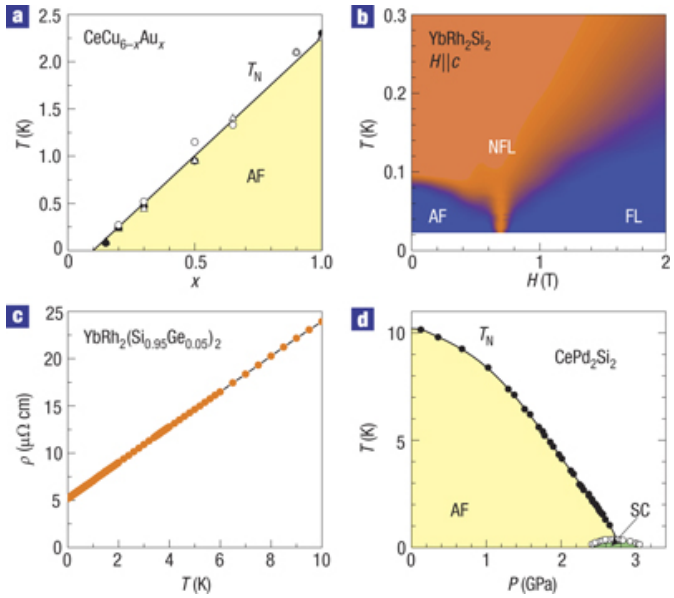

Figure 1.1: Examples of quantum phase transitions in several heavy fermions systems. (a) Shows $CeCu_{6-x}Au_x$, where chemical substitution induces an antiferromagnetic quantum critical point [17]. (b) Shows the field tuning of an antiferromagnetic transition (T_N = 70 mK) in $YbRh_2Si_2$ to a quantum critical point. Also shown are the exponent of the resistivity with colours indicating n=2, blue and n=1, orange [18], the latter indicating non-Fermi liquid behaviour. (c) shows a linear temperature dependence over three decades in Ge-doped $YbRh_2Si_2$ demonstrating robust non-Fermi liquid behaviour [18]. (d) shows emergent superconductivity in $CePd_2Si_2$ masking an antiferromagnetic quantum critical point [7].

In ferromagnetic systems second order phase transitions can be found at higher temperatures. However, if a ferromagnetic transition is tuned to zero temperature it is predicted to turn first order or to be masked by a magnetically modulated phase. In the first case, with the application of field, the ferromagnetic transition branches at a tricritical point and terminates at a quantum critical end point (QCEP). Superconductivity is less common in ferromagnetic materials however examples can be found in UGe_2 [19] (shown in Figure 1.2), UReGe [20], UIr [21] and, ϵ-Fe [22].

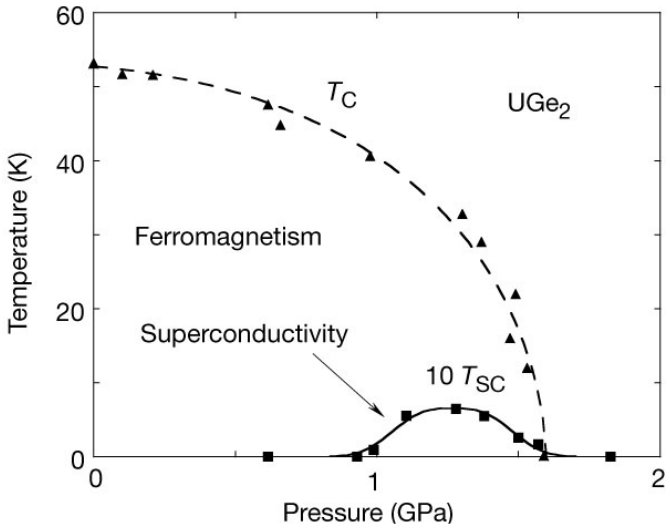

Figure 1.2: Phase diagram where emergent superconductivity appears near a ferromagnetic quantum phase transition in UGe_2 [19].

1.2 Materials

Studies on range of magnetic transition metal materials are presented in this thesis. These materials are $FePt_3$, Mo_3Sb_7 and, $NbFe_2$.

1.2.1 $FePt_3$

$FePt_3$ is a fcc alloy that undergoes two antiferromagnetic transitions. Through measuring the pressure dependence of this system it offers the opportunity to study the evolution of two different antiferromagnetic states with the hope of suppressing the transitions to a quantum critical point. If superconductivity was to emerge this would be an example of the missing case of an antiferromagnetically induced superconductor in a cubic d-electron system.

1.2.2 Mo_3Sb_7

Mo_3Sb_7 is a superconducting material which has a critical temperature of $T_c = 2.1$ K but apparently shows no magnetic order at zero pressure. Recent low pressures studies up to

2.2 GPa [23] on Mo_3Sb_7 have however indicated the appearance of a spin density wave transition at $T_{SDW} = 6.7\ K$ (the evolution up to the maximum pressure involves a small increase in the critical temperature and a decrease in the spin density wave transition temperature). By increasing the range of the temperature-pressure phase diagram the relationship between the spin density wave and superconductivity can be clarified.

1.2.3 $NbFe_2$

The approach to a ferromagnetic quantum phase transition has typically been accompanied by a change from second order to first order. Another possible scenario consists on the ferromagnetic quantum critical point being masked by a long wavelength spiral phase. $NbFe_2$ is a candidate material for this so far unobserved scenario.

$NbFe_2$ when doped with either small amounts of Nb or Fe ($Nb_{1-y}Fe_{2+y}$) has been extensively studied with polycrystalline samples and shows a rich and complex phase diagram, which is shown in Figure 1.2.3. For compositions $y > 0.02$ the system is an Ising ferromagnet and for $y < -0.02$ a Heisenberg ferromagnet. Around stoichiometry an unknown magnetic phase with a potential long range helical structure is observed.

1.3 High Pressure as a Tuning Mechanism

High pressure is an important control parameter for the tuning of electronic properties of materials. For a material that undergoes no structural transitions, pressure affects predominantly the inter-atomic distances. This is in contrast to other tuning methods; chemical substitution, which causes disorder and shifts the Fermi level and magnetic field, which breaks time-reversal symmetry. The realisation of high pressure hydrostatic measurements is demanding because achieving high pressures either requires small sample volumes or bulky equipment. In this thesis small Bridgman anvil cells are used which have been designed to be easily mounted within a cryogenic fridge and the bore of high field magnets. To allow measurements up to 20 GPa sample spaces of less than 0.08 mm^3 are required creating many technical difficulties in performing physical property measure-

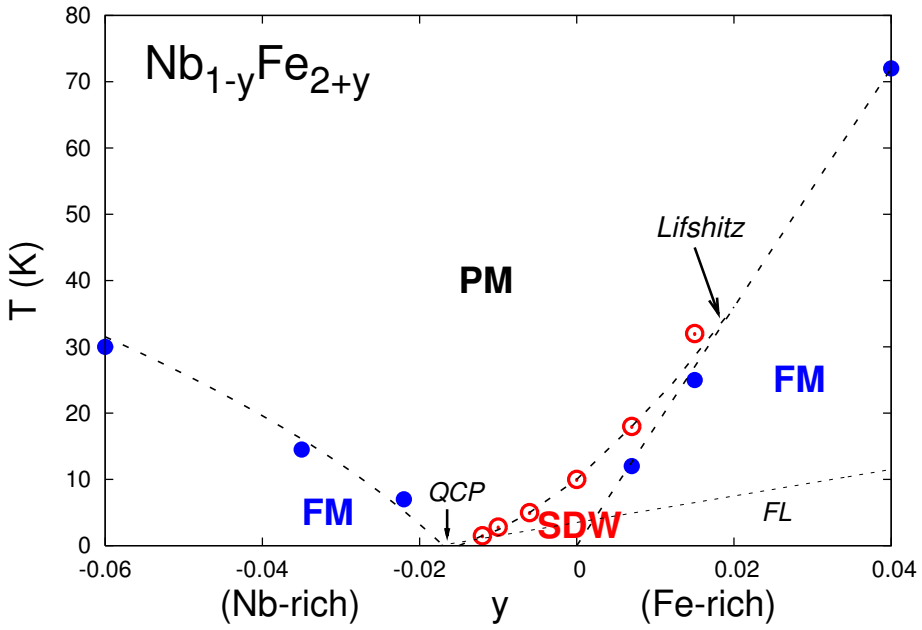

Figure 1.3: Phase diagram of $NbFe_2$ developed from the measurement of multiple polycrystalline materials [24].

ments. Resistivity and heat capacity measurements using a solid pressure medium have been realised. Furthermore, a technique, to measure magnetic susceptibility in a liquid pressure medium with a pair of counter-wound coils within the sample space, has been developed.

Chapter 2

Theoretical Concepts

2.1 Fermi Gas Model

The Fermi gas model is a basic description of metals consisting of non-interacting fermions trapped within an infinite potential well. In metallic systems where the number of electrons is of the order of 10^{23} there are many finely spaced energy levels called bands. In the ground state of the system ($T = 0$ K) the highest occupied state is known as the Fermi energy, E_F. This is typically of the order of 10000 K for transition metals and $10 - 100$ K for some heavy-fermion metals. In momentum space the area which separates the highest occupied state from the lowest unoccupied state is known as a Fermi Surface. For the free-electron model the Fermi surface is a sphere, however as electron-ion interactions are taken into account the shape will become contorted. These characteristics are often used to predict the thermal, electrical, magnetic, and, optical properties of metals. Excitations are created by the promotion of a fermion from just below the Fermi surface to just above it, creating an particle-hole excitation. These two states have uniquely labeled quantum numbers for the spin and momentum. Only electrons within the energy range of $\mathrm{k}_B T$ or $\mu_B H$ of the Fermi surface can contribute to the specific heat and to the magnetisation of the system. These give the low temperature physical properties for the heat capacity and magnetic susceptibility with a linear response expected in the heat capacity and a constant for the inverse of the magnetic susceptibility.

2.1.1 Fermi Liquid Theory

The Fermi gas model prediction (linear response of the heat capacity and the inverse magnetic susceptibility being a constant) for the low temperature properties are observed in most metals however with a smaller magnitude. The experimentally observed quadratic dependence of the electrical transport is not seen in the Fermi gas model. To improve on this Landau proposed that electron-electron interactions were included as a perturbation to the Fermi gas model [9]. The theory rests on the concept of adiabatic continuity. This states that on a gradual increase of the perturbation to the system, the eigenstates of the system change however the quantum numbers associated with the eigenstates are robust. These quantum numbers are not to be associated with electrons but with quasi-particles, renormalised electrons which can have an effective mass many times larger than that of the non-interacting electron and finite lifetimes.

Figure 2.1 shows the occupation probability in reciprocal space for a non-interacting Fermi gas at 0 K and for an interacting Fermi liquid. The quantity $Z_{\mathbf{k}}$ is the quasiparticle weight and is related to the size of the step occurring at the Fermi energy. The correlation enhancement of the effective mass is predicted to be[25],

$$\frac{1}{Z_{\mathbf{k}}} = \left(\frac{m^*}{m}\right)_{corr}. \tag{2.1}$$

As $Z_{\mathbf{k}} \to 0$ the Fermi liquid begins to break down, for example due to an enhancement of the long range interactions. This happens for example around a second order magnetic quantum critical point where there is a divergence in the magnetic correlation length and the quasiparticle scattering cross section.

2.2 Magnetism

The various forms of magnetic order magnetism can be broadly split into two categories, consisting of localised or itinerant magnetic moments. In the localised case the magnetic moments are associated with a particular atom whereas in the itinerant case the magnetic

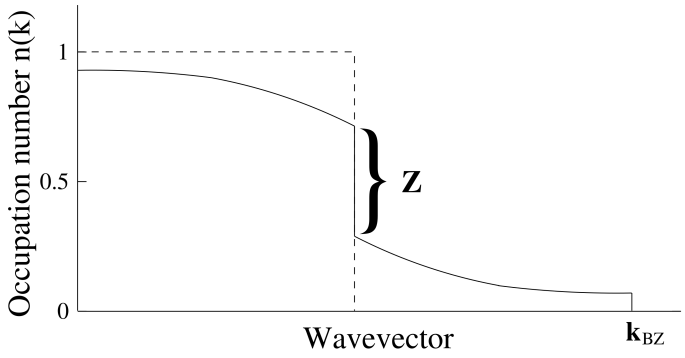

Figure 2.1: Occupation of states for a non-interacting Fermi gas (dashed line) and an interacting Fermi Liquid (solid line). In the case of the interacting Fermi liquid the step at the Fermi surface has been reduced, corresponding to the reduced quasiparticle weight, $Z_{\mathbf{k}}$ [26].

moments are considered to be spatially extended. The interesting magnetic properties of the rare earth and transition elements derive from the materials filled subshells having a greater spatial extent than that of their unfilled subshells. This is especially true of the rare earth materials whose incomplete 4f shells lie significantly deeper than the outer 6s shell thus many of the atomic characteristics remain unchanged. In this way 4f rare earth compounds can exhibit properties associated with localised magnetism. For transition metal materials the unfilled 3d shell lies spatially within the outer 4s shell and have significant overlapping wavefunctions with neighbouring atomic sites. This gives a significant probability of the electrons being associated with neighbouring atoms and therefore 3d (and to lesser extents 4d and 5d) transition metal compounds are best described using an itinerant picture.

2.2.1 Localised Model

To describe the emergence of ferromagnetism in a localised picture a mean field theory is used. A lattice of magnetic moments are coupled together with an exchange field. In the

non-interacting case the magnetic suscieptibility has the Curie form of paramagnetism,

$$\chi = \frac{M}{H} = \frac{\mathsf{C}}{T}, \tag{2.2}$$

with the Curie constant, C= $n_a \mu_B^2 \mu_{eff}^2$ with n_a the number of magnetic ions per unit volume and μ_{eff} is the effective paramagnetic magnetic moment. The interacting case term is modeled by adding a term for the internal magnetic field, which is proportional to the magnetisation, $H_{int} = \lambda M$, where λ is an exchange constant. The magnetic susceptibility is now found to be,

$$\chi = \frac{M}{H + \lambda M} = \frac{\mathsf{C}}{T}. \tag{2.3}$$

Therefore,

$$\chi = \frac{\frac{\mathsf{C}}{T}}{1 - \lambda\left(\frac{\mathsf{C}}{T}\right)}. \tag{2.4}$$

Comparing Equation 2.2 and 2.4 an enhancement in the magnetic susceptibility is seen by a factor of $\frac{1}{1-\lambda \mathsf{C}/T}$. The model breaks down and leads to long range magnetic order when $T \leq \lambda \mathsf{C}$

2.2.2 Stoner Model

Stoner model describes how ferromagnetism can be energetically favorable in an itinerant system. The non-interacting system starts with an equal number of spin up and spin down electrons. A spin inbalance is defined as

$$\Delta N = \frac{n_\downarrow - n_\uparrow}{N}, \tag{2.5}$$

where $n_{\downarrow,\uparrow}$ are the density of down and up spins and N the total number of spins. The magnetisation of the system can be expressed as $M = \frac{N}{V}\Delta N \mu_B$. The energy change compared to the non-interacting for state for the spin up and spin down electrons is then given by

$$E_{\uparrow,\downarrow}(k) = \tilde{E}(k) \mp \frac{I_S \Delta N}{2}, \tag{2.6}$$

where I_S is Stoner parameter and describes energy reduction due to electron spin correlations. $\tilde{E}(k)$ is given by

$$\tilde{E}(k) = E(k) - \frac{I_S(n_\downarrow + n_\uparrow)}{2N}. \tag{2.7}$$

The change in spins can be expressed as

$$\Delta N = \frac{1}{N}\sum_k f_\uparrow(k) - f_\downarrow(k), \tag{2.8}$$

where

$$f_{\uparrow,\downarrow} = \left[\exp\left(\tilde{E}(k) \mp \frac{I_S\Delta N}{2} - \frac{E_f}{k_B T}\right)\right]^{-1}, \tag{2.9}$$

are the Fermi-Dirac distributions for the up and down pin electrons, respectively. Performing a Taylor expansion of Equation 2.8 (assuming ΔN is small) gives

$$\Delta N = -\frac{1}{N}\sum_k \frac{\partial f(k)}{\partial \tilde{E}(k)}\left(I_S\Delta N\right) - \frac{1}{24N}\sum_k \frac{\partial^3 f(k)}{\partial \tilde{E}(k)^3}\left(I_S\Delta N\right)^3 + \ldots. \tag{2.10}$$

The sum of Equation 2.10 may be expressed as

$$\frac{\partial f(k)}{\partial \tilde{E}(k)} = \frac{V}{(2\pi)^3 N}\int dk \left(\frac{\partial f(k)}{\partial \tilde{E}(k)}\right) \tag{2.11}$$

$$= \frac{V}{(2\pi)^3 N}\int dk \left(-\delta\left(\tilde{E} - E_F\right)\right) \tag{2.12}$$

$$= -\frac{V}{2}D(E_F), \tag{2.13}$$

$$\tag{2.14}$$

Where $D(E_F)$ is the density of states at the Fermi surface. The density of states per atom per spin is therefore given by,

$$\tilde{D}(E_F) = \frac{V}{2N}D(E_F). \tag{2.15}$$

This may then be substituted back in to Equation 2.10 to give.

$$\Delta N = \tilde{D}(E_F) I_S \Delta N - \mathcal{O}^3 \tag{2.16}$$

Rearranging gives

$$\Delta N \left(1 - \tilde{D}(E_F) I_S\right) = -\mathcal{O}^3, \tag{2.17}$$

For $\Delta N > 0$ this means that $1 - \tilde{D}(E_F) I_S < 0$ or

$$\tilde{D}(E_F) I_S > 1. \tag{2.18}$$

This is the stoner criterion for ferromagnetism

2.3 Beyond Fermi-Liquid Theory

Fermi liquid theory relies on the continuous adiabatic from the bare electron ground state when an interaction field is gradually turned on. When the interactions become too strong or too long range Fermi liquid theory breaks down. This means the electron interactions become so dominant that they not only lead to a quantitative change in the properties but also a qualitatively different behaviour. There are many variants of the break down of Fermi liquid behaviour, for example the Luttinger liquid, the marginal Fermio liquid which is expected mear a quantum criticality.

2.3.1 Quantum Criticality

A classical phase transition occurs between two states at finite temperature. A phase transitions at zero temperature between two ordered states is a quantum phase transitions. A graphical representation of an itinerant second order quantum phase transition is shown in Figure 2.3.1. The position at which the ordered state is suppressed to 0 K is the quantum critical point (QCP). A non-thermal ordering parameter is used to drive the system through the two ordered states for example the charging energy in a Josephson-junction array, the magnetic field in a quantum Hall sample.

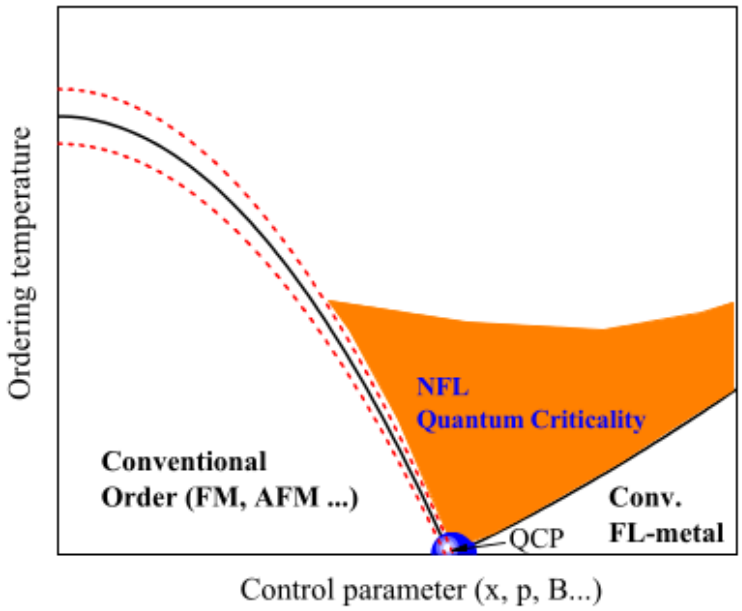

Figure 2.2: A diagram showing a quantum phase transition between two ordered states. Also shown are the quantum critical region (orange) and classical critical region (red dotted line).

At non-zero temperature, phase transitions are accompanied by a divergence of the correlation length and the correlation time, this is to say that the order parameter fluctuates coherently over increasing distance and ever more slowly as the phase transition is approached. These fluctuations are characterised by a frequency ω^* which tends to zero as the phase transition is approached. This means that a quantum system will behave classically at a phase transition since the temperature will exceed all frequencies of interest, $k_B T_c \gg \hbar\omega^*$. At a quantum phase transitions , where $T_c = 0$ this is no longer the case and as sch the system may no longer be described classically.

Spin Fluctuation Model

A number of investigators have considered the physical properties of metals at a quantum phase transition [27, 28, 29, 30]. Though these models define the system at 0 K, at temperatures significantly close to the quantum phase transition the behaviour of the system is still defined by quantum criticality [31]. One of these models is the spin fluctuation model, which describes magnetic fluctuations in a near magnetic system. Though initially used for ferromagnetic systems this model can be extended for systems with small ordering wavevectors, $\boldsymbol{Q}$.

It has been shown in the limit that the transition temperature converges to zero this model is a good quantum theory of the critical phenomena [27, 28]. The treatment here follows the 'Magnetic Electron' by G.G. Lonzarich [32].

To simplify the model, only fluctuations with a frequency, ω and wavevector, q below certain cutoffs, $\omega < \omega_c$ and $q < q_c$ are considered. In this case, ω_c and q_c are assumed to be small compared to the Fermi energy and the Brillouin zone. It is these relatively slow large amplitude fluctuations that give rise to the singular properties of the quasiparticles.

Scalar Dynamic Field

We begin with a Ginzburg-Landau postulate of the field equation and consider an applied spacially varying but static magnetic field, $H(\mathbf{r})$ of the form

$$H(\mathbf{r}) = H[M] = aM(\mathbf{r}) + bM^3(\mathbf{r}) - c\nabla^2 M(\mathbf{r}), \tag{2.19}$$

where square brackets are used to imply the mapping of $(\mathbf{r})$ from one function to another. In Equation 2.19 $a = a_0 - \lambda$, where a_0 is te inverse Pauli susceptibility,χ_0 and λ is a phenomenological constant known as the exchange field parameter. a leads to an enharncement of the susceptibility of the form $\chi = a^{-1} = \chi_0/(1-\lambda\chi_0)$. c is a measure of the resistance of the system to spatial variations in $M(\mathbf{r})$ (and is positive for ferromagnets). It is useful at this point to define an effective field, $H_{eff} = H - H[M]$, where H is the allied field and $H[M]$ is the right hand side of equation 2.19. In the paramagnetic state it is expected that M will relax towards equilibrium, given by $H_{eff} = 0$. For small H_{eff} and slow variations, the time dependence of the magnetisation is postulated by the spatial convolution of effective field

$$\gamma * H_{eff}, \tag{2.20}$$

where $*$ denotes a spatial convolution and $\gamma(\mathbf{r})$ is the relaxation function. Taking the Fourier transform of equation 2.20 leads to the following expression,

$$H_{\mathbf{q},\omega} = \chi^{-1}_{\mathbf{q},\omega} M_{\mathbf{q},\omega}, \tag{2.21}$$

where

$$\chi^{-1}_{\mathbf{q},\omega} = \chi^{-1}_{\mathbf{q}} \left(1 - i\frac{\omega}{\Gamma_{\mathbf{q}}}\right), \tag{2.22}$$

$$\chi^{-1}_{\mathbf{q}} = \chi^{-1} + c\mathbf{q}^2, \tag{2.23}$$

$$\Gamma_{\mathbf{q}} = \gamma_{\mathbf{q}} \chi^{-1}_{\mathbf{q},\omega}. \tag{2.24}$$

Where $\Gamma_{\mathbf{q}}$ is the relaxation spectrum and can be interpreted as the rate at which a component of $M_{\mathbf{q}}(t)$ will relax to the equilibrium $H = 0$. $\chi^{-1}_{\mathbf{q},\omega}$ is the generalised linear susceptibility defined as $M_{\mathbf{q},\omega}/H_{\mathbf{q},\omega}$. This reduces to $\chi^{-1}_{\mathbf{q}}$ as $\omega \to 0$, the wavevector dependent susceptibility. χ^{-1} is the susceptibility when $\mathbf{q}$ and $\omega \to 0$. It is assumed $\gamma_{\mathbf{q}} = \gamma q^{-1}$ for low $\mathbf{q}$ where n=1 for ferromagnets and paramagnets and n=0 for systems with large $\mathbf{Q}$

Thermal Properties

In order to determine the physical properties a consideration of the thermal affects on the fluctuations is needed. This is achieved by modeling the system as an overdamped harmonic oscillator where the susceptibility is the response function. Invoking the fluctuation dissipation theorem, which relates the variance of the local magnetisation, $\bar{m}^2$, to the imaginary part of the susceptibility, given by

$$\bar{m}^2 = \frac{2}{\pi}\int_0^{\inf} d\omega \left(\frac{1}{2} + n_\omega\right) \Im\chi_\omega, \tag{2.25}$$

where n_ω is the Bose function, given by $\left(\mathsf{e}^{\hbar\omega/k_B T} - 1\right)$. This expression holds for an arbitrary field in the presence of anharmonicities. From the thermal part of the local magnetisation, $\bar{m}^2_T$, the dimensionless thermal population $n(\Gamma/T)$ can be obtained, which is used for the determination of the temperature dependence of the physical properties. This is given by

$$n(\Gamma/T) = \frac{\bar{m}^2_T}{\Gamma_\alpha} = \frac{2}{\pi}\int_0^{\inf} d\omega n_\omega \frac{\omega}{(\omega^2 + \Gamma^2} \tag{2.26}$$

$$\approx \frac{T}{\Gamma(1 + (3\Gamma/\pi T))} \tag{2.27}$$

$$\tag{2.28}$$

Table 2.1: The power law exponents for physical properties of itinerant systems derived from Fermi liquid theory and spin fluctuation theory(SFT).

	Fermi Liquid	SFT FM (3D)	SFT FM (2D)	SFT AFM (3D)
Resistivity	T^2	$T^{5/3}$	$T^{4/3}$	$T^{3/2}$
Inverse Susceptibility	const.	$T^{4/3}$	T	3/2
Heat Capacity	γT	$-T\ln T$	$T^{4/3}$	$T^{1/2} - T^{3/2}$

General Form of the Low Temperature Exponents

Using the dimensionless population, Equation 2.26 and the entropy of the overdamped oscillator, expressions for the change in susceptibility, heat capacity and resistivity and be found in the form,

$$\partial\chi^{-}1 = \partial a = 5b\sum_{\mathbf{q}} \gamma_{\mathbf{q}} n_{\mathbf{q}} = 5b\sum \gamma_{\mathbf{q}} n\left(\frac{\gamma_{\mathbf{q}}}{T}(a + \Delta a + c\mathbf{q}^2)\right), \tag{2.29}$$

$$\Delta C = \frac{3}{2}\sum_{\mathbf{q}} \Gamma_{\mathbf{q}} \frac{\partial n_{\mathbf{q}}}{\partial T}, \tag{2.30}$$

$$\partial\rho = \eta\sum_{\mathbf{q}} \mathbf{q}^k \left(\frac{T\partial n_{\mathbf{q}}}{\partial T}\right)_{\Gamma}, \tag{2.31}$$

where $k = 2$ is for ferromagnetic fluctuations and $k = 0$ for antiferromagnetic fluctuations. These equations may be solved for two different limits of $\Gamma_{\mathbf{q}}$, either close to a critical point or far away from one. For the latter the results reassuring produce the same exponens as the Fermi liquid model. In the former case the exponents are dependent on both the type of fluctuations as well as the dimensionality of the system. The results for both sets of exponents are presented in Table 2.3.1.

2.3.2 Quantum Criticality in Ferromagnetic Materials

Ferromagnetic phase diagrams differ from those of itinerant antiferromagnetic second order quantum phase transitions, 2.3.2 (a). To date there have been no reports of a second

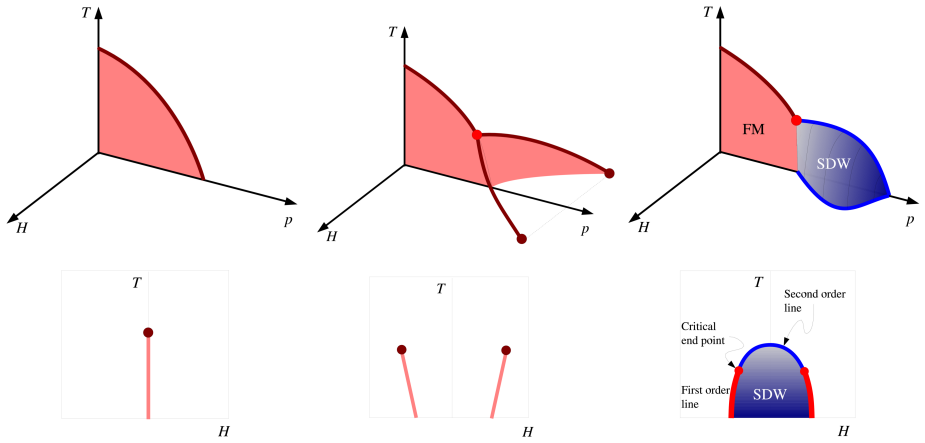

Figure 2.3: Possible phase diagrams for Ferromagnetic materials [1].

order itinerant ferromagnetic quantum phase transitions. Instead as the second order ferromagnetic phase transition reaches low temperature it turns first order, as shown in Figure 2.3.2 (b). This coincides with the appearance of second order branches in magnetic field emerging from a tricritical point (TCP). Below these transitions in magnetic field are sheets of 1st order metamagnetic transitions. This phase diagram is seen in many materials such as Ni_3Al [33], $ZrZn_2$ [34] and, UGe_2 [35].

Another possibility for the phase diagram of ferromagnetic materials [36] is that of a long range magnetic helical spiral order than masks the QCP, 2.3.2(c). This scenario not yet been observed experimentally however $NbFe_2$ is a potential candidate material.

2.3.3 Superconductivity

Superconductivity, the dissipationless flow of electrons is one of the most dramatic breakdowns of the Fermi-liquid theory. This occurs when there is a net quasiparticle-quasiparticle attraction from the effective interaction potential such that pairs of quasiparticles form bound bosonic states, called Cooper pairs. These may then be described by Bose-Einstein statistics. The condensation of the Cooper pairs below a critical temperature, T_c gives rise to superconductivity.

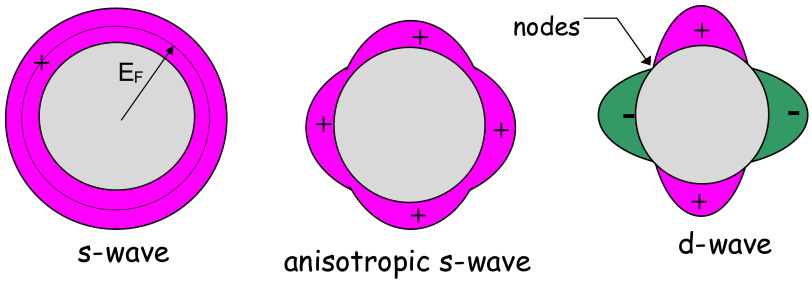

Figure 2.4: Examples of the order parameter symmetry for s-wave, anisotropic s-wave and d-wave superconductivity [39].

The best established and understood method for the mediation of superconductivity is via electron-phonon interactions, described by BCS (Bardeen, Cooper and Schrieffer) theory [37], referred to as conventional superconductivity. In this case electrons near the Fermi surface pair with electrons with opposite spin and crystal momentum, forming a spin singlet s-wave state.

The difference between conventional superconductivity and unconventional superconductivity is how this model is treated further. For the conventional s-wave superconductor the wavefunction is homogeneous in momentum space, this gives a spherical symmetry of gap and wavefunction in reciprocal space. An s-wave, an anisotropic s-wave and, d-wave symmetry are shown in Figure 2.4. For unconventional superconductivity, where the crystal lattice is often anisotropic the pair wavefunction can be directional. An example is a d-wave superconductor which exhibits nodes and a sign change in reciprocal space. The mechanism for pairing in unconventional superconductors are still controversial however it is assumed to arise from strong electron correlations. One such candidate is spin fluctuations [38]

Chapter 3

Experimental Techniques

This chapter provides an overview of the experimental techniques developed and used in this thesis. The chapter has four main sections of this chapter cover cryogenics, ambient pressure measurement techniques, a description of high pressure techniques for measuring resistivity and heat capacity and finally improvements made in magnetic susceptibility techniques. Recent high pressure susceptibility setups included the pick-up coil in the sample space to increase the filling factor. In this work it has been achieved to additionally include a counterwound compensation coil in the sample space. The new technique allows to better reduce the background in the susceptibility signal.

3.1 Cryogenics

All the measurements shown in this thesis were performed on a Physical Property Measurement System (PPMS) from Quantum Design incorporating a bidirectional sample magnet with a maximum field of 9 T. The PPMS is a ^{4}He cryostat which operates from a base temperature of 1.8 K via ^{4}He pot to a maximum temperature of 400 K. Heating and cooling can be controlled to within 0.01 K min^{-1}. Thermal conductivity to the samples is provided by exchange gas and a direct thermal coupling at the base of the sample chamber. Temperature is measured via two thermometers at the base of the sample chamber, a platinum thermometer for measuring temperature above 50 K and a cernox thermometer

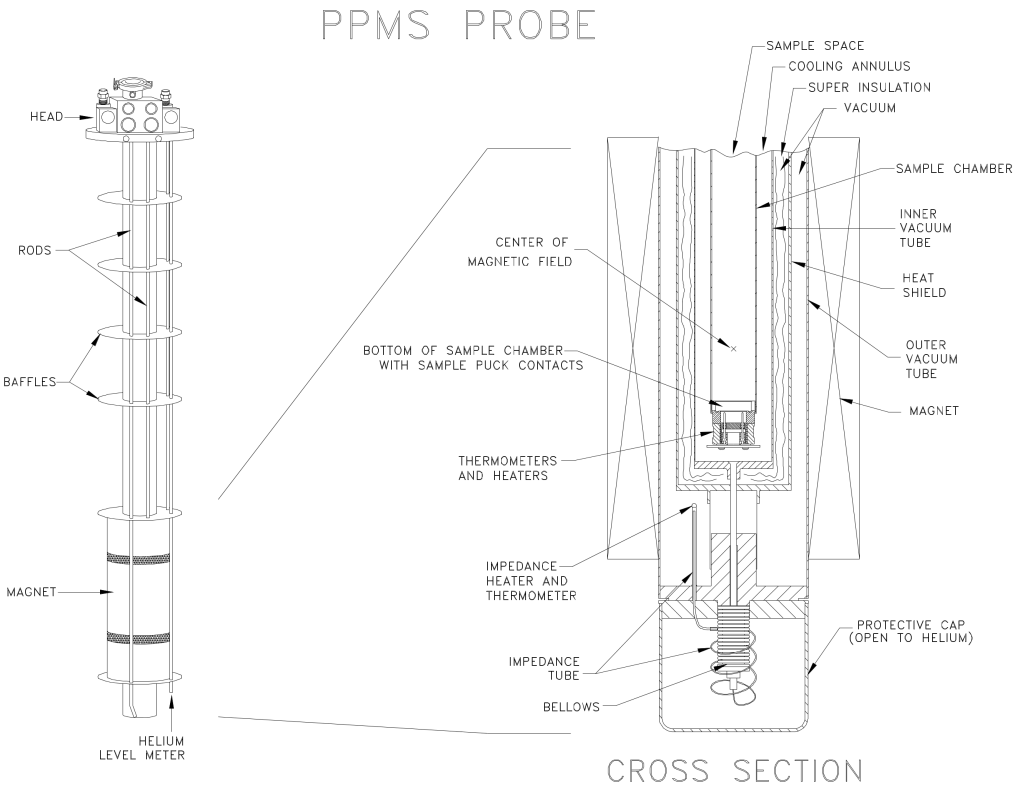

Figure 3.1: Diagram of the PPMS sample chamber and magnet [40]. The figure on the left shows the head of the sample probe where the electrical connections are made and where access to the sample space. At the base of the probe is the 9 T magnet and the porous protective cap. The right hand figure shows a cutaway of the magnet showing the bottom of the sample tube with a typical sample puck installed.

for measuring temperatures below 100 K, temperatures between 50 K and 100 K use a weighted function of the two thermometers. A further platinum thermometer located half way up the sample chamber is used for stabilisation purposes. The field dependence of these thermometers has been calibrated by Quantum Design with accuracy of the thermometry reported as $\pm 0.5\%$ [40]. A diagram of the PPMS sample chamber is shown in Figure 3.1.

3.2 Ambient Pressure Measurement Techniques

3.2.1 Resistivity

Resistivity measurements were carried out using a four point method with an alternating current. Four gold wires with 25 µm diameter are spot welded in series across the samples. Only a low current is sent through the outer two contacts, to avoid heating. The voltage is measured using the inner two contacts. For a voltmeter with an ideal infinite impedance no contact resistance would be measured using this technique. A Lock-in amplifier was used for all measurements and a frequency selected producing low noise. For most measurements 23 Hz was selected.

Power law analyses

A power law dependence may be fitted to the temperature dependence of the resistivity of the form

$$\rho = AT^n + \rho_0, \tag{3.1}$$

where ρ_0 is the residual resistivity at 0 K and A is the effective scattering cross section at low temperatures. By subtracting ρ_0 from Equation 3.1 and taking the natural logarithm one obtains,

$$\ln(\rho - \rho_0) = n \ln T + \ln A. \tag{3.2}$$

As can be seen from Equation 3.2 a straight line can be fitted to a ln-ln plot of $(\rho - \rho_0)$ against T which is obtained using a least square fit. The extrapolated gradient is the exponent and the intercept is the logarithm of the effective scattering cross section . This method is highly sensitive to the choice of ρ_0, which has been determined from a fit of the lowest temperatures measured.

3.2.2 DC Magnetisation and AC Susceptibility

An additional insert is used for the simultaneous measurements of DC magnetisation and AC susceptibility. The insert, which is shown in Figure 3.2 consists of several copper coil

sets wound around a hollow fibre glass tube which is placed within the sample chamber. The coil set consists of two counter wound coils with calibration coils wound around the centre of each. These are used for the measurement of the samples. Around these are the driver coil for the AC susceptibility measurements and the compensation driver coil wired in series and counter wound to the AC driver coil to compensate for external fields. An additional thermometer is also located in the centre of the coil set and used in addition to the other thermometry for temperature determination using this setup. This is due to the reduced thermal contact between the base of the cryostat where the PPMS sample thermometer is located and the sample in the magnetic measurement option. Samples are mounted within a plastic tube designed to produce low magnetic signals. The plastic tube is attached to a baffle rod which is secured to a servo motor located at the top of the sample chamber. This allows the sample to be translated through the coil set. Before measurements the samples are located within the coil set so in order to optimise the signal.

DC Magnetisation

During DC magnetisation a permanent external field is applied and the sample translated through both detection coils. The measured voltage is proportional to the rate of change of magnetic flux. Propriety software from Quantum Design is used to integrate these results and compare to a pre-calibrated standard to obtain the magnetisation data.

AC Susceptibility

In contrast to the DC magnetisation measurement in AC susceptibility measurements the samples remain stationary and an oscillating magnetic field is applied to induce a magnetic moment. This field is small with a typical value of 10^{-3} T used during the measurements presented. Due to the detection coils being counter-wound in series allows for the driving field to be eliminated from the signal measured. A five reading measurement is taken at each point. The first reading is performed with the sample in the centre of the lower detection coil, then the sample is measured in the centre of the upper coil followed once again by the centre of the lower detection coil. Finally two measurements are taken with

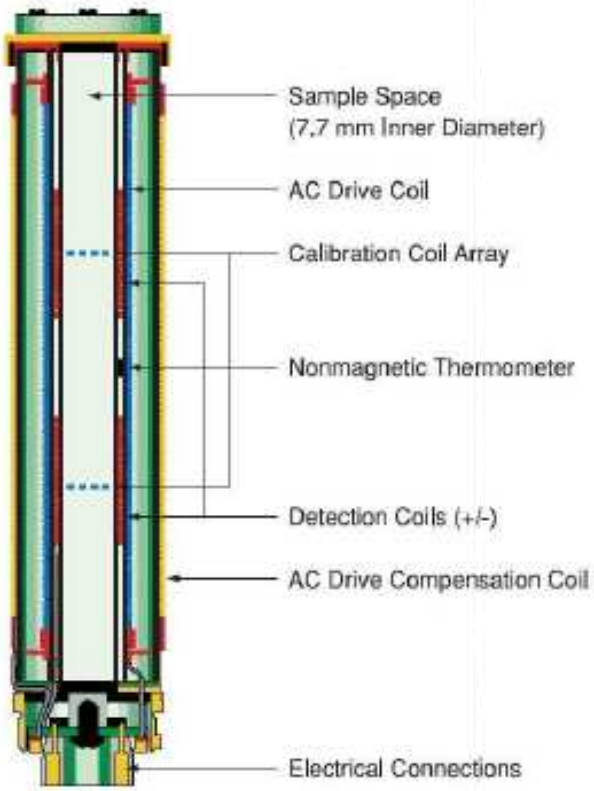

Figure 3.2: Diagram of coil set insert for the PPMS used for the measurements of DC magnetisation and AC susceptibility [40]. The diagram shows the sample space which is connected to a motor via a baffle rod at the top of the cryostat. Six coils are shown, two detection coils located and below an addition thermometer. Two calibration coils are are wound around the centre of the detection coils. The driver coil used for AC susceptibility is wound on the outside.

sample in the centre of the two detection coils. The AC susceptibility option provides an excellent signal to noise ratio with a signal sensitivity two orders of magnitude higher than the DC magnetisation (with the given value for the sensitivity of the susceptibility 10^{-10} Am^2 [40]).

Several frequencies of the applied field to ensure there are no non-linear dependencies, with typical values of 16, 33, 66, 133 and 233 Hz used.

3.2.3 Heat Capacity

Thermal Relaxation

The heat capacity setup consists of a sapphire platform with attached thermometer and heater which is suspended from the thermal bath by wires. They supply both the electrical contacts as well as well as the only thermal link to the bath for heat dissipation. Samples are placed in good thermal contact with the platform using a small quantity of Apeizon NNN grease. To reduce radiation heating a heat shield is used over platform and the whole experiment is performed under ultra high vacuum (UHV).

Measurements are taken using the thermal relaxation method [41] in which a heat pulse is applied to the sample until a steady state is achieved after which the sample is allowed to cool back down to equilibrium. Assuming that the thermal coupling between the sample and the platform is ideal and that the sample has a large thermal conductivity then the heat dissipation will be from the thermal conduction through the wires. By using the one dimensional heat flow equation,

$$P = A\kappa_w \frac{\partial T}{\partial z} + C(T)\frac{dT}{dt}, \tag{3.3}$$

where P is the power applied to the sample, A is the cross sectional area of the wires, κ_w is the thermal conductivity of the wires, $\frac{\partial T}{\partial z}$ is the change in temperature across the length of the wire, z and $C(T)$ is the heat capacity at constant pressure. Rearranging Equation

3.3 and setting $K_w(T) = \kappa_w(T)Al^{-1}$ leads to an expression for the heat capacity given by,

$$C(T) = \left(\frac{dT}{dt}\right)^{-1}\left[P - \int_{T_0}^{T} K_w(T')dT'\right]. \tag{3.4}$$

For a small temperature rise where $\Delta T = T_1 - T_0 \leq 2\%$ of T_0, K_w can be assumed to be a constant. The integral in Equation 3.4 then becomes;

$$\int_{T_0}^{T} K_w(T')dT' = K_w(\bar{T})\Delta T, \tag{3.5}$$

where $\bar{T} = \frac{1}{2}(T_0 - T_1)$. Combining in Equations 3.4 and 3.5 gives,

$$C(T) = \left(\frac{dT}{dt}\right)^{-1}\left[P - K_w(\bar{T})\Delta T\right]. \tag{3.6}$$

If the heat capacity of the bath is much larger than the heat capacity of the sample and the platform then the the bath temperature, T_0 remains constant in time.

$$\frac{dT_0}{dt} \ll \frac{dT}{dt} \Rightarrow \frac{dT}{dt} \approx \frac{d\Delta T}{dt}. \tag{3.7}$$

Therefore as $t \to 0$, so does $P \to 0$, thus giving;

$$C(T) = \left(\frac{d\mathsf{ln}(\Delta T)}{dt}\right)^{-1} K_w(\bar{T}). \tag{3.8}$$

This leads to the solution

$$T(t) = (T_1 - T_0)\mathsf{e}^{-t/\tau_1}. \tag{3.9}$$

Where $\tau_1 = C(T)/K_w$ is a characteristic time constant known as the relaxation time. The heat capacity can therefore be determined by fitting an exponential to the data such that,

$$C(T) = \frac{\tau_1}{K_w(T)}. \tag{3.10}$$

The thermal conductance of the wire, K_w is obtained from calibrations of the heat capacity puck. The measured heat capacity is a combination of the sample and the platform. To

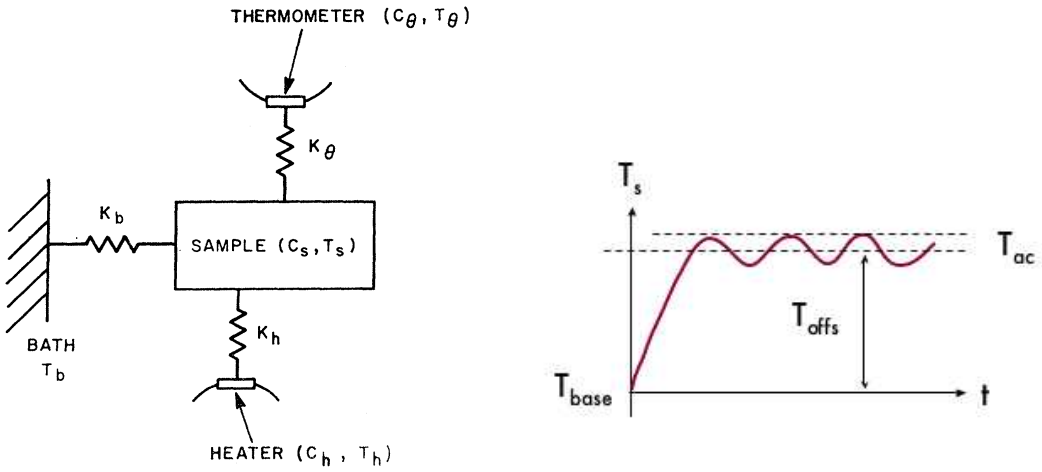

(a) (b)

Figure 3.3: (a) AC-Temperature Calorimetry setup [42] and (b) graph of the temperature of the sample when applying an alternating heat source.

obtain the sample heat capacity the addenda (a measure of just the platform) is subtracted from the data.

AC Calorimetry

AC-temperature calorimetry allows for continual measurement of the heat capacity of the sample. This method involves having the sample attached to a thermal bath via a link with thermal conductance, K_{bath} and applying an alternating heating source of power $\dot{Q}_0$ and frequency ω. A cartoon of this is shown in Figure 3.3(a). This will cause an initial temperature rise in the sample and then an oscillating temperature with a characteristic measurement quantity T_{AC} equal to the amplitude of the oscillation. This is seen as long as the thermal relaxation times τ^2_{heater} and $\tau^2_{thermocouple}$ are short such that $\omega^2\left(\tau^2_{heater}+\tau^2_{thermocouple}\right) \ll 1$. The behavior is shown in Figure 3.3(b). By determining T_{AC} from measurements the heat capacity can be found via

$$C_S = \frac{\dot{Q}_0}{2\omega|T_{AC}|}\left(1+\frac{1}{\omega^2\tau^2_{sample}}+\omega^2\tau^2_{Int}+\frac{2LK_{base}}{3A\kappa}\right)^{-\frac{1}{2}}, \tag{3.11}$$

Table 3.1: A list of pressure cell types and typical highest pressures achievable

Pressure Cell Type	P_{Max} / GPa	Notes
Piston Cylinder Cell	3	[43]
Bridgman Cell- Tungsten Carbide	10	[43]
Bridgman Cell- Sintered Diamond	40	Anvils are magnetic
Cubic Anvil Cell	10	Three opposed anvils, highly hydrostatic [44]
Moissanite Anvil Cell	60	Cheaper alternative to Diamond [45]
Diamond Anvil Cell	400	$P_{max} = 25$ GPa has been achieved in resistivity measurements [46]

here A is the cross sectional area and L the length of the thermal link to the bath. τ_{sample} is the relaxation time of the sample and τ_{Int} is associated with the time for the sample to attain thermal equilibrium is given by

$$\tau_{Int} = \frac{L^2}{(\pi/2)^{1/2}\, n}. \tag{3.12}$$

If $\tau_{Int} \ll 1/\omega \ll \tau_{sample}$ Equation 3.11 may be simplified further to

$$C_S = \frac{\dot{Q}_0}{2\omega|T_{AC}|}\,(1+c)^{-\frac{1}{2}}\,, \tag{3.13}$$

where $c = \frac{2LK_{base}}{3A\kappa}$ is a constant.

3.3 Pressure Measurements

To ensure hydrostatic pressure measurements the choice of pressure transmitting medium is highly significant. An ideal liquid with zero viscosity would exert equal pressure on every point of a sample immersed in it. The pressure is established by containing the pressure medium within a sealed container and reducing the container volume. A list of some of the pressure cells which have been used to achieve hydrostatic presssure conditions is shown in Table 3.3. In this work two types of pressure cell have been used, the piston cylinder cell and the Bridgman anvil cell.

3.3.1 Piston Cylinder Cells

Piston cylinder cells offer large sample space for hydrostatic pressure measurements and can therefore be used for a variety of physical property measurements. The downside is the low pressures achievable with a typical piston cylinder cell operating up to 3 GPa [43]. The piston cylinder cells presented in the following were designed to be used within the PPMS and a diagram showing the setup of a piston cylinder cell is shown in Figure 3.4 [47]. The main body consists of is a bored non-magnetic cobalt-nickel (MP35N) kernel surrounded by a beryllium-copper casing. A nickel-cobalt alloy (MP35N) feed-through is prepared with eight 100 μm copper wire twisted pairs which are passed through a 1 mm diameter hole into the pressure region. The hole is sealed with stycast (25:1 ratio of 2850FT to catalyst 9, Merson and Cummings). The copper wires are attached to a rectangular board to which the sample wires are attached. The samples remain freely suspended to allow maximum hydrostaticity. The samples are then enclosed within a Teflon tube which is sealed at one end. The tube measures 20 mm in length and has a diameter of 2.5 mm and is filled with a pressure medium before being sealed by the feedthrough. The feedthrough and teflon tube are then inserted into the bore of the main body and secured with a locknut which is screwed into the casing. A tungsten carbide rod is inserted into the other end to act as the piston, transmitting the force for pressure application. Pressure is applied with a hydrolic press via a larger tungsten carbide rod and a steel spacer. Pressure is retained by an additional locknut surrounding the spacer.

3.3.2 Bridgman Cell

For measurements requiring pressures higher than than 3 GPa (the maximum pressure of the piston cylinder cells) Bridgman anvil cells with scintered diamond anvils were used. These have a maximum pressure of approximately 20 GPa. The setup described in this section are developed from Bridgman [48]. The components of a Bridgman cell are shown Figure 3.5. The Bridgman cell consists of a pair of opposing tungsten carbide anvils [49] that fit into a Be-Cu sleeve. The gasket and sample area are set up on the bottom anvil and are screwed into the bottom of a Be-Cu sleeve, a simple tube measuring 62 mm in

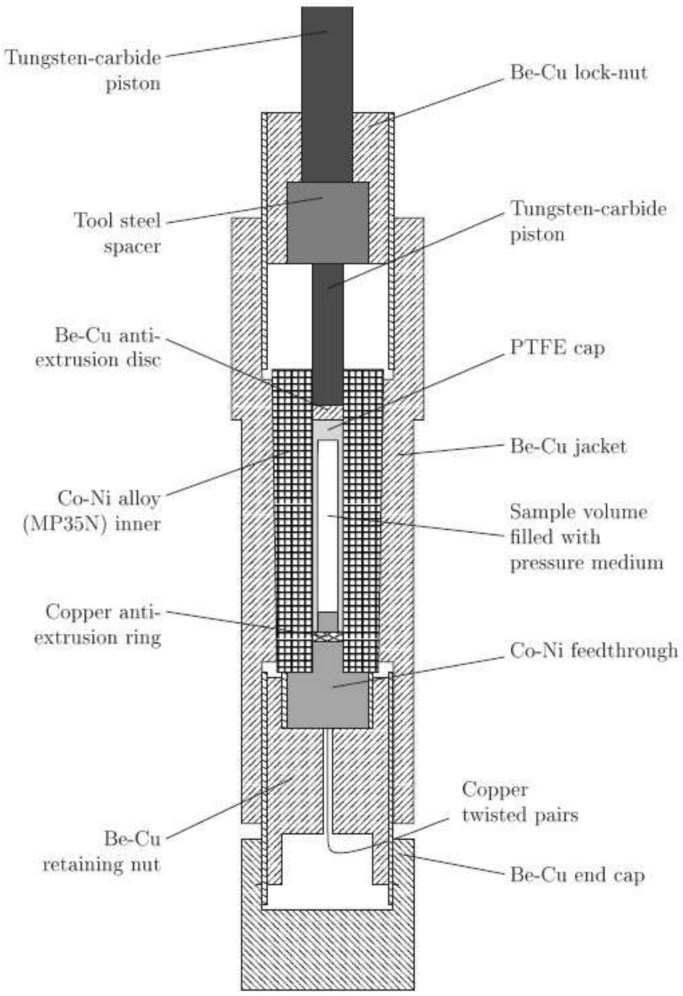

Figure 3.4: Cross sectional diagram of a piston cylinder cell [47] which was designed to fit within a PPMS. The sample is attached to a measurement platform which is attached to the Co-Ni feedthrough. Electrical contacts are made using eight twisted pairs of Cu wire which pass through the feedthrough into the sample volume. Pressure is applied via the tungsten-carbide piston to the liquid pressure medium contained by the PTFE cap. The pressure is retained by the Be-Cu lock-nut. The diagram is to scale.

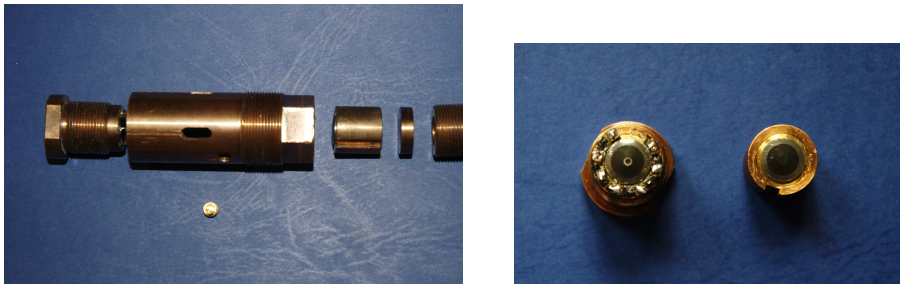

(a) (b)

Figure 3.5: Images of components for a Bridgman cell. Image (a) shows an exploded setup of the components of the Bridgman cell. Which shows left to right the lower anvil, the Be-Cu sleeve, the top anvil, a Be-Cu washer and the lock nut. (b) Top down view of the bottom (left) and top (right) anvil. Bottom anvil shows seven solder pads surrounding the anvil. The centre of the anvil shows a gray pyrophyllite gasket outside of which the anvil is covered in epoxy resin. The upper anvil also is covered in a small quantity of epoxy resin except the very centre which is left exposed.

length and 24 mm in diameter which has an internal thread at each end. The small dimensions of this pressure cell were designed to allow measurements within the PPMS. The body of the sleeve has four windows which are positioned at the same height as the top of the lower anvil when the anvil is screwed in position. This allows wires to leave the pressurised region without being bent or kinked. Grooves grinded into the outside of the sleeve allow the wires to be secured into position (with Teflon tape).

The upper anvil and a Be-Cu washer rest on top of the lower anvil and are secured with a lock nut. To apply pressure the cell is mounted on a hydraulic ram and pressure is applied via a Be-Cu piston through a hole in the lock nut. By tightening the lock nut the pressure is held while the press is released. The thread of the lock nut and sleeve are designed to be in stress when the load is released, minimising the pressure loss. A pin located in the groove of the upper anvil and the Be-Cu washer reduce rotational stress in the pressure chamber as the lock nut is tightened.

The sample space is created using a pyrophyllite gasket with a thickness of 200 µm. The gasket is placed on the cutlet of the lower anvil and fixed with a highly diluted General Electric (GE) varnish. Pyrophyllite, an aluminum silicate hydroxide, was chosen as the

gasket material due to its friction coefficient (0.35 [50]) with respect to metallic materials is quite high. High frictional forces allow the gasket to withstand the high pressure difference existing across its width [51]. An additional advantage in the material being insulating such that non-insulated wires may be passed through the gasket. Slow setting epoxy resin is then applied in a thin layer to the sloped outer region of the lower anvil up to the height of the gasket and also to the sloped region of the upper anvil to form an electrically insulating surface between the wires and the conducting tungsten carbide anvils. Figure 3.5b shows a top down view of the top and bottom anvil with the epoxy and gasket in place. Eight soldering points are glued around the perimeter of the anvil and four twisted 150 μm copper pairs are soldered to them. A scalpel is used to create eight 100 μm deep equally spaced grooves in the gasket that are directed radially (see Figure 3.6b).

Steatite is used as the pressure medium for both the resistivity and the heat capacity measurements. The steatite disc, polished to a third of the thickness of the pyrophyllite gasket (≈ 50 μm) is placed within the gasket and is fixed in place with a small amount of dilute GE varnish. The superconducting transition of lead, tin and zirconium are common manometers for high pressure measurements of this type[52, 53]. Here, lead has been used as a manometer and measured using the four point a resistivity setup described below. It is not possible to use the other manometers as their T_c is lower than the minimum temperature, of 1.8 K obtainable with the PPMS. The pressure dependence of the critical temperature, T_c for lead, in GPa is given by the empirical formula

$$P = 10\left(a + b\left(T_C\right) + c\left(T_C\right)^2\right). \tag{3.14}$$

The values of the constants shown are $a = 3.51$ GPa, $b = -0.77$ GPaK^{-1} and $c = 0.04$ GPaK^{-2} [54, 55, 56]. Pressure values reported in this thesis are taken as the midpoint of the superconducting transition. Their error is derived from the width of the transition and is a measure of the pressure inhomogeneity.

Resistivity

Upon following the basic setup described above the sample and lead manometer are secured to the steatite disk using a small amount of epoxy upon one corner, to ensure it remains fixed while pressure is applied but does not create any significant pressure gradient across the sample. Electrical contact is made using annealed (to increase pliability) 25 μm platinum wire cut into pieces 1.5 cm in length. The ends of these wires are flattened and cut back into points the width of the original wire. This is done to stop them spreading and touching the othere wires when pressure is applied. The platinum wires are then soldered to the soldering points, placed in the previously prepared grooves and covered with epoxy to ensure they are insulated from the top anvil (ensuring that none of the epoxy flows into the gasket). The pointed ends are then placed onto the sample in a four point measurement configuration, with maximum seperation between the two central voltage leads, while ensuring no contact between any of the leads. Steatite powder is then carefully packed into the gasket and a second steatite disc of identical thickness as the first ($\approx$ 50 μm) one is placed on top. Pyrophyllite powder is then packed into the grooves in the gasket containing the wires and the top anvil is carefully placed on top.

The contact between the sample and the platinum wires is created by the force applied. An initial force of around 1 kN is used resulting in a relatively high initial pressure, typically around 2 GPa to ensure good electrical conductivity.

Heat Capacity

This section describes a setup for measuring the heat capacity in a Bridgman cell. The method uses the method of AC Calorimetry as described in section 3.2.3, for the high pressure measurements an AC calorimetry method is used instead

Experimental Setup

To implement this method in a Bridgman pressure cell of the small sized used in this project poses several problems and with several iterations tried before the final setup. Half of the 1 mm sample space is used for the lead manometer which is measured using

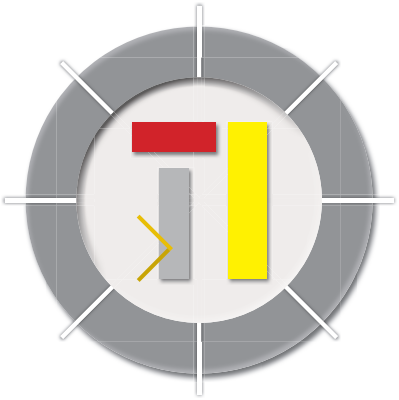

(a).

(b)

Figure 3.6: Heat capacity setup in a Bridgman Cell. (a) This sketch of the heat capacity setup shows the heater in red, the lead manometer in yellow and the Au-Au/Fe thermocouple shown in gold. The sample is shown in light gray. (b) shows a picture taken of heat capacity setup before closing. The sample with attached thermocouple is on the top left and the heater on the bottom left.

the four point resistivity setup in the above section. The remaining half of the sample space has to accommodate several components in contact with the sample. The heater is made of manganin ($Cu_{86}Mn_{12}Ni_2$), a resistive wire with a resistivity of, $\rho(300K) = 4.82 \times 10^{-9}$ Ωm. The thermometry used is a gold-gold/iron thermocouple which is spot wielded together and secured to the top of the sample, good thermal contact critical for a successful measurement. The final and most successful setup is shown in Figure 3.6 with a schematic of the design and a picture of a setup before closing.

Earlier setups had the heater and the sample in contact with each other which has the advantage of significantly better thermal conduction, however the heater broke frequently in this configuration such that a design where the heater was placed as close to the sample without touching was adopted.

This method has shown some reasonable results at low temperatures where the heat capacity is small. It can easily be seen from Equation 3.13 that the heat capacity is inversely proportional to the temperature change, which is proportional to the measured

voltage. As the heat capacity increases with increasing temperature the voltage drops to within the noise.During testing while developing this temperature was found to be around 10 K. This was to low to study any of the magnetic transitions of the materials presented in this thesis. To further develope this, advantage can be taken in the fact measurements are taken using the second harmonic. This allows a direct connection between the heater and the sample was the interference from the heater voltage on the measure voltange will be small. A resistive material for the heater is therefore required which can withstand the large uniaxial pressure between the sample and the heater without breaking. If this is achieved higher measurement temperatures should be achievable.

3.4 High Pressure AC Susceptibility

A method for incorporating two coils in a counterwound orientation inside the sample space of a Bridgman anvil cell has been developed to allow the measurement of susceptibility up to 20 GPa in a Bridgman anvil cell with high sensitivity.

Previous approaches have included diamond anvil cells with the pick up coil only within the sample space. Due to the limitation in sample space the compensation coil is placed outside the gasket with an auxiliary driver coil placed around it [57]. These have produced good results in measurements of the magnetic susceptibility and NMR. In some cases specially grown diamonds with a six turn pick up coils fabricated on top of one of the anvils [58] have been used which allow pressures of the order of 100 GPa. Miniature diamond anvil cells have been manufactured which can be placed within commercial SQUID magnetometer [59]. However due to the reduced size of the cell body the maximum pressure is restricted. All the diamond anvil cell designs have only provided enough space for a pick-up coil in the sample space, to allow for counterwound pick-up and compensation coils inside the sample space a Bridgman anvil cell has to be utilised.

From the outset the use of a liquid pressure environment for a Bridgman anvil cell was desired to give optimal hydrostatic conditions. Initially a method similar to the design by Jaccard et. al. was attempted [60]. Wherein a pyrophyllite gasket is sealed with an

epoxy resin. This setup with a 2 mm diameter sample space showed excellent results for susceptibility measurements up to around 10 GPa [60]. A pickup and counterwound compensation coil as well as a driver coil was incorporated within the sample space adapted to allow a liquid pressure medium. To perform measurements above 10 GPa in a Bridgman cell requires a much smaller sample space to allow susceptibility measurements up to 20 GPa. Due to the reduced size of the gasket hole available with the anvils used to achieve higher pressures filling the sample space with a liquid pressure medium proved impossible. The smallest droplets of pressure medium would overfill the sample space and cause the gasket to come in contact with the liquid pressure medium. This caused the gasket to become unstable and break under very small pressures. Other previous adaptations of a Bridgman anvil cell to use liquid pressure medium also involve sealing a pyrophyllite gasket, usually with a ring of Teflon or nylon [61, 62, 63, 64]. Examples of the Teflon and nylon adaptations are shown in Figure 3.4.

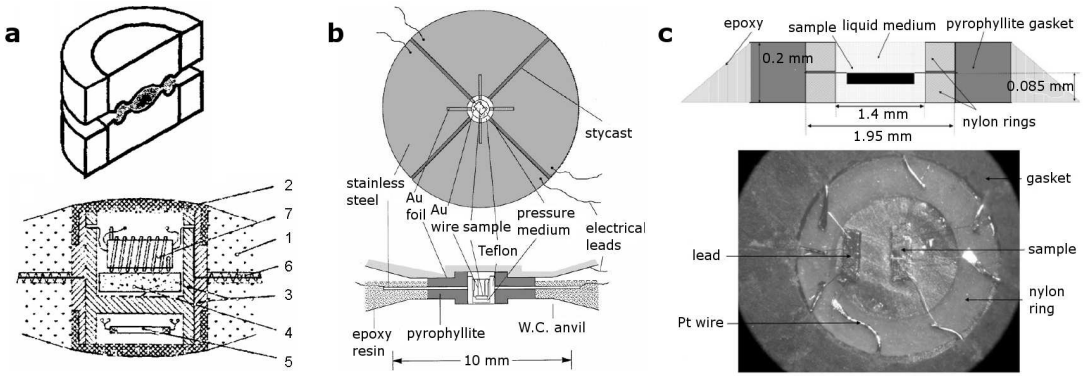

Figure 3.7: Figure showing various realisations of gaskets for use with a liquid pressure medium in a Bridgman pressure cell. (a) shows a modified anvil with teflon ring seal for high temperature measurements [61] (b) shows a teflon ring seal with four wires [62] and (c) shows a cell with a nylon ring seal with multiple wires entering sample space [64]. Image from [65].

These adaptations however were all made to perform electrical transport measurements or multiple simultaneous measurements which require at least four wires (and up to 16 wires to enter the sample space). A steel gasket is generally not used as it increases the chance of the wires short-circuiting as pressure is increased. Adding grooves to the steel

gasket reduces the chance of short circuiting however is technically hard to achieve for a large number of grooves. If a small number of wires were used small grooves could be added into the sample space without adversely affecting the stability of the gasket at high pressures. In the setup detailed below only two wires are required allowing a steel gasket to be an appropriate choice. The gasket is pre-indented to a thickness of 150 µm. This was found from optimising an initial pre-indention of half the maximum pressure, which was found to be two thick, with very small pressure changes seen up to the maximum pressure. Several measurements were run with varying smaller thicknesses with the final thickness chosen that was both stable and allowed high pressures to be reached. The optimal thickness is the same thickness as for the pyrophyllite gaskets used for these anvils. A 1 mm hole is drilled into the centre of the gasket which forms the sample space. Finally a 50 µm tungsten wire is secured across the centre of the hole extending radially to the edge and a small pressure applied to create 2 grooves into the gasket into which the wires leaving the sample space will sit.

Microcoils are formed from 35 μm copper wire which is wound around a 100 μm tungsten former. The coils consist of two counterwound coils of five turns each, both with a maximum height of three turns to allow them to fit within the sample space. These form the pick-up and counterwound coils. Once the pick up and compensation coils are wound they are removed from the former and manipulated such that the two coils are adjacent to each other. The microcoils are fed out through the two grooves pressed into the gasket. These are then covered with a mixture of stycast and alumina powder to seal the sample space and protect the wires. Finally a 70-80 turn driver coil is wound out of 100 μm copper wire around a 1 cm diameter tungsten cylinder (untapered). This is placed around the steel gasket and secured with GE varnish. Two photographs of a pressure cell are shown in Figure 3.8 showing a close up of the pick-up coils and the second where the driver coil and gasket are visible. In both shots the stycast has not been added to the grooves for clarity of the shots.

Due to the limitation on space and to the reduce the number of grooves needed in the gasket (due to weakening of the gasket) a four point resistivity measurement of a

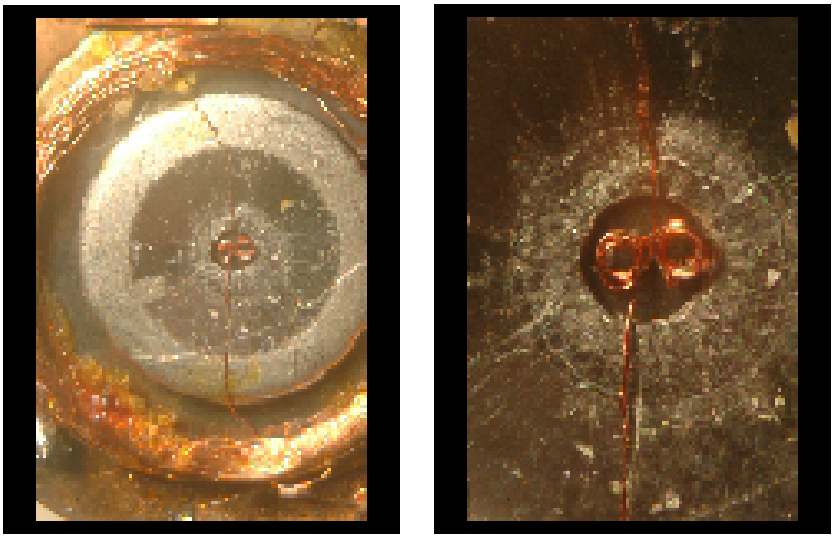

(a) (b)

Figure 3.8: Photographs of the susceptibility setup in a Bridgman anvil cell. (a) shows 77 the driver coil on the outside of the steel gasket. The leads of the pick-up coil and compensation coil circuit reach the sample space through two grooves, which are positioned above and below the sample space in this photograph. (b) shows an expanded view of the centrally located sample space showing the arrangement of counterwound pick-up and compensation coils inside the sample space.

manometer is not usable. Instead a piece of lead is placed within the compensation coil of the susceptometer. As the coils are counterwound the signals of the sample and manometer appear with opposite signs.

Concerning the pressure medium, initially an alcohol based liquid was used. A 50:50 ratio of pentane and iso-pentane which has a flash point of ≈ 230 K making it an excellent hydrostatic pressure medium. However the fast evaporation allowed a very brief time span to close the pressure cell leaving the sample space less than optimally filled before it was sealed. Therefore an oil was used instead, in this case Daphne oil 7373, manufactured by Idemitsu Kosan Co. Ltd., Tokyo, Japan. This oil is a modified spindle machine oil which shows small pressure losses between room temperature and liquid He temperatures. At 1 GPa the pressure loss amounts to around 0.12 GPa and diminishes as applied pressure increases. Another important factor is a continuous pressure variation under solidification. At room temperature Daphne oil solidifies at 1.9 GPa [66]

Susceptibility signals will be measured using a lock-in amplifier. From electrodynamics the voltage change across the pick up coil, V_{emf} as a function of the susceptibility is given by [67]

$$V_{emf} = 2\pi^2 N r^2 B f \eta \chi_{ac}, \tag{3.15}$$

where N is the number of turns and r^2 the radius of the pick up coil. η is the effective filling factor, f the operating frequency and B the magnetic induction. χ_{ac} is the ac susceptibility of the system (in the superconducting state $\chi_{ac} = -1$).

The cell was initially tested, characterised and refined with just a sample of lead used. After the final design was determined the pressure design was used in the measurement of Mo_3Sb_7 . These can be seen in the results section in chapter 5.2.

Chapter 4

$FePt_3$

4.1 Abstract

The aim of this section is to study a 3D antiferromagnetic quantum critical point. $FePt_3$ is a rare example of a 3D antiferromaget with a second order phase transition in a transition metal material. Results presented show a surprisingly weak pressure dependence. Also seen are weak electron-electron interactions seen in the resistivity power law analyses (with $n > 2$ seen over all pressures). The results show that the 3D antiferromagnetic region is technically out of reach for $FePt_3$ in a Bridgman anvil pressure cell.

4.2 Introduction

$FePt_3$ is a face centered cubic alloy ((Cu_3Au)-type) with iron occupying the corner sites. $FePt_3$ orders antiferromagnetically below the Néel temperature, $T_N = 170$ K. The magnetic moments of iron form a C-type antiferromagnetic state, with a $(\frac{1}{2}\frac{1}{2}0)$ ordering wave vector and ferromagnetic sheets in the (110) direction. The platinum atoms play no part in the magnetic structure. $FePt_3$ undergoes a second magnetic transition, which is a transition between two antiferromagnetic states with a transition temperature of, $T_S = 80$ K. This phase was initially studied in 1962 where an inhomogeneous spin structure model was proposed [68] wherein the C-type antiferromagnetic state changes to an A-type an-

tiferromagnetic state with ferromagnetic planes in the (100) direction. A more recent inelastic neutron experiment has suggested a homogeneous spin structure mode, in which both $(\frac{1}{2}\frac{1}{2}0)$-type and $(\frac{1}{2}00)$-type spin correlations coexist in the low temperature phase with a resulting non-collinear spin structure [69]. Due to the magnetic domain distribution however in the low-temperature phase the actual spin structure was not determined. Using uniaxial pressure to break cubic symmetries in the lattice, the spin structure was determined from a second neutron experiment [70]. The resulting spin structure is shown in Figure 4.1.

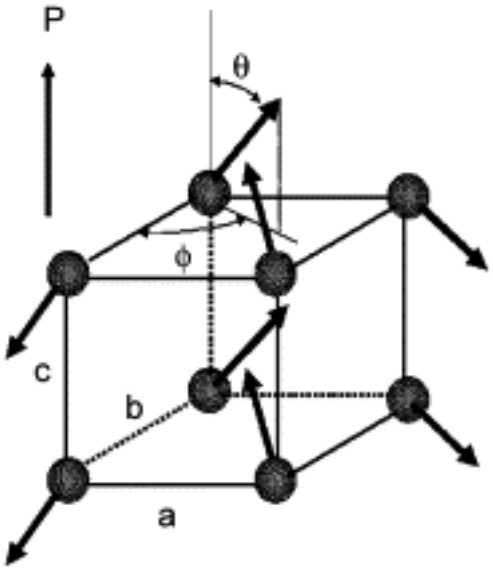

Figure 4.1: Non-collinear magnetic structure of $FePt_3$ below $T_S = 80$ K [70] determined from neutron measurements with uniaxial pressure applied in the p direction. The angles were found to be $\theta = 58^\circ$ and $\phi = 44^\circ$.

4.3 Samples

The samples were obtained from Y. Tsunoda's group from Waseda University, Japan. These were previously used to perform neutron experiments to determine the spin structure [69] of the low temperature antiferromagnetic phase. Of the samples received a single piece of dimensions 6.49 mm x 4.08 mm x 2.14 mm and mass of 1.0247 g was used for all

measurements. X-ray measurements taken of this sample showed a single crystal as well as powder regions within the sample. The results of a x-ray diffraction measurements in one of the three orthonormal directions of the single crystal is shown in Figure 4.2. A unit cell length of 7.7(1) Å is derived (using commercial software from Oxford Diffraction ltd) from the Bragg peaks of the single crystal, in agreement with the literature values [71].

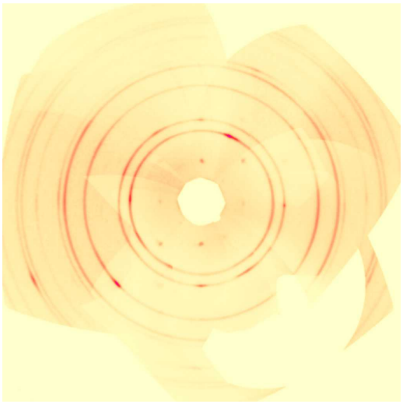

Figure 4.2: X-ray diffraction image of one of the orthonormal faces of the $FePt_3$ sample used for all measurements. The Oxford Diffraction ltd Xcalibur diffractometer at Royal Holloway was used for this measurements. Figure shows set of Bragg peaks from large single crystal as well as powder rings.

4.4 Zero Pressure Results

4.4.1 Resistivity

Four point resistivity measurements were performed over a range of 2-300 K in the PPMS on a sample with dimensions 2.5 mm x 2.0 mm x 0.3 mm and the voltage lead separation was 2.0 mm. Figure 4.3 shows the resistivity measured in zero magnetic field and in a 9 T magnetic field, with the current applied in the (100) direction ad the magnetic field perpendicular in the (010) direction. Two kinks in the data are observable which relate to the magnetic transitions in the sample. The lower graph of Figure 4.3 shows the differential of the resistivity ($d\rho/dT$), where the transition temperatures can be seen as two clear features in the data. From these results no difference is observed in T_N at zero

field and at 9 T. A reduction in T_C of 2 ± 1 K is seen between 0 T and 9 T. The zero field transition temperatures derived from the resistivity are $T_S = 82 \pm 2$ K and $T_N = 171 \pm 2$ K both of which are in good agreement with the literature [68].

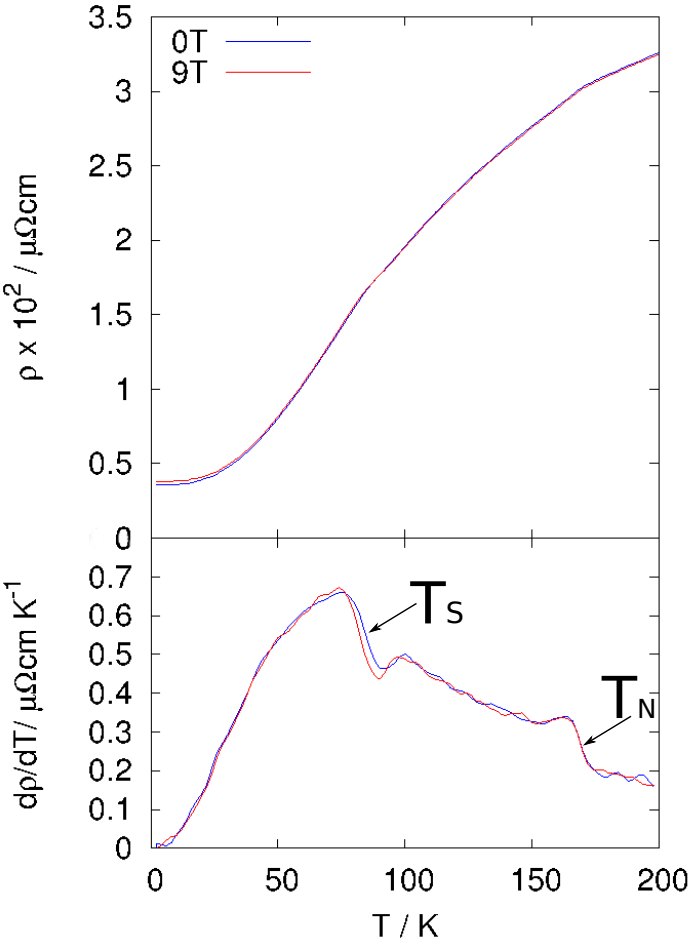

Figure 4.3: Resistivity of $FePt_3$ at ambient pressure. Top figure shows the resistivity, ρ at 0 T and at 9 T. The current is applied in the (100) and external magnetic field perpendicular to this in the (010) direction. The bottom figure shows the temperature derivative of this data $d\rho/dT$. The two magnetic transitions are shown by arrows, the paramagnetic transition, $T_N = 171$ K and the antiferromagetic to antiferromagetic transition, $T_S = 82$ K. A small decrease, $\Delta T_S = 2$ K is seen between 0 T and 9 T. No change is seen in T_N up to 9 T.

4.4.2 Heat Capacity

A 79.3 mg sample was placed on the PPMS heat capacity puck and measured with a 10% increase in temperature between 2 K and 300 K. The measured data for the total heat capacity, C_p is shown in Figure 4.4. The Figure shows a step around the paramagnetic

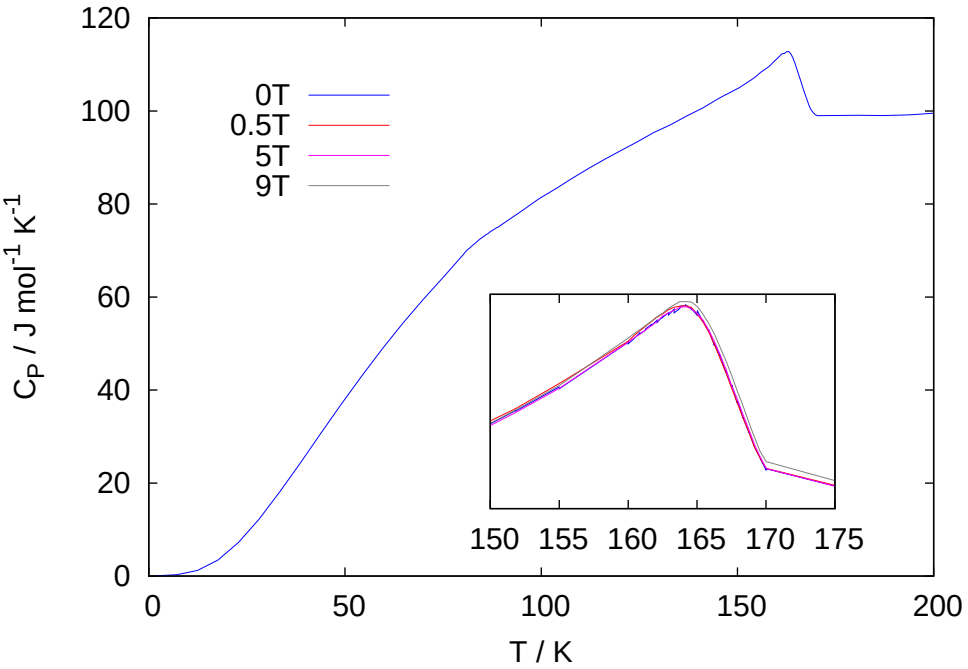

Figure 4.4: Heat capacity, C_p, as a function of temperature for $FePt_3$ at zero pressure. A kink is seen at $T_S = 83$ K and and step is seen at $T_N = 167$ K. An insert shows the magnetic field dependence around T_N with the field applied in the (100) direction. No dependence is seen with changing magnetic field.

to antiferromagnetic transition $T_N = 167$ K and a kink is seen at antiferromagnetic-antiferromagnetic transition $T_S = 83$ K. A second order phase transition shows a discontinuity in the second order derivative of the Gibbs free energy (such as heat capacity) which suggests that the paramagnetic to antiferromagetic transition is a second order transition. The field dependence of the paramagnetic to antiferromagetic transition up to 9 T is shown in as an inset to Figure 4.4. This shows no field dependence on the paramagnetic to antiferromagetic transition.

4.4.3 Magnetic Susceptibility

Previous measurements on the susceptibility of $FePt_3$ between 20 K and 900 K showed a very distinct peak at the Néel temperature in zero magnetic field [72]. An initial 76.5 mg sample was mounted vertically into a susceptibility straw with the (100) direction mounted parallel to the applied magnetic field. The data is shown in Figure 4.5. This shows a peak at the paramagnetic to antiferromagnetic transition at 168 K and a shoulder at the antiferromagnetic-antiferromagnetic transition at 79 K. When a field of 0.1 T is applied in the (100) crystallographic direction the feature at the paramagnetic to antiferromagnetic transition is no longer seen, though no change in the position of the peak is observed below this field. There is no change in the shoulder seen at the antiferromagnetic-antiferromagnetic transition up to 1 T.

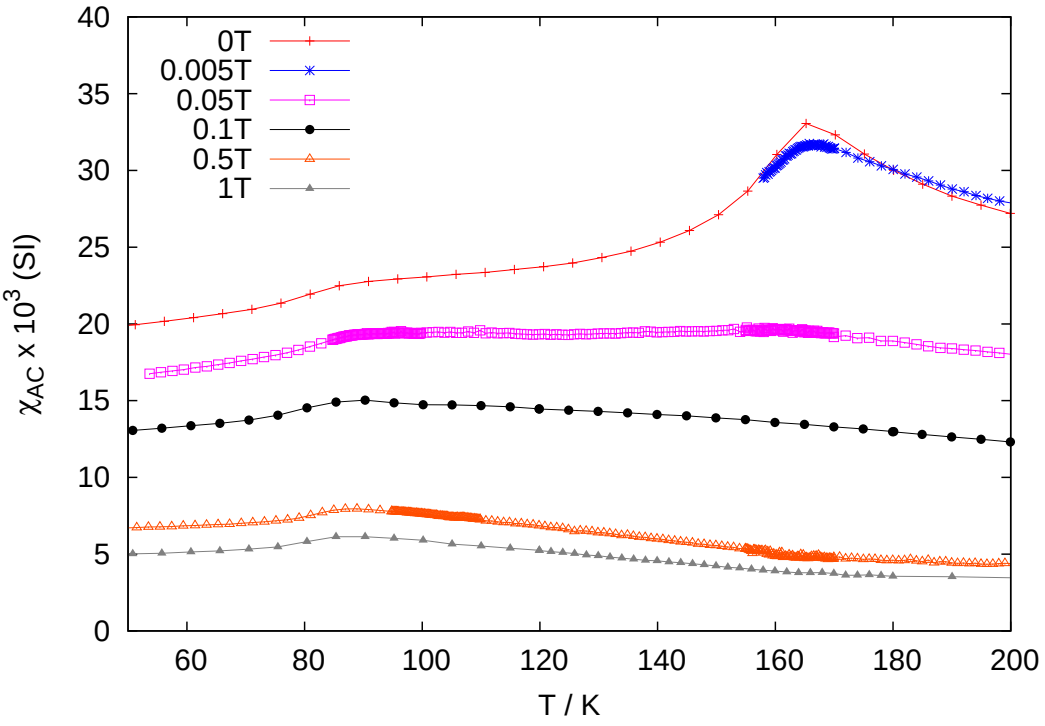

Figure 4.5: Real part of the magnetic susceptibility, χ_{AC}, of $FePt_3$ with a magnetic field applied in the (100) direction. At zero field a shoulder is seen at 79 K and peak at at 168 K which relate to the T_S and T_N seen in the resistivity results (Figure 4.3) respectively.

4.4.4 Evaluation of the Zero Pressure $FePt_3$ Data

From physical property measurements of $FePt_3$ several features of this system have been seen. The position of the antiferromagnetic to paramagnetic phase transition is unaffected by the application of magnetic field. The antiferromagetic to antiferromagetic phase transition shows a small decrease with applied field. In the measurements of magnetic susceptibility a decrease in the magnitude of the peak at T_N is seen, with the peak being suppressed by 0.1 T. No change is seen in the shoulder at T_S. Transport measurements show no change in the resistivity or heat capacity around the paramagnetic to antiferromagnetic transition with the application of magnetic field.

4.5 High Pressure Measurements of $FePt_3$

Resistivity measurements in a Bridgman anvil cell using a steatite pressure medium was used to explore $FePt_3$ at high pressure. The technique used is described in Section 3.2.1. Temperature sweeps were performed between 2 K and 250 K at zero magnetic field up to a maximum pressure of 12.8 GPa before the cell failed. The results are presented in Figure 4.6. The temperature derivatives of the resistivity data are shown in Figure 4.7. The transition temperatures were taken as the mid-point of the step of the derivative data in Figure 4.7. The phase diagram of $FePt_3$ taken from these results is shown in Figure 4.8. From this phase diagram it can be observed that the paramagnetic to antiferromagetic transition increases with increasing pressure. An initial decrease is seen in T_S up to 7 GPa.

4.5.1 Power Law Relation

To study if pressure tuning has any effect on the magnetic ordering a study of the power law dependence on the resistivity between 2-10 K is presented below. The data is fitted using the procedure discussed in Section 3.2.1. A plot of the exponent n as a function of pressure is plotted in Figure 4.9. All results range from n=2.1-3.3 all above T^2, suggesting that electron-electron scattering is a weak contribution. The values are around to $n = 3$ which is expected for electron-phonon interactions. No general trend in the evolution of

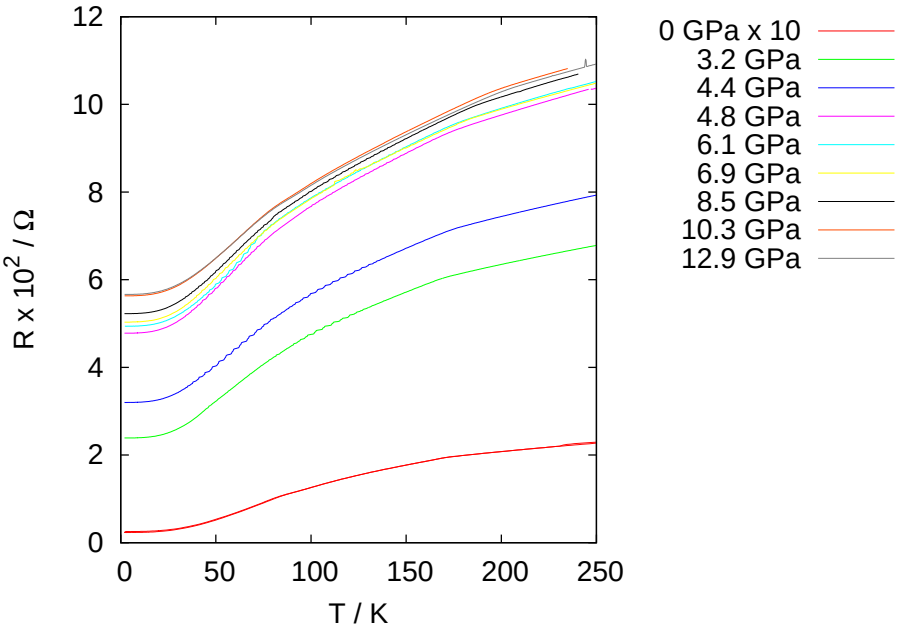

Figure 4.6: Resistance, R, as a function of temperature for $FePt_3$ for various pressures up to 12.8 GPa measured in a Bridgman anvil cell. The zero pressure data has been scaled. Kinks can be seen around 80 K relating to T_S and a kink seen around 180 K at T_N.

the power laws in determinable.

4.5.2 Conclusion

The fact that the magnetic transitions are so weakly pressure dependent is a surprising result. It is expected that the magnetic transition temperature should reduce with applied pressure. This is taken from the Stoner model of magnetism which applies well to transition metals and the Stoner criterion for magnetism which is

$$\tilde{D}\left(E_F\right) I_S > 1, \tag{4.1}$$

where I_S is the is the Stoner parameter which is a measure of the strength of the exchange correlation and $\tilde{D}\left(E_F\right)$ is the density of states at the Fermi energy per atom per spin. On applying homogeneous pressure to a system the lattice shrinks leading to a greater overlap of the atomic orbitals. This should delocalise the electrons and cause them to

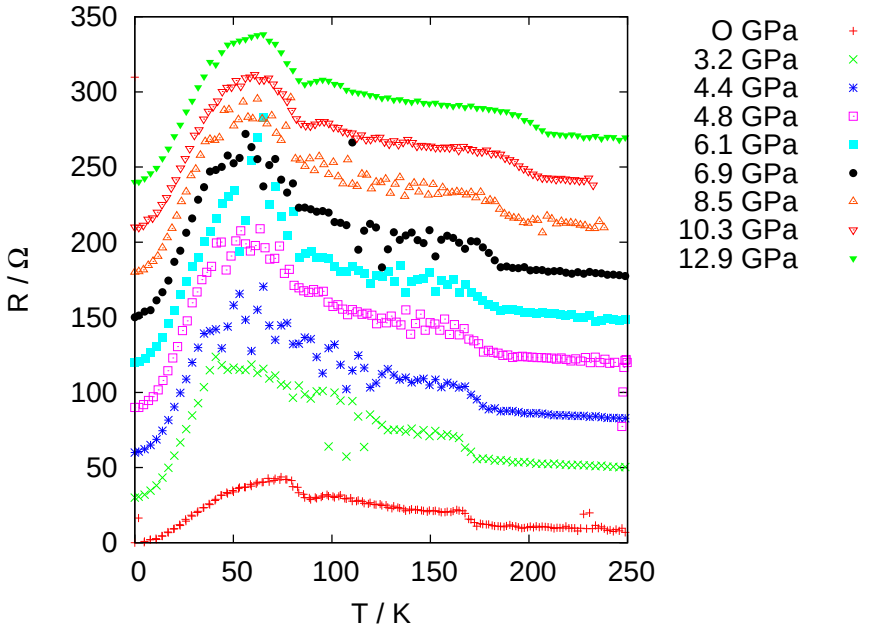

Figure 4.7: The temperature differential of the resistance, dR/dT, shown in Figure 4.6. Two steps are seen relating to the two magnetic transitions, the first near 80 K relating to T_S and the second seen around 180 K at T_N. The data has been offset for clarity.

occupy a wider range of energies, i.e., to create a larger bandwidth, to fulfill the criteria of Pauli's exclusion principle. This results in a decrease in the in the density of states. Finally at high enough pressures the Stoner criteria will no longer be fulfilled and the transition temperature should collapse. The power law analyses has shown that up to the highest pressures weak electron-electron interactions, with n¿2 seen over the entire pressure region. No overal trend was seen in the pressure evolution of the power laws.

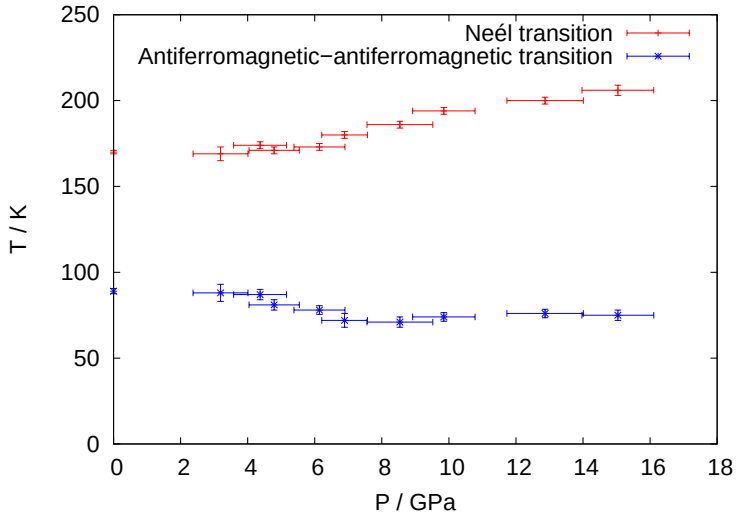

Figure 4.8: Phase diagram of the magnetic transitions of $FePt_3$ as a function of pressure. The Neél transition, T_N shows an increase from 170 K to 205 K. The antiferromagnetic-antiferromagnetic , T_S shows a initial decrease up to 7 GPa and is linear after.

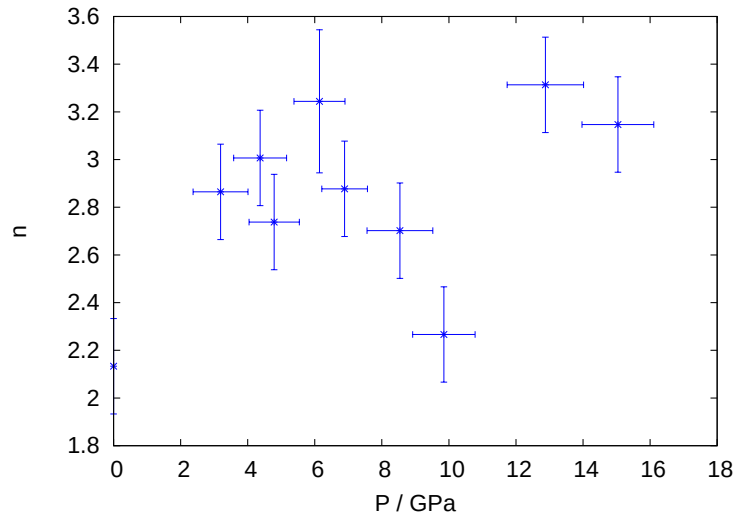

Figure 4.9: The power law exponent of resistance data from Figure 4.6 as a function of pressure for $FePt_3$. Exponent was determined between 2-10 K. No general trend can be seen in the evolution of the power law.

Chapter 5

Mo_3Sb_7

5.1 Abstract

The motivation for this chapter is to study superconductivity induced by a 3D antiferromagnetic spin fluctuation in a transtion metal system. Mo_3Sb_7 is an ideal candidate system as superconductivity is seen at zero pressures and a spin density wave at low pressures. The aim of this chapter is to extend the pressure-phase diagram to explore the correlation between the spin densitiy wave and superconducting phase.

5.2 Introduction

Mo_3Sb_7 is a cubic system with the Ir_3Ge_7 structure. It undergoes a structural transition at $T^* = 50$ K from cubic to a tetragonal structure [73]. This is related to a Mo-Mo dimerisation below T^* in the z direction of the tetragonal lattice. Mo_3Sb_7 was found to be superconducting with a critical temperature, $T_c = 2.1 \pm 0.2$ K [74]. Several possibilities for the type of superconductivity have been discussed in the literature. Originally a BCS-type behavior was suggested from magnetisation data [74] and point contact Andreev reflection [75]. More recent point contact Andreev reflection suggested that it was not a conventional s-wave superconductor, but instead an (s+g) wave or another unconventional superconductor. Low temperature specific heat and and muon spin rotation studies below 0.5 K

have been analysed in terms of two BCS-like gap models with gap widths $2\Delta_1/k_BT_c = 4.0$ and $2\Delta_2/k_BT_c = 2.5$ [76, 77] . These experiments also show that the effective masses of the charge carriers are enhanced ($\approx 16 - 18\ m_0$) compared to a conventional BCS superconductor. Electrical resistivity, specific heat and magnetic susceptibility measurements performed down to 0.6 K have been interpreted in the framework of spin fluctuation theory [78]. Using this theory an expected superconducting transition temperature, T_c was estimated using a modified McMillan expression which takes into account paramagnon effects [79]. The modified McMillan expression is

$$T_c = \frac{\Theta_D}{1.45} \exp\left(\frac{-1.04\,(1+\lambda_{eff})}{\lambda_{eff} - \mu^*_{eff}\,(1+0.62\lambda_{eff})}\right), \tag{5.1}$$

where Θ_D is the Debye temperature and λ_{eff} and μ^*_{eff} are the renormalised parameters for the electron phonon wavelength and the Coulomb parameter with the contribution from spin fluctuations. The estimated value for the transition temperature was found to be $T_c = 1.4 - 2.0$ K. Without the spin fluctuations the transition temperature is expected to be significantly higher, $T_c \approx 8.7 - 11.0$ K.

5.2.1 Samples and characterisation

Polycrystalline samples were prepared and the purity, homogeneity and crystal structure of the sample were checked by X-ray diffraction by V.H. Tran et. al.. Additionally the purity of the sample was checked by a scanning electron microscope and an energy dispersive X-ray spectrometer [80]. V.H. Tran et. al. also determined the zero pressure bulk physical properties, with the susceptibility and resistivity reproduced in Figure 5.1 and 5.2 respectively. The onset of diamagnetism in the susceptibility occurs at 2.28 K, the saturation at the base temperature measured was 45 % in the zero field cooled case and 30 % in the field cooled case. The resistivity shows the superconducting transition with $T_c = 2.26 \pm 0.12$ K. Also observed is an upturn in the resistivity above the critical field suggesting a positive magnetoresistance. For a spin density wave phase a negative magnetoresistance would be expected.

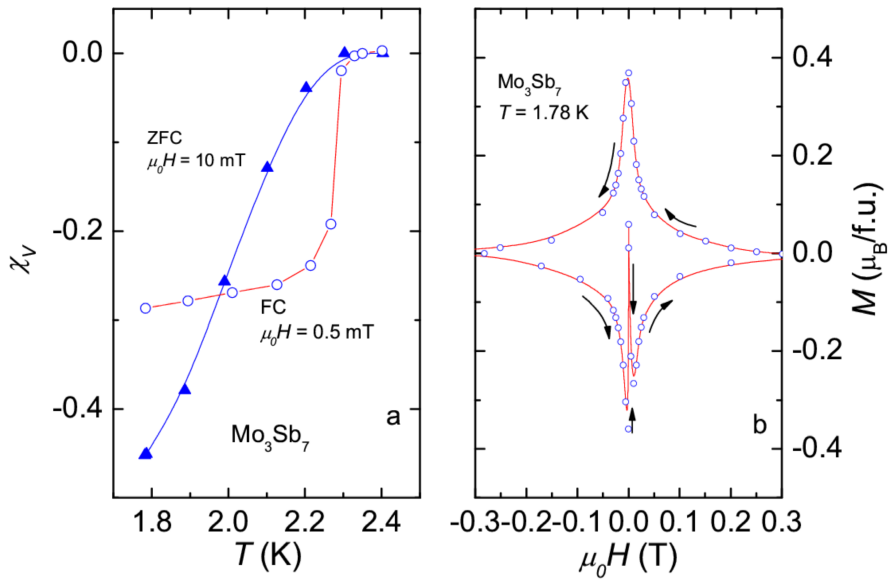

Figure 5.1: Zero pressure magnetic measurements of Mo_3Sb_7 [80]. (a) shows the susceptibility as a function of temperature around the superconducting transition, T_C = K, in the field cooled (FC) and zero field cooled (ZFC) cases. (b) shows the magnetisation as a function of magnetic field at 1.78 K between -0.3TT and 0.3 T. Arrows show the direction of change of magnetic field. In low field range M-H curve follows a linear dependence. Deviation from this dependence is estimated to be 3.2 mT.

5.2.2 High pressure results

V.H. Tran et. al. also performed low pressure resistivity measurements up to 2.2 GPa and magnetisation measurements up to 0.6 GPa [81]. The superconducting transition was observed to increase from the initial value of $T_C = 2.1$ K to $T_C = 2.38$ K at the maximum pressure measured of 2.2GPa. At 0.45 GPa an additional feature is observed in the resistivity at 6.6 K. A minimum is observed at a similar temperature in the magnetisation measurements, which is suppressed by a magnetic field of 0.02 T. This is described as a spin density wave transition. At 0.02 GPa a small anomaly at 6.7 K is seen which could also be ascribed to the spin density wave. This transition is suppressed to $T_{SDW} = 6.1$ K at the highest pressure. The results from the resistivity data are reproduced in Figure 5.2 and the reproduced phase diagram shown in Figure 5.3. By determining the derivative of

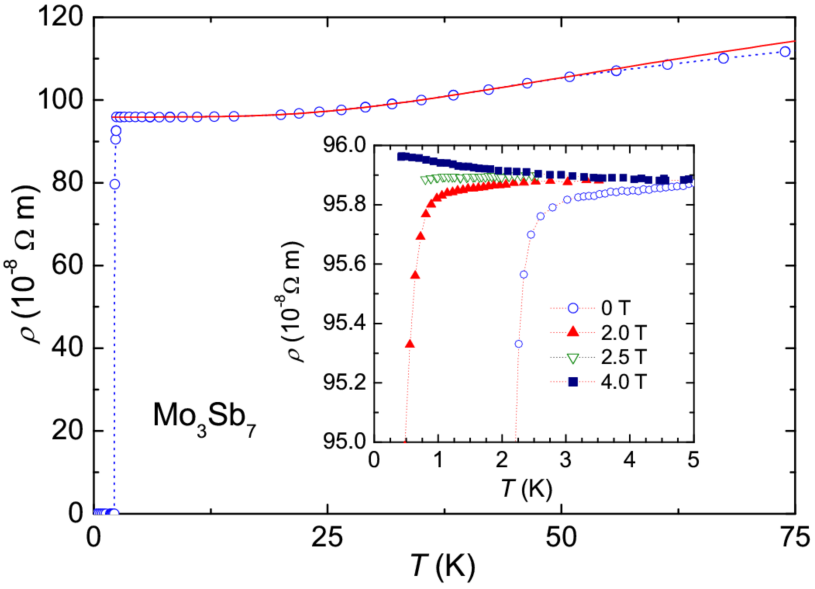

Figure 5.2: Zero pressure measurement of the tempereature dependence of the electrical resistivity, *rho* of Mo_3Sb_7 [80]. The insert shows the evolution of the resistivity with a finite magnetic field, showing the suppression of the superconducting transition to be below 0.2 K by 2.5 T.

the resistivity with respect to temperature around the structural transition a decrease in T^* with increasing pressure was observed.

The aim of this chapter is to further explore the pressure phase diagram to understand the relation between the magnetic spin density wave transition and the increase in the superconducting transition temperature.

5.3 High Pressure Measurements

To study Mo_3Sb_7 the susceptibility was measured in a Bridgman cell as described in Section 3.4. For the purpose of exploring the high pressure-temperature phase diagram of Mo_3Sb_7 susceptibility measurements were more suitable than resistivity measurements. Using this technique it was possible to use a liquid pressure medium (Daphne oil) ensuring very good hydrostaticity and the method employed was considered to me more promising

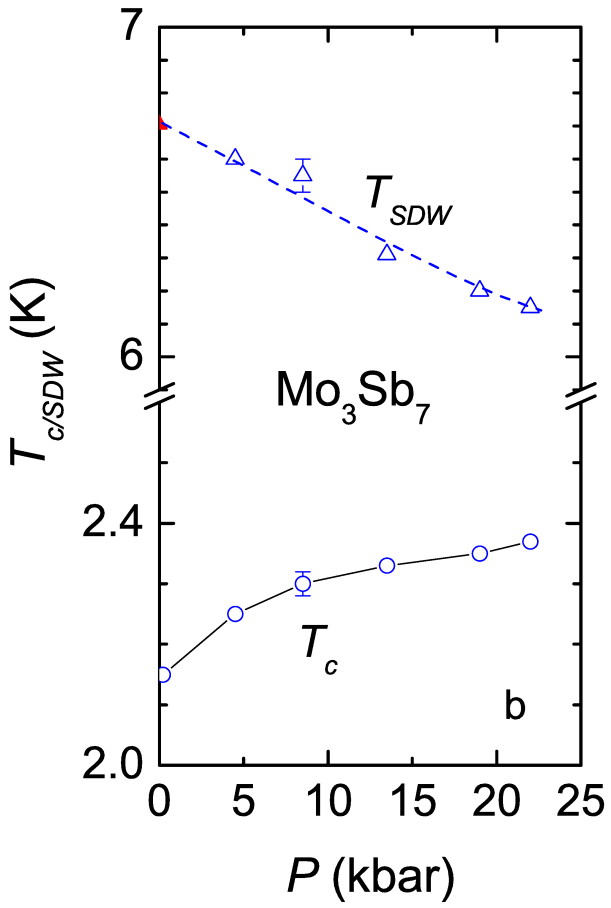

Figure 5.3: Pressure-temperature phase diagram of Mo_3Sb_7 showing the superconducting critical temperature, T_c (circles) and spin densitiy wave transition temperature T_{SDW} (triangles) [81]. All data taken from resistivity data. T_{SDW} is taken from a sharp anomaly seen in the data above 0.45 GPa. A small anomaly is seen in the 0.02 GPa data and is indicated by a red triange instead of blue.

in resolving the spin density wave transition.

During measurements of Mo_3Sb_7 several different pressure cells were used. Figure 5.4 shows three zero field cooled (ZFC) susceptibility measurements at low pressure taken in the same cell. This setup worked up to 0.6 GPa. From the data shown in 5.4 many features can be seen. The superconducting transition of Mo_3Sb_7 is seen as a upward step around 2.2 K. The superconducting transition of the Pb manometer is seen as a downward

step around 7 K (the step in the opposite direction to the superconducting transition of Mo_3Sb_7 due to the manometer being located in the compensation). A change of gradient in the susceptibility is seen around 4 K and continues to base temperature in this case. This systematically appeared in all the pressure setups, the cause of which has yet to be determined. The onset and width of the feature changes slightly between setups. Two more features, seen as downward steps, can be seen in the data the first at 6.2 K and the second at 6.8 K. Neither is seen to be pressure dependent. As this setup achieved only low pressures a second pressure cell was setup, the data taken is shown in Figure 5.5. The coils in this setup were not counterwound by accident. However, superconducting transitions of the sample and the lead manometer can be determined from the data. It can also be seen that this data has a lower signal to noise ration and random spikes in the data which are a consequence of the pick-up and compensation coil not being counterwound. In Figure 5.5 a feature again can be seen around 6.8 K (though the feature is seen as a peak compared to a step in Figure 5.4). This setup worked up to 9 GPa, the highest pressure reached.

Figure 5.6 shows the superconducting transition temperatures (taken from the centre of the transition) as a function of pressure for data measured in both the counterwound (Figure 5.4) and non-counterwound (Figure 5.5) pressure cells. The feature seen around 6.2 K and 6.8 K have not been included as it seems highly dependent on the setup and from the results taken can not be linked to the SDW transition. From the results of the superconducting transition temperature an increase is seen up the maximum pressure measured of 8.5 GPa. The previous pressure study also showed an increasing superconducting transition temperature with increasing pressure, the results of which have also been included on Figure 5.6. These results are in good agreement with each other however higher pressure are needed to be obtained in order to determine the maximum transition temperature as well as the critical pressure for this system.

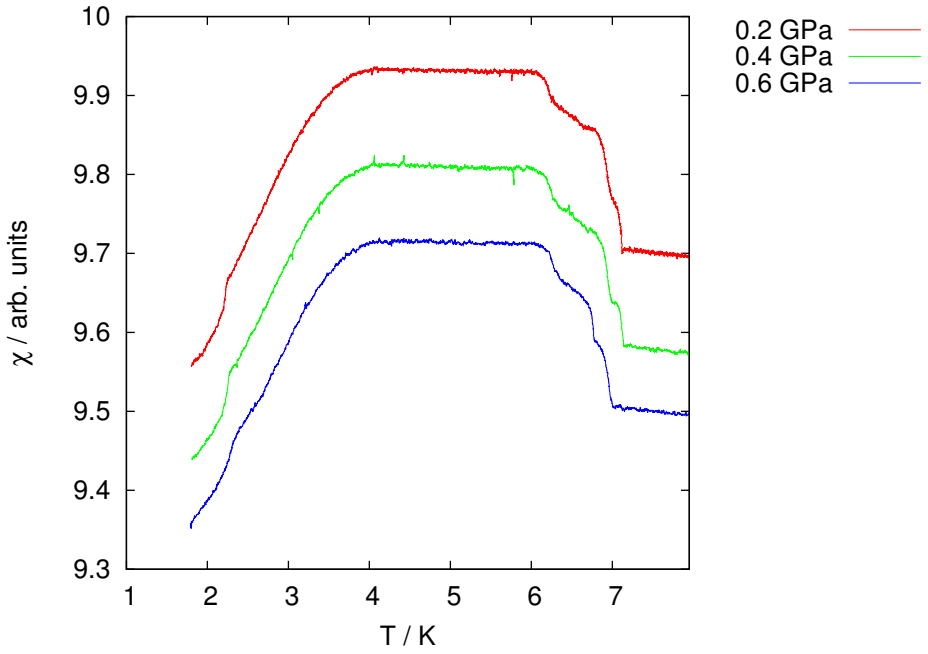

Figure 5.4: Pressure evolution of the magnetic susceptibility of Mo_3Sb_7 . The susceptometer contained couterwound pick-up and compensation coils. Signatures can be seen for the superconducting transition of Mo_3Sb_7 , T_C, (an upward step at 2.4 ± 0.2 K) as well as the superconducting transition of the Pb manometer (A downward step at 7 ± 0.5 K). In addition three systematic features are seen. The first a change in gradient below 4 K. The second and third are two downward step at 6.0 K and 6.8 K. An increase in T_C is seen with increasing pressure and no change is seen in the systematic temperatures.

5.4 Conclusion

High pressure measurements were taken on Mo_3Sb_7 extended the phase diagram initially reported by V.H. Tran et.al. [81]. Results have shown the superconducting transition of Mo_3Sb_7 increase from the zero pressure critical temperature of $T_C = 2.1$ K to 3.4 ± 0.3 K at the maximum pressure measured of 8.6 GPa. No results could be drawn on the SDW transition reported by V.H. Tran and the structural transition was not looked at. To continue this study the features seen in the data around 6.8 K and 6.2 K (Figures 5.4 and 5.5) need to be studied further to determine if they are related to the SDW transition.

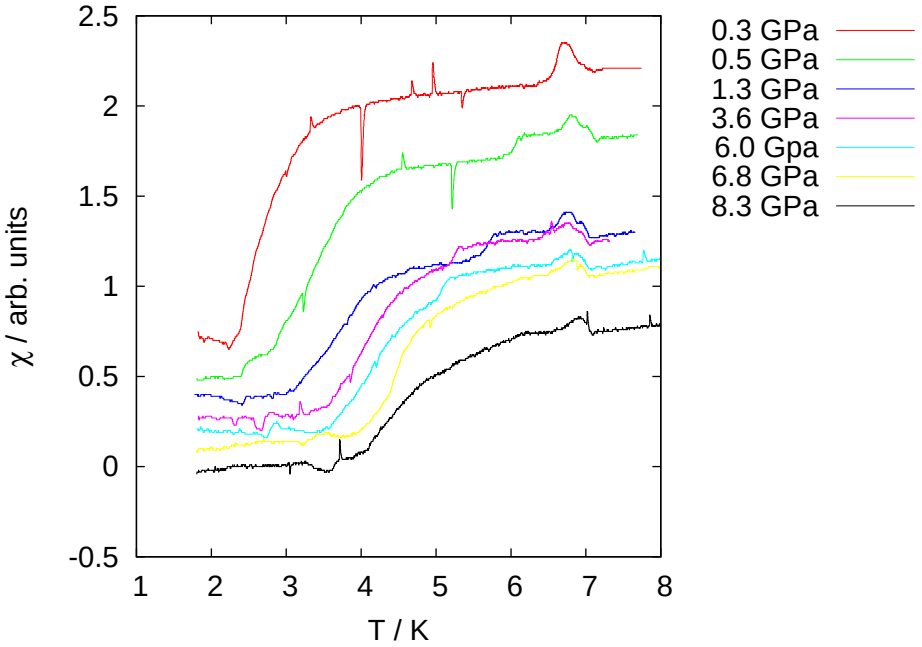

Figure 5.5: Pressure evolution of the magnetic susceptibility, χ of Mo_3Sb_7 . The susceptometer included pick-up and compensation coils which were not counterwound, leading to increased noise and spikes in the data. Signatures can be seen for the superconducting transition of Mo_3Sb_7 , T_C, (an upward step between 2.1 K and 3.4 K) as well as the superconducting transition of the Pb manometer (A downward step from 7 K to 4 K). In addition two systematic features are seen. The first a change in gradient initially below 4 K up to 6 K at the highest pressures. The second a peak in the data at 6.8 K. The results show T_C increasing with pressure. The onset of the gradient change also increases with pressure. The featyre at 6.8 K does not seem to be pressure dependent.

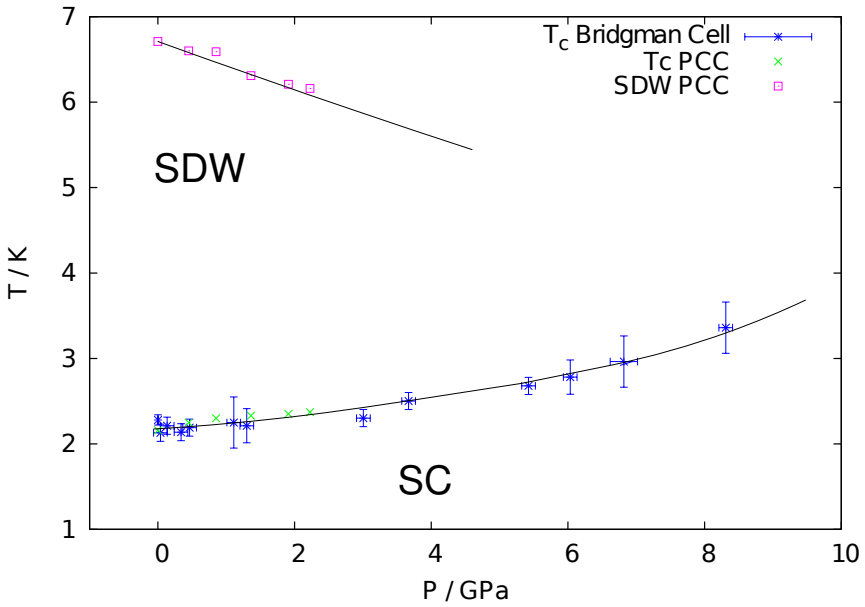

Figure 5.6: Extended pressure-temperature phase diagram of Mo_3Sb_7 showing the pressure dependence of the superconducting and SDW transitions. The susceptibility measurements in a Bridgman anvil cell were performed by the author and the results from resistivity and magnetisation in a piston cylinder cell (PCC) were obtained from V.H. Tran et.al. [81]

Chapter 6

$\mathbf{Nb}_{1-y}\mathbf{Fe}_{2+y}$

6.1 Abstract

$Nb_{1-y}Fe_{2+y}$ offers an opportunity to study both a Ising ferromagnet near a quantum phase transition and a modulated magnetic phase. The work presented in the following sections shows the results for two different compositions of of $Nb_{1-y}Fe_{2+y}$. One is near stoichiometry and shows only modulated magnetic ordering the second is iron rich and is an Ising ferromagnet in the ground state and the modulated magnetic order at higher temperatures. Motivation includes studying the magnetic phase diagram of iron rich of $Nb_{1-y}Fe_{2+y}$, with possible phase diagram is presented in Figure 6.1 and gaining a better understanding of the modulated magnetic phase. Results from susceptibility and resistivity measurements of the ferromagnetic phase has shown that the ground state may not be a simple Ising ferromagnet but instead a coexistance of the modulated phase and the ferromagnetic phase. Measurements of the resisitivity under pressure have shown that the ferromagnetic phase is suppressed under pressure and the critical pressure was achieved. Comparison with the chemical doping results shows good agreement between pressure and chemical doping measurements, suggesting that the change of lattice parameter is the main contribution in both phase diagrams. The modulated phase was shown to be suppressed with increasing pressure however the critical pressure could not be achieved. Power law analyses has shown non-Fermi liquid behaviour over all pressures measured.

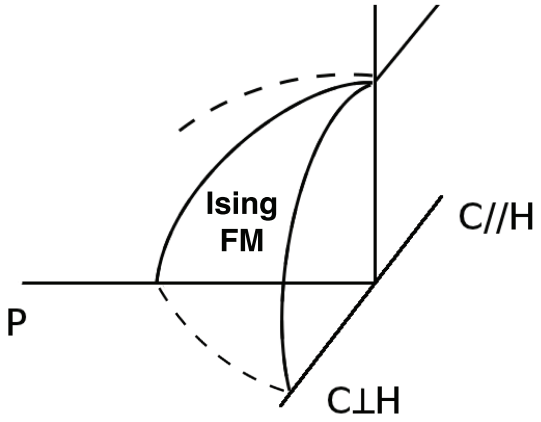

Figure 6.1: Schematic phase diagram of single crystal $NbFe_2$ in the Ising Ferromagnetic state tuned with field and pressure.

6.2 Introduction

The metallic system Nb_{1-y} Fe_{2+y} has shown a very rich phase diagram and unconventional physical properties over a very small doping range. This includes marginal Fermi liquid behavior characteristic of ferromagnetic quantum criticality [82]. Recently a number of single crystals have been grown of various compositions allowing for a confirmation and extension of our understanding of the unconventional properties of Nb_{1-y} Fe_{2+y}.

6.2.1 Structure of $NbFe_2$

$NbFe_2$ has the C14 Laves $MgCu_2$ crystal structure (space group $P6_3/mmc$) in the homogeneity range of $27.4 \leq Nb\% \leq 36.3$ [83].

The structure consists of iron Kagome planes stacked normal to the c-axis. Between these planes are iron and niobium atoms that form tetrahedra with the iron atoms in the Kagome planes, as seen in Figure 6.2. From neutron studies, x-ray measurements and Mössbauer measurements of AFe_2 systems (where A is a transition metal of rare earth metal) doping with both A and Fe is by direct substitution [84, 85, 86]. Excess A atoms occupy Fe sites causing an expansion around the defect and excess Fe occupying the A sites with a contraction around the defect.

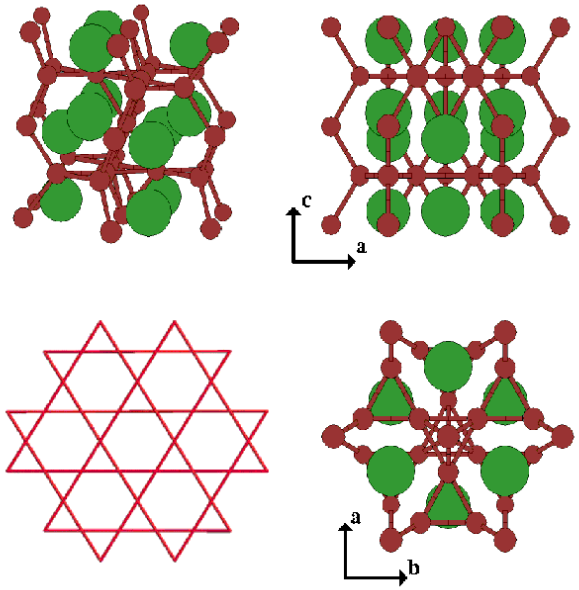

Figure 6.2: Crystal structure of $NbFe_2$ with iron atoms shown in red and niobium atoms shown in green. Bottom left figure shows the Kagome lattice formed in planes by the iron atoms.

6.2.2 Phase Diagram of of $Nb_{1-y}Fe_{2+y}$

Several previous studies have produced chemical phase diagram. The first to study the low temperature phases studied several polycrystalline samples (y = -0.04,-0.02,0,0.02 and0.04) using nuclear magnetic resonance (NMR) and DC magnetisation [87]. The phase diagram is shown in Figure 6.3(a). This shows two ferromagnetic phases either side of stoichiometry. The ground state at y=0 is shown as paramagnetic. A later study by the same group identified a magnetic state around stoichiometry, which was suggested to be a weak antiferromagnet. This was ascertained from a maximum in the susceptibility around 10 K and 0.31 T and a line broadening in the NMR seen below this temperature [88]. Measurements of other ferromagnetic samples in this study showed good agreement with the previous study, 6.3(b). A phase diagram in 1995 shows much higher transition temperatures than the previous reports and shows no paramagnetic ground state. The ground state at stoichimetry is again reported as antiferromagnetic. Between the ferromagnetic

phase and antiferromagnetic phase a mixed state is observed where both antiferromagnetic and ferromagnetic signitures were seem in the magnetic isotherms.

The current compositional phase diagram of of $Nb_{1-y}Fe_{2+y}$ was measured by Moroni et. al. from multiple polycrystaline samples [24]. The composition of the nominally stoichiometric samples was determined from Co-Kα X-ray diffraction (Cu-Kα is absorbed by iron) and wavelength dispersive X-ray spectroscopy (WXDS). The lattice parameters were within 0.001 Å of other measurements [47]. The transition temperatures were determined using magnetic measurements and the phase diagram is shown in Figure 6.3(d). The iron rich side of the phase diagram shows an Ising ferromagnet with transition temperatures in good agreement with the Yamada studies [87, 88] Figure 6.3(a and b). A Heisenberg ferromagnetic ground state is seen on the Nb rich side which suppresses to a quantum phase transition at $y = -0.018$. Beyond the quantum phase transition a magnetic state emerges, which is possible modulated, is the ground of the system till $y = 0$ and is measured up to $y = 0.017$. In this study it is labeled as a spin density wave, SDW in the compositional phase diagram, Figure 6.3(d).

6.2.3 Magnetic ordering around y=0

The magnetic ordering around stoichiometry was first postulated to be helical, similar to $MnAu_2$ [90]. This is following an NMR study on stoichiometric $NbFe_2$ which found both ferromagnetic and antiferromagnetic spin fluctuations and a large distribution on internal fields at the ^{95}Nb sites. This scenario was supported by an estimation taken for the ordering wave vector, $\mathbf{Q}$ of 0.05 Å^{-1}. This was obtained from the expression $\chi_q^{-1} = c(q - \mathbf{Q})^2$ where $\chi_q^{-1} \approx 0.02$ is the magnitude of the peak in the AC susceptibility and c was taken for inelastic neutron scattering data on $ZrZn_2$ [91]. Results from small angle neutron measurements [92] and large angle neutron measurements [1] have seen no sign of magnetic order in the modulated magnetic state. At stoichiometry another magnetic state is seen as the ground state. This is originally measured by NMR as an Ising ferromagnet [88]. Recent spin- dependent Compton scattering measurements (performed at 2.5 T) for a single crystal iron rich sample of $NbFe_2$ suggest that the ground state is

ferrimagnetic [93]. The predicted spin state and the results are shown in Figure 6.4. This agrees with recent band structure calculations which have determined the ground state of the stoichiometric sample to be ferrimagnetic [94].

6.2.4 High Pressure Studies

Several high pressure studies have been performed. The first an NMR measurement performed by Yamada et.al. up to 3 GPa [95] of an iron rich (y=0.01), niobium rich (y=-0.02) and a stoichiometirc polycrstalline sample. The Heisenberg ferromagnetic phase of the niobrium rich sample was quickly suppressed in pressure. Similarly the iron rich Ising ferromagnetic phase was suppressed under pressure however was more resilient than the niobium rich Heisenberg ferromagnet and the critical pressure was not reached. The stoichiometric sample showed a narrowing of the line width with increasing pressure suggesting the modulated phase was being suppressed with increasing pressure. Three further studies have been performed by C. Albrecht, D. Moroni and W. Duncan as part of their theses, who are former members of the Royal Holloway group [96, 47, 1]. All measurements were resisitivity measurements performed in a piston cylinder cell and the maximum pressure reached was 3 GPa. Two niobium rich samples were looked at (y=-0.035 and -0.02) which again showed suppression of the ferromagnetic phase. A slightly niobium rich sample (y=0.0117) is near the quantum phase transition and showed long range linear temperature dependence of the resistivity at low temperatures. This decreased with increasing pressure. Two near stoichiometric samples (y=0 and y=0.007) showed that the modulated phase is suppressed with applied field however the critical pressure was not achieved. Finally an iron rich sample was measured (y=0.0157) showing a suppression of the ferromagnetic phase. In difference to the Yamada study [95] the iron rich ferromagnetism was seen to suppress quicker than the niobium rich ferromagnetism though in both cases the critical pressure was not reached.

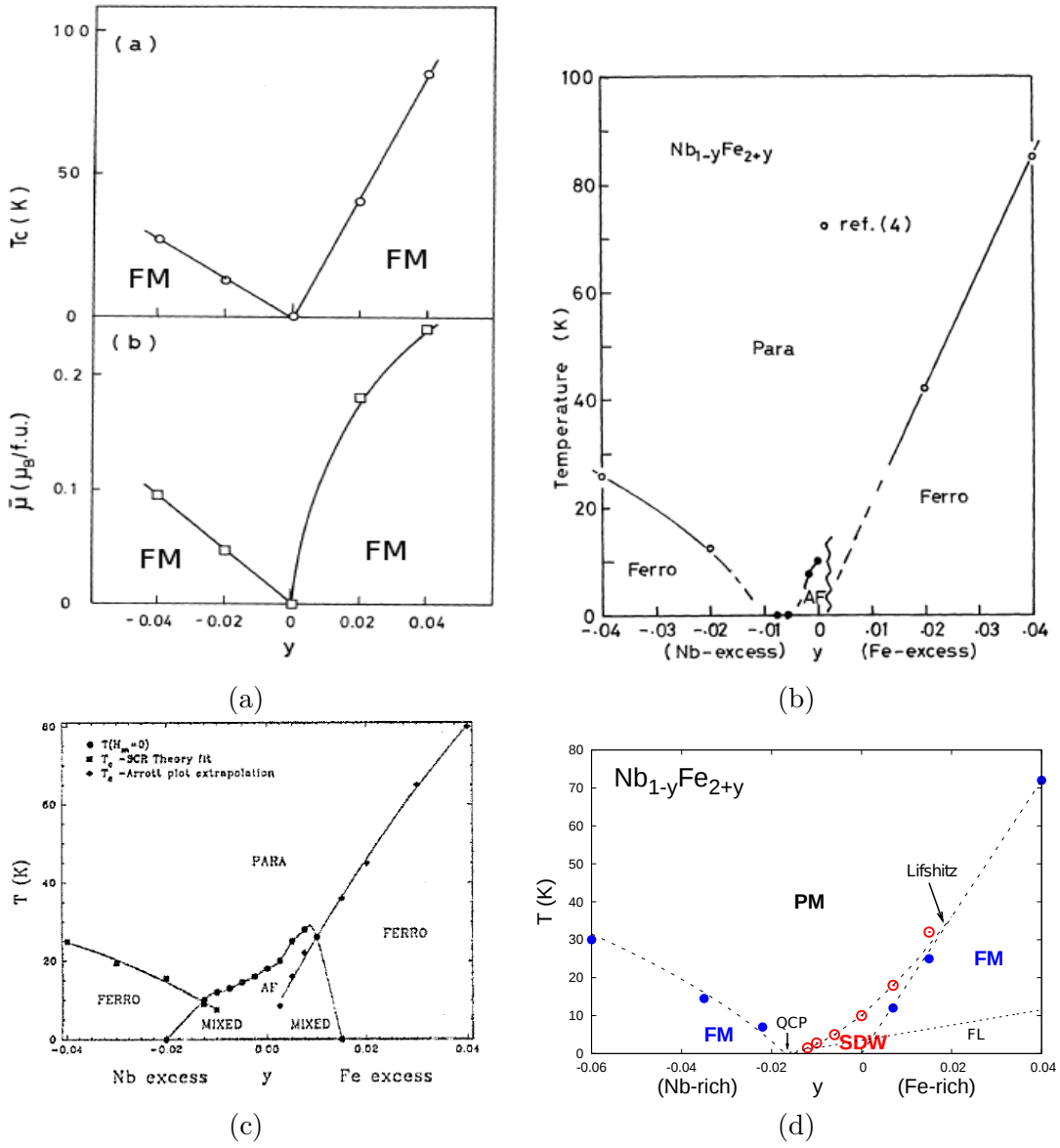

Figure 6.3: Presented are several chemical phase diagrams of of $Nb_{1-y}Fe_{2+y}$. (a) shows the study by Yamada et. al. in 1987 [87] showing two ferromagnetic (FM) phases either side of stoichiometry. The ground state as stoichiometry was stated as paramagnetic (PM). (b) shows a later study by Yamada et.al. in 1988 [88]. This study saw a weak antiferromagnetic state (AFM) as the ground state at stoichiometry. Measurements of the ferromagnetism agreed with previous study. (c) Shows a study by Crook et.al. in 1995 [89]. The ground state at stoichiometry is reported as antiferromagnetic and between the antiferromagnetic state and ferromagnetic state a mixed state was measured where signitures of antiferromagnetism and ferromagnetism were observed. Current phase diagram taken from many polycrystalline samples using magnetisation and magnetic susceptibility measurements [24]. Results show a modulated magnetic state as the ground state (SDW).

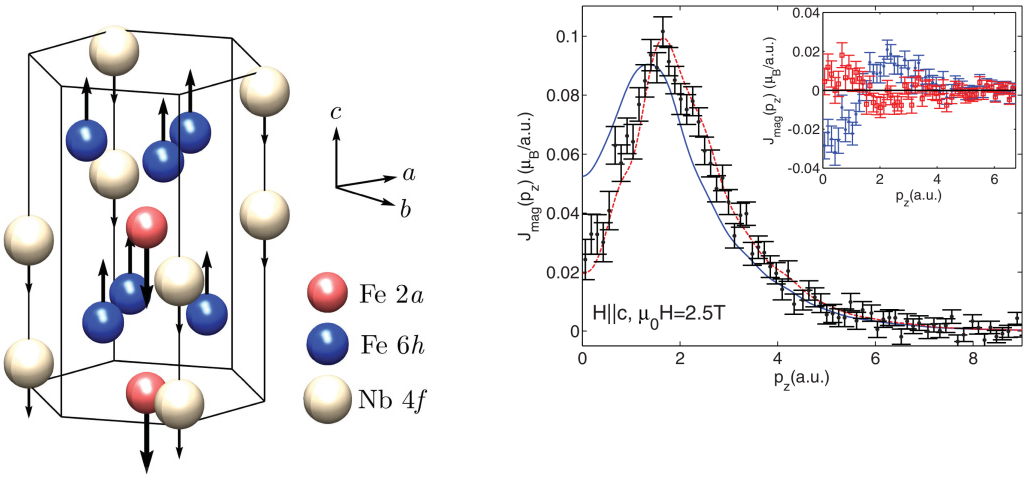

(a) (b)

Figure 6.4: (a) $NbFe_2$ in the ferrimagnetic state predicted by LMTO calculation. The arrows on the atomic sites indicate the relative sizes and directions of the respective moments. (b) Experimental $Nb_{0.985}Fe_{2.015}$ magnetic spin momentum density (black points) projected along the [0001] crystal direction, plotted together with LMTO ferrimagnetic calculation (red dashed line) and ferromagnetic calculation (blue solid line). Both the calculated LMTO profiles have been normalized to the same total spin moment (area). The inset shows difference plots for the experimental data minus each theoretical profile, again with the ferrimagnetic (ferromagnetic) case plotted as red squares (blue points) [93].

6.3 Single Crystals

Single crystals were grown by A. Neubauer and W. Duncan at the Technical University of Munich under the group of Prof. Christian Pfleiderer. A specially designed optical floating zone (OFZ) furnace was used with an ultra high vacuum (UHV) capability for the growth of intermetallic crystals [97]. Several crystals of varying composition were grown of which two have been studied in this thesis. A sample close to stoichiometric with composition $Nb_{0.9980}Fe_{2.0020}$ and OFZ28, an iron rich sample has a composition $Nb_{0.9853}Fe_{2.0147}$. Neutron studies of the crystals were done by Andreas Neubauer and the technicians at the crystal lab at the Technical University of Munich. Neutron diffraction was done with Björn Pedersen at the Reciprocal Space Investigator (RESI) which showed high quality single crystal with lattice parameters determined and shown in Table 6.1. Depolarization analysis was conducted with Vladimir Hutanu at the Hot single crystal Diffractometer (HIEDI) along with AC susceptibility measurements revealed well-defined homogeneous magnetic phase transitions from which the composition was determined. Both neutron instruments are located at the FRM2 in Munich.

Table 6.1: Sample labeling, nominal composition and measured parameters of $Nb_{1-y}Fe_{2+y}$ samples studied in this thesis.

Growth label	Nominal y	m_i / mg	δ m / mg	observed y
OFZ11	0	14350.8	N/A	+0.0020
OFZ28	+0.010	21790	37.8	+0.0156
Growth label	y / Å	c / Å	V / 10^6pm^3	Mosaicity
OFZ11	4.85	7.86	13.34	1°
OFZ28	4.81	7.94	13.26	0.3°- 0.4°

For the iron rich samle of composition $Nb_{0.9853}Fe_{2.0147}$ two cuts from the grown boule were used in all the measurements presented. X-ray diffraction of were taken and showed very similar results. In Figure 6.5 is measurements taken for the second sample.

The physical properties results presented in the next chapter for the iron rich sample, OFZ28 were taken in collaboration with W. Duncan. Some of the results are reproduced

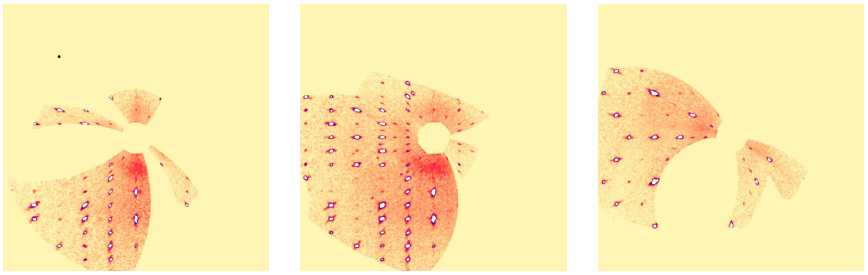

(a) (b) (c)

Figure 6.5: X-ray diffraction images of the orthonormal faces of the single crystal with composition of $Nb_{1-y}Fe_{2+y}$ y=0.0156 (sample OFZ28.4.1) taken with the Oxford Diffraction ltd Xcalibur diffractometer at Royal Holloway. Image (a) shows the (0KL) plane, (b) the (H0L) and (c) the (HK0) plane.

from his thesis [1], which are used to present an alternative interpretation of the data.

6.4 Susceptibility Results for $Nb_{0.9853}Fe_{2.0147}$

Detailed in this section are the magnetic susceptibility results for $Nb_{0.9853}Fe_{2.0147}$. In this section two singles crystals of the same composition were used. These have labels OFZ28.4.1 and OFZ28.4.2 and the crystal used for each measurement is stated.

6.4.1 Temperature Dependence

Figure 6.6 shows the temperature dependence of the real and imaginary components of the magnetic susceptibility of $Nb_{1-y}Fe_{2+y}$ for y=0.0156 and sample OFZ28.4.2, with the excitation field applied parallel to the crystallographic c axis, $H//c$. In the real part of the susceptibility two peaks can be seen one at $T_0 = 29.5 \pm 0.2$ K and the other at $T_C = 22.0 \pm 0.2$ K. T_C is the Curie temperature marking the onset of ferromagnetism. Between T_C and T_0 the sample is believed to be in the predicted magnetically modulated state. A peak is seen in the imaginary part of the susceptibility relating to the ferromagnetic phase however there is no corresponding peak at T_0. The zero temperature susceptibility is of the order of 0.02, this corresponds to a Stoner enhancement factor $\chi/\chi_0 \approx 180$ where $\chi_0 \approx 10^{-4}$ is the susceptibility estimated from the calculated bare band structure of the density of states [98]. Several temperature sweeps in fixed magnetic fields below 0.5 T were also measured for $H//c$ and $H \perp c$. The results for the real component of the magnetic susceptibility are shown in Figure 6.7. For the orientation $H//c$ two peaks in the data are seen below 0.05 T. The peak at lower temperatures is seen to increase with increasing magnetic field while the peak initially at 29.5 ± 0.4 K decreases with increasing field. At 0.05 T only a single peak of a magnitude larger than the two peaks seen at lower and higher fields. At higher fields a peak of magnitude comparable to the original peaks is seen in addition to a shoulder in the data. In the $H \perp c$ results a peak is seen seen 22 ± 0.3 K at zero field which increases slightly up to 0.1T. A shoulder is seen around 30 ± 0.5 K at zero magnetic field. As with the $H//c$ case this feature is seen to decrease in temperature with increasing field however the change in temperature is much smaller over the same change in field.

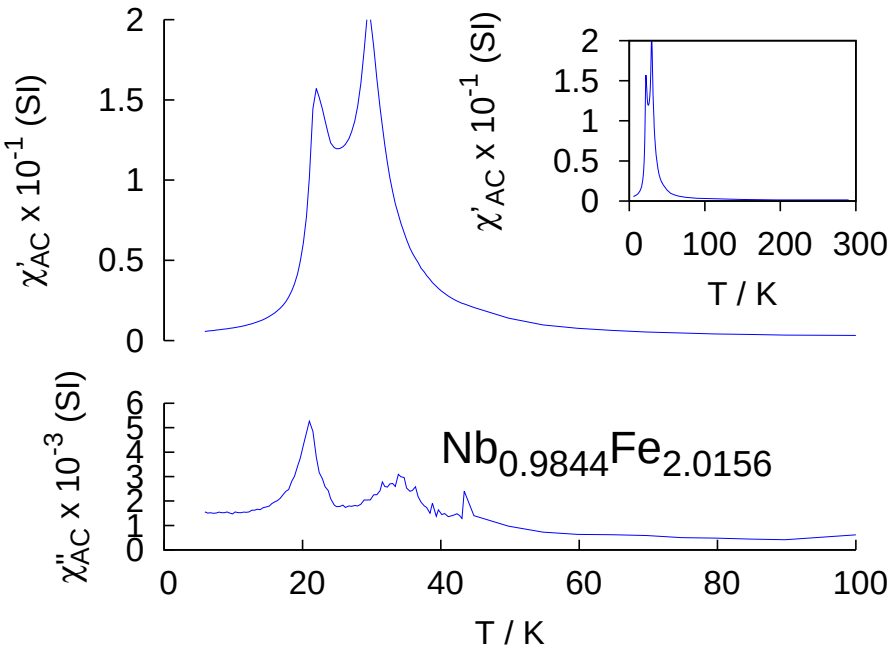

Figure 6.6: Temperature dependence of the magnetic susceptibility of $Nb_{0.9853}Fe_{2.0147}$ (sample OFZ28.4.2) with $H//c$. Plot shows the real, χ' and the imaginary χ" parts of the susceptibility with an applied excitation field of 10^{-4} T [1]. Peaks can be seen at 22.0 ± 0.2 K and 29.5 ± 0.2 K relating to the ferromagnetic T_C and modulated, T_0 phase transitions respectively. Insert shows extended temperature range of the real part of the susceptibility from 0-300 K.

6.4.2 Field Dependence

Figures 6.8 shows the field dependence of the real part of the magnetic susceptibility using sample OFZ28.4.2, for fields applied in both crystalographic directions. Several features can be seen in the magnetic field dependence of the susceptibility. For $H//c$ the central peak shows hysteresis at the lowest temperatures measured. This central peak is no longer observed above 25 K. In the data measured at 4 K a shoulder in the data is seen at 0.3 T, which develops into a peak. The magnitude of this peak increases up to a maximum around 30 K. In the $H \perp c$ case similar features are seen including a small hysteresis curve around the central peak at 1.9 K. This central peak also appears suppressed around 25 K. Another similar feature is a shoulder around 0.3 T at 8 K which develops into a peak as

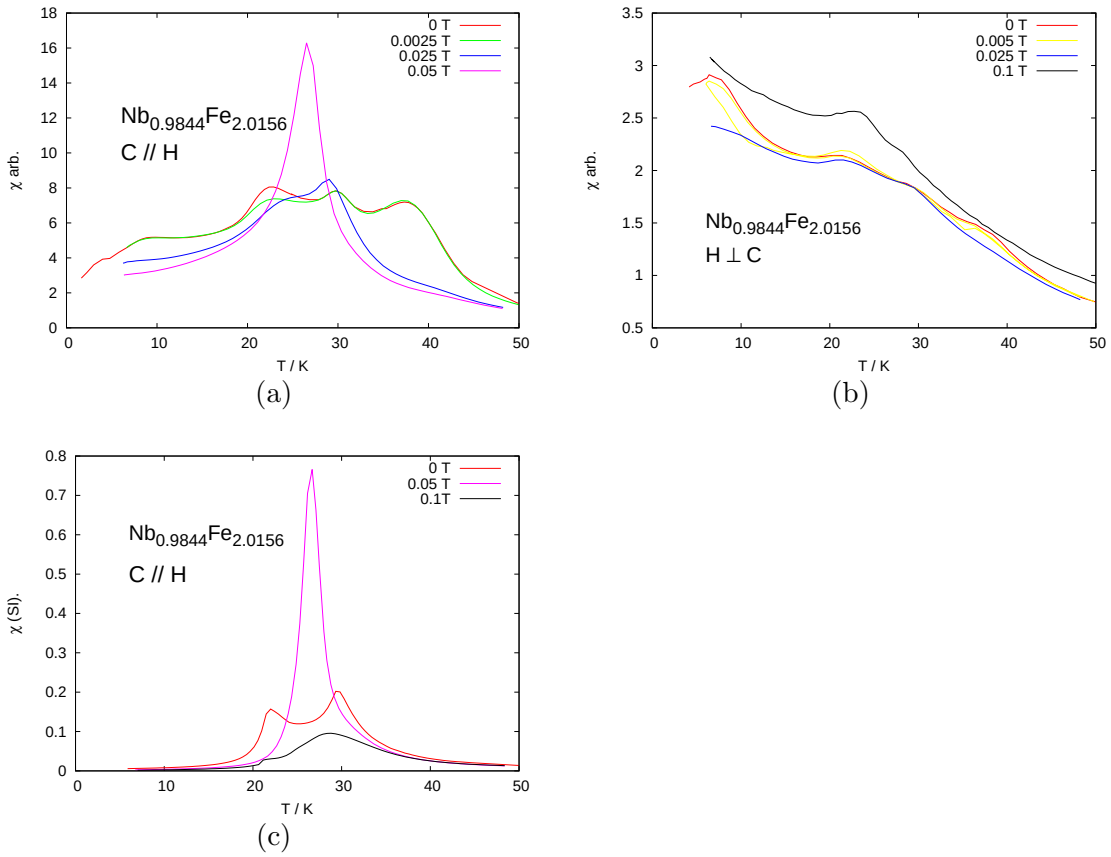

Figure 6.7: Temperature dependence of the magnetic susceptibility of $Nb_{1-y}Fe_{2+y}$ for y=0.0156 for various fixed magnetic fields. Plots (a) and (c) show the magnetic susceptibility for $H//c$ and (b) for $H \perp C$. Plots show the development of the magnetic transitions, seen as peaks and shoulders in the data, in various magnetic fields. For $H//c$ and $H \perp c$ a peak at 22 K in zero field is seen to increase in temperature with increasing field. For $H//c$ a peak at 30 K is seen to decrease in temperature with increasing fields. For $H \perp c$ a shoulder is seen at 30 K that decreases in temperature with increasing field. For both features the change in temperature is larger in the $H//c$ orientation. For $H//c$ at 0.05 T a single peak with a larger magnitude than previous peaks, this appears where the two previous peaks intercept. The measurements were performed on two different crystals with the same composition; (a) and (b) on sample OFZ28.4.1 and (c) on OFZ28.4.2

the magnetic field increases. Additionally a broad shoulder, with an onset of $\approx$ 2.5 T at 1.9 K, is seen in all data below 20 K.

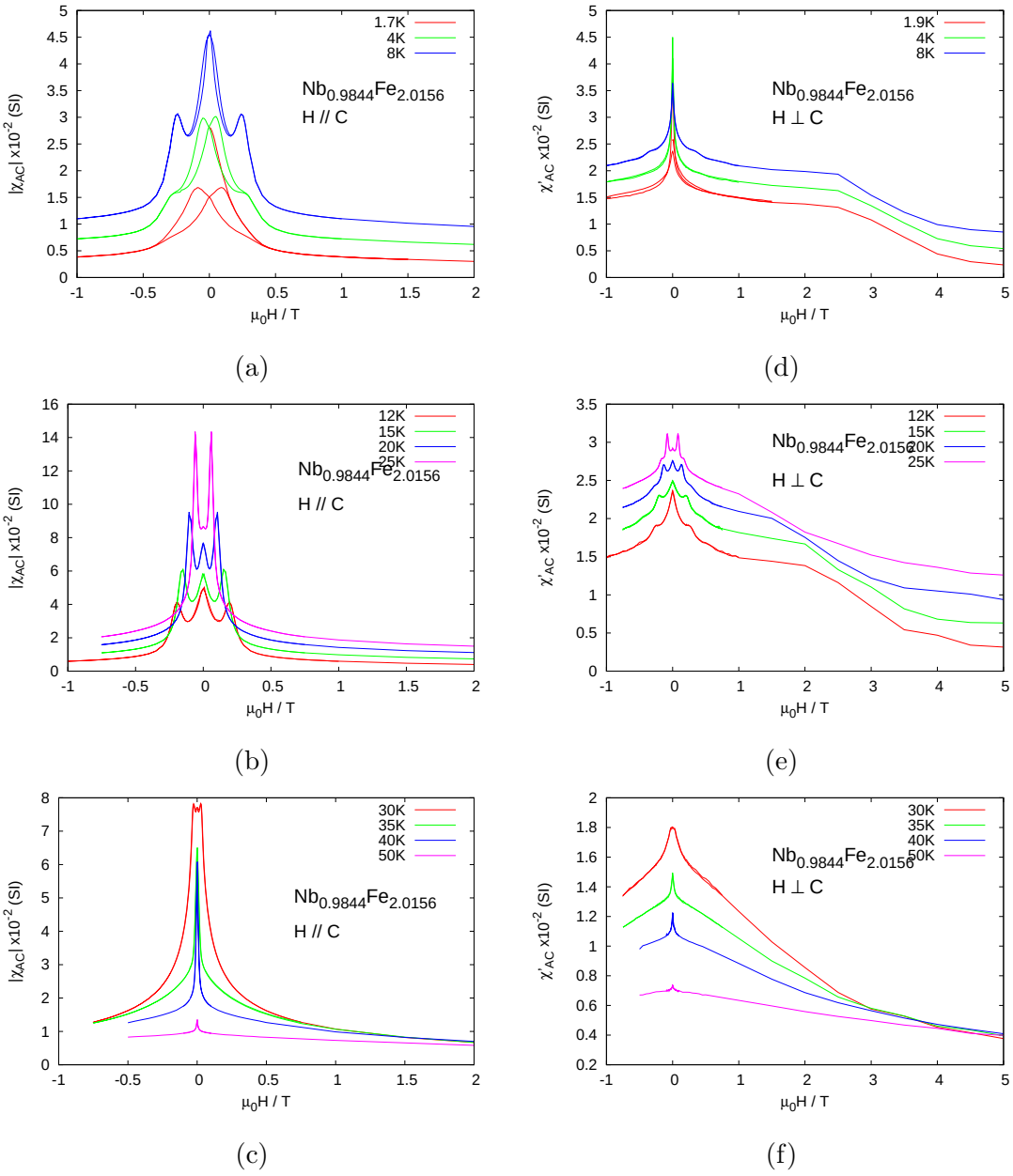

Figure 6.8: Field dependence of the magnetic susceptibility of $Nb_{1-y}Fe_{2+y}$ for y=0.0156. Plots (a),(b), and (c) show the susceptibility for $H//c$ and (d),(e) and, (f) for $H \perp C$. Plots (a) and (d) show the real part of the susceptibility for temperatures below 8 K. Plots (b) and (e) show the field dependence of the real part of the susceptibility between 12 K and 20 K. Plots (c) and (f) show the higher temperature dependencies up to 50 K. Curves in plots (a),(b),(c), and, (d) have been offset for clarity [1].

6.4.3 Partial phase diagram

From the results of magnetic susceptibility a partial field phase diagram can be generated from the susceptibility results. These are shown in Figure 6.9 in both field directions. No labels have yet been associated with each phase, instead each feature is just plotted by measurement type with the evolution of several magnetic phases seen. A discussion on these phases is presented in Section 6.7.1.

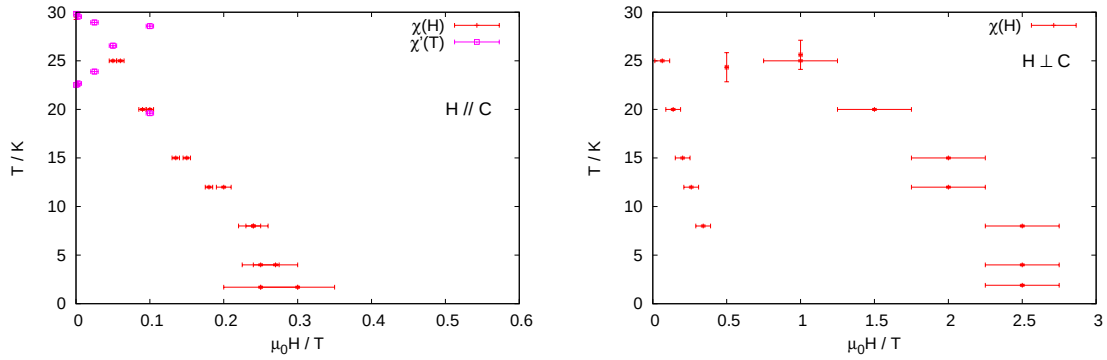

(a) (b)

Figure 6.9: The partial magnetic phase transitions produced from the magnetic susceptibility results of $Nb_{1-y}Fe_{2+y}$ for y=0.0156. Labels show where each point is obtained. Either from peaks in the field dependent susceptibility ,$\chi(H)$ of peaks or shoulders in the temperature dependence of the susceptibility, $\chi(T)$. (a) shows the phase diagram for $H//c$ and (b) $H \perp c$. Results show the evolution of several magnetic phases which are discussed is Section 6.7.1.

6.5 Resistivity Results for H=0

6.5.1 $Nb_{0.9853}Fe_{2.0147}$ (near stoichiometric), $P = 0$

The resistivity of $Nb_{0.9980}Fe_{2.0020}$ is shown in Figure 6.10 taken on a sample of dimesions $7 \times 3 \times 1$ mm with voltage lead seperation of 5 mm. No features are seen in the low temperature regime, suggesting no feature is seen around the modulated phase transition, which is also seen in the literature [82].

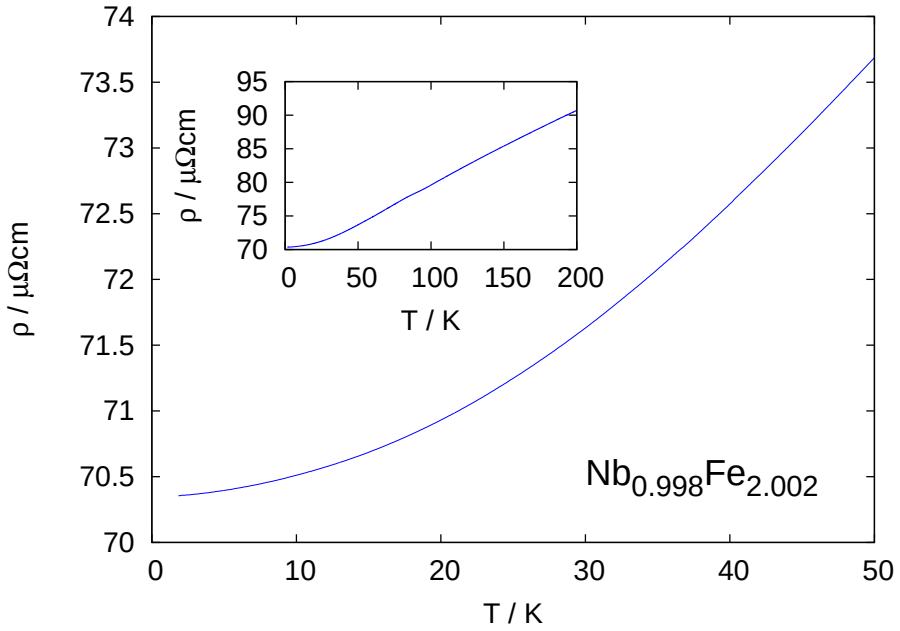

Figure 6.10: Resistivity, $\rho(T)$ of $Nb_{0.9980}Fe_{2.0020}$ with $J//C$ with zero applied magnetic field. Results show that no feature is seen in the resistivity around the modulated phase transition, $T_0 = 22$ K. Insert shows the resistivity over an extended temperature range (0-200 K).

6.5.2 $Nb_{0.9853}Fe_{2.0147}$ (near stoichiometric), $P > 0$

Measurements of $Nb_{0.9980}Fe_{2.0020}$ were carried out in a piston cylinder cell, using the techniques described in Section 3.3.1 with a sample with dimensions $5 \times 1.5 \times 1$ mm and voltage lead seperation of 3.5 mm. Two pressure runs were completed where the temper-

ature and field dependence of the resistivity were measured. In the first run low pressures were achieved and are shown in Figure 6.11. Similar to the zero pressure measurements, Figure 6.10 no features are seen in the resistivity around T_0 and no signals were seen in the derivative of the data. A second pressure run was measured starting at higher pressures however the signal to noise ratio obtained in this second run was significantly lower than that of the first run therefore results for the temperature dependence of the resistivity are not presented. Results are however presented in the magnetic measurements of this sample as the feature seen in the data is significantly larger than the noise and meaningful data can be extracted.

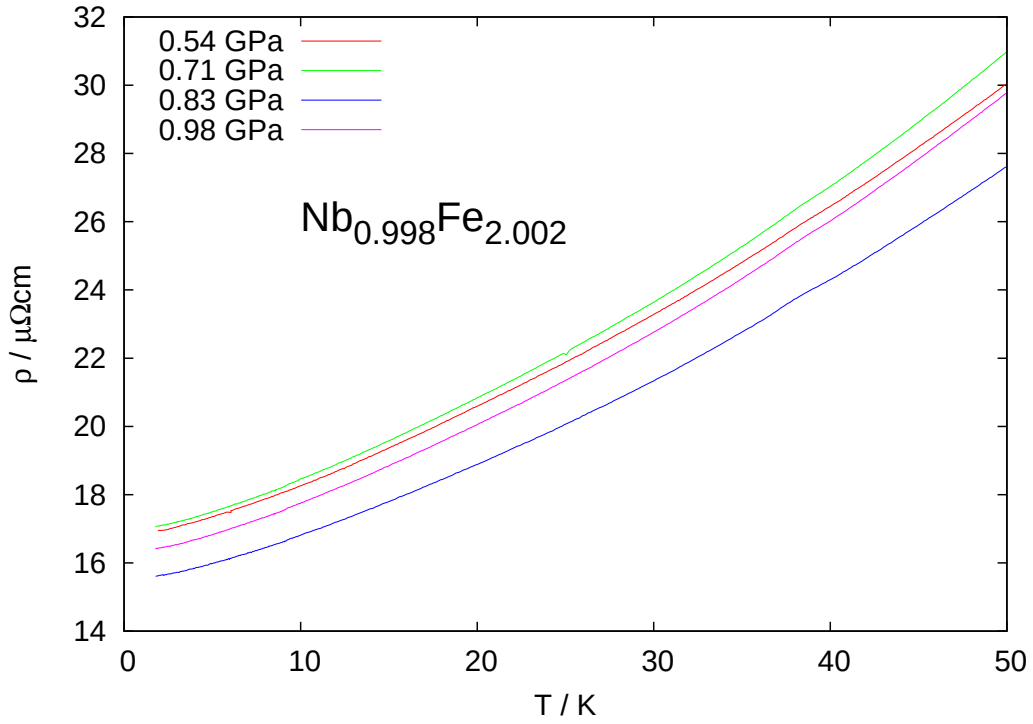

Figure 6.11: Resistivity, $\rho(T)$ as a function of temperature for several pressures of $Nb_{1-y}Fe_{2+y}$ for y=0.002 with $J//c$. Samples were measured in a piston cylinder cell. No features are seen relating to magnetic transitions.

6.5.3 $Nb_{0.9853}Fe_{2.0147}$ (Iron rich), $P = 0$

This section lists the resistivity for $Nb_{0.9853}Fe_{2.0147}$ taken on a sample of dimesions $8 \times 3 \times 1.5$ mm with voltage lead seperation of 5.5 mm. All results were taken from the sample OFZ28.4.1 one of the two samples used for the susceptibility results. Shown in Figure 6.12 is the temperature dependence of the resistivity. A kink can be seen in this dependence at 23.3 ± 0.3 K in both $J \perp c$ and $J//c$, relating to the Curie temperature of the system. The insert of Figure 6.12 which shows the derivative of the data ($d\rho/dT$), shows a clear peak at T_C. As was seen in the $y = 0.002$ resistivity results (Figure 6.11) no feature is seen seen around T_0.

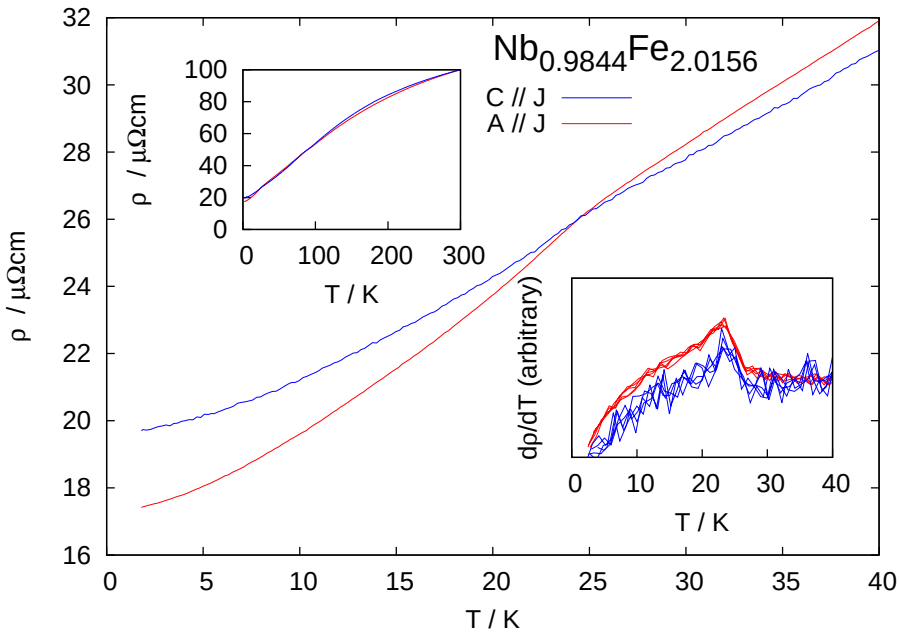

Figure 6.12: Resistivity, $\rho(T)$ of $Nb_{1-y}Fe_{2+y}$ for y=0.0156 as a function of temperature for $C//J$ and $C \perp J$. The lower insert shows the temperature derivative ($\frac{d\rho}{dT}$) of the data with a peak relating to the ferromagnetic transition, T_C seen for both current directions. No feature is observed near the modulated phase transition $T_0 = 22$ K. Upper insert shows an extended temperature range, from 0-300 K [1].

6.5.4 $Nb_{0.9853}Fe_{2.0147}$ (Iron rich), $P > 0$

Resistivity measurements in a Bridgman cell were taken using the four point technique described in Section 3.2.1. Two runs were performed, the first starting at 4.1 GPa and finishing at 16.0 GPa using a sample of size $0.8 \times 0.25.05$ mm. A second run was performed to achieve lower pressures, starting at 1.8 GPa and measured up to 3.9 GPa using a sample of size $0.6 \times 0.2.05$ mm. In both pressure runs the samples were orientated with the same current orientation, J⊥C. The results for low pressures are shown in Figure 6.13 and for high pressures in Figure 6.14. The data at 1.83 GPa of Figure 6.13 has been scaled down as it was significantly higher than the rest of the results. This is probably due to a short that developed above this pressure reducing the signal size. Similarly the 4.6 GPa data Figure 6.14 showed much smaller values than the remaining runs and has been scaled up in the figure. This is probably due to the sample cracking with increased pressure. A plot of the residual resistivity which are not scaled is shown in Figure 6.15.

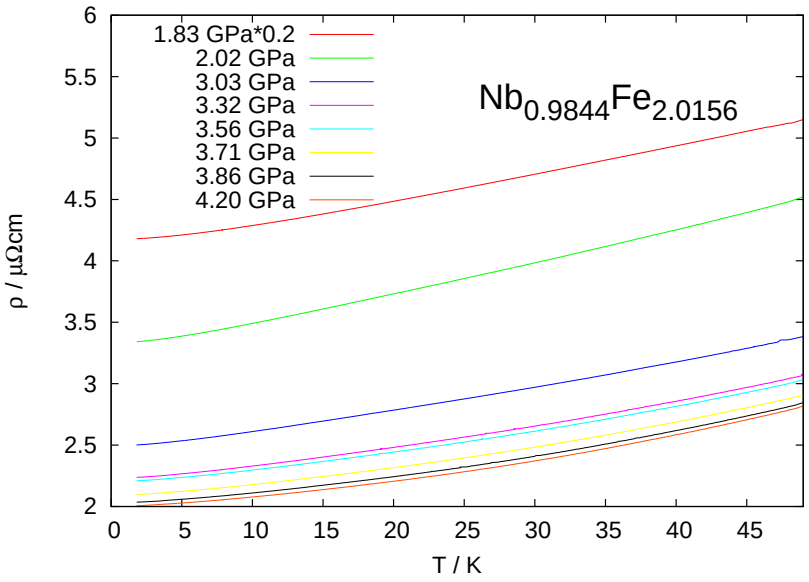

Figure 6.13: Plots of resistivity, ρ against temperature with $J \perp c$ for several low pressures of $Nb_{1-y}Fe_{2+y}$ for y=0.0156. All measurements were performed during the same pressure run in a Bridgman anvil cell. The data for 1.83 GPa has been scaled down.

To determine the transition temperature of the ferromagnetic transition the derivative

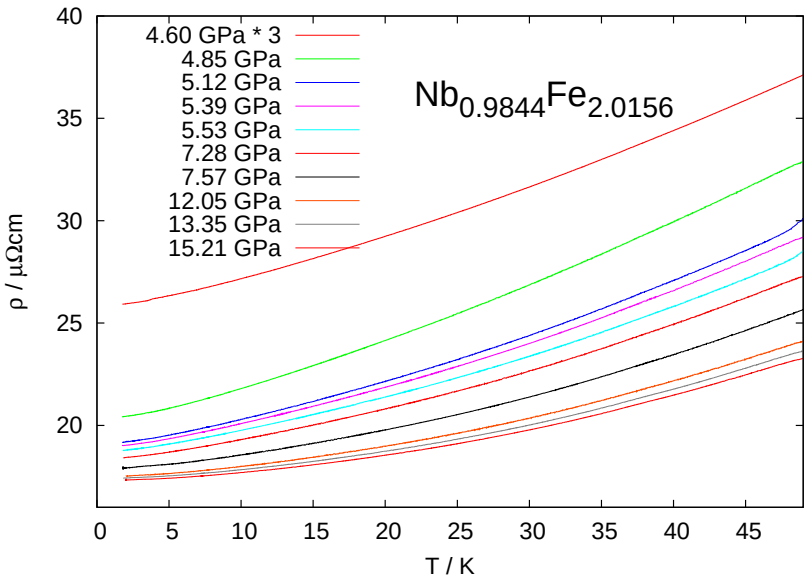

Figure 6.14: Plots of resistivity, ρ against temperature with $J \perp c$ of $Nb_{1-y}Fe_{2+y}$ for y=0.0156. These measurements were taken in a Bridgman anvil cell and show high pressure results. Data for 4.6 GPa have been scaled up. This uses the same setup as Figure 6.13 but are two different pressure runs.

of the data has been studied. Figure 6.16 shows the derivative of the data from Figure 6.13 (for lower pressure results). These results show small broad steps around the ferromagnetic transition, T_C. This is possibly due to a relatively large pressure inhomogeneity in the low pressure run. A transition temperature is dervived from the midpoint of the step. In Figure 6.14 (the results for higher pressures) a kink is seen in the resistivity data for the lowest two pressures. Figure 6.17 shows the temperature derivative for the first three pressures up to 5.4 GPa. A step similar to those seen in Figure 6.13 relating to the ferromagnetic transition. Beyond 5.4 GPa no feature is seen in the temperature derivative of the resistivity which suggests that the ferromagnetic transition is below 1.8 K or had been suppressed.

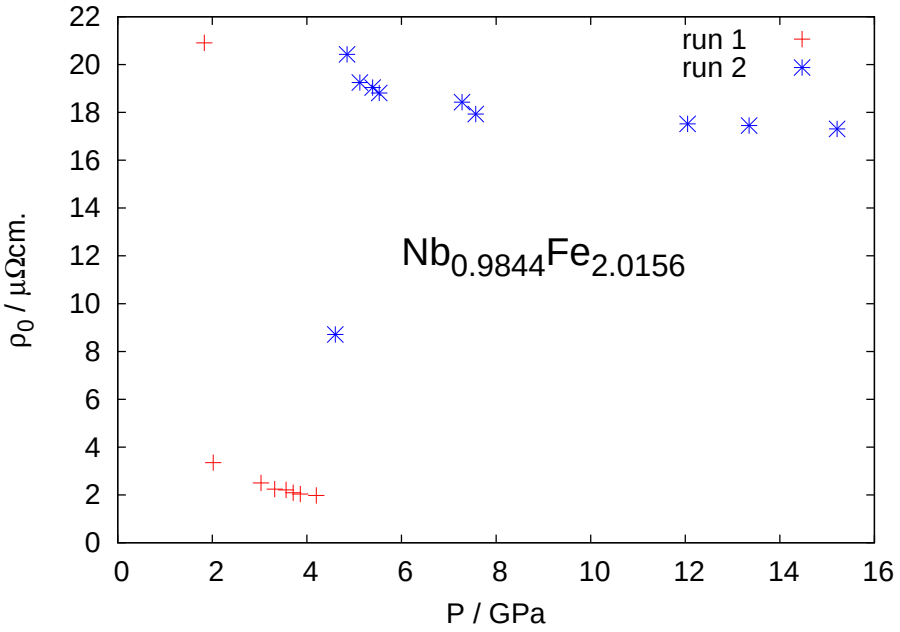

Figure 6.15: Plots of residual resistivity, ρ_0 for the pressure runs shown in Figures 6.13 (run 1) and 6.14 (run 2).

Pressure Phase Diagram for Iron Rich $NbFe_2$

The phase diagram of the ferromagnetic transition, which are derived from the kinks in the high pressure results and from the intercept of the two regions in the derivative of the resistivity for the low pressure results are shown in Figure 6.18. These are plotted alongside a measurement of a polycrystaline sample of stoichiometry $y = 0.0158$ and transitions $T_0 = 29.9$ K and $T_C = 24.4$ K which was measured in a piston cylinder cell [1]. The single crystal and polycrystal samples have a stoichiometry difference of, $\Delta y = 0.0002$ (OFZ28.4 $y = 0.0156$) and difference of transition temperatures of $\Delta T_0 = 1.9$ K (OFZ28.4 $T_0 = 28.0$ K) and $\Delta T_C = 2.9$ K (OFZ28.4 $T_C = 21.5$ K). Therefore a reasonable comparison between the polycrystaline and single crystal results is possible. It can be seen in the region of 1.5-2.2 GPa where the data overlaps there is good agreement between the results. The original analysis of the pressure results was a linear suppression with a possible critical end point at around 3.0 GPa. With both data sets together a linear fit is

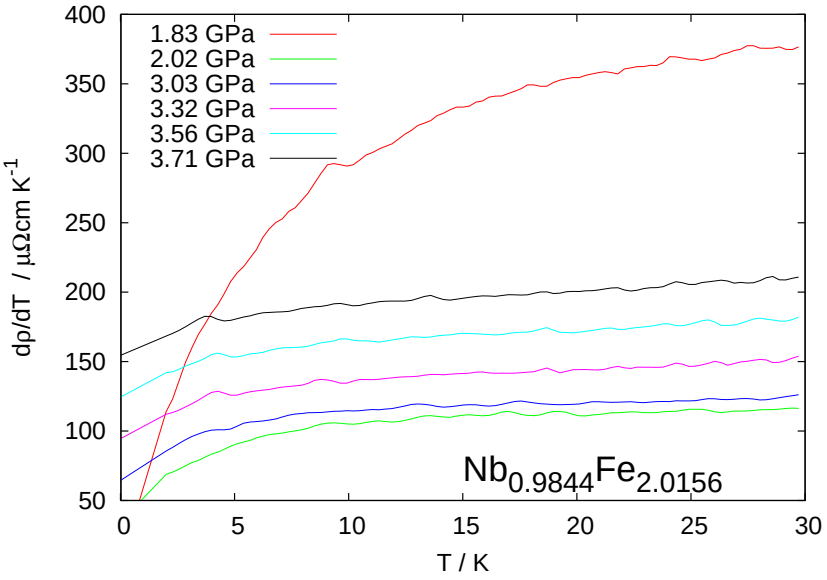

Figure 6.16: Plot of the temperature derivative of the resistivity dρ/dT of $Nb_{1-y}Fe_{2+y}$ for y=0.0156 at varying pressures with $J \perp c$. The ferromagnetic transition, T_C is seen as a step in the data. It can be seen T_C decreases with increasing pressure.

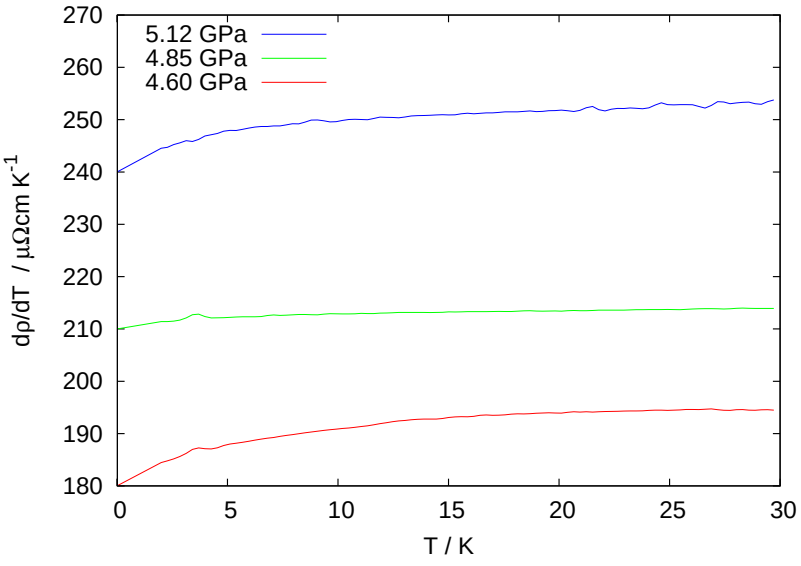

Figure 6.17: Plot of derivative of the resistivity dρ/dT of $Nb_{1-y}Fe_{2+y}$ for y=0.0156 with $J//c$ under pressure. Derivative data is taken from Figure 6.14.

no longer appropriate for the data.

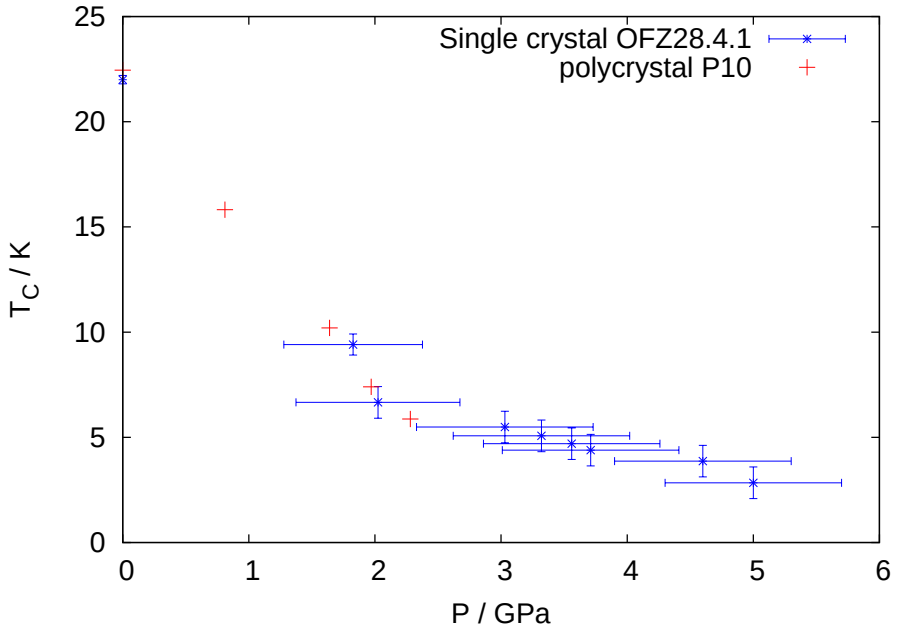

Figure 6.18: Phase diagram of the ferromagnetic transition temperature derived from resistivity results of $Nb_{1-y}Fe_{2+y}$ for y=0.0156 ± 0.0002. Results have been obtained from single crystal OFZ28.4.1 measured in a Bridgman anvil cell and polycrystalline sample P10 [1] measured in a piston cylinder cell.

6.6 Resistivity for $H > 0$

This section details resistivity results obtained on both samples when an external magnetic field was applied.

6.6.1 $Nb_{0.9980}Fe_{2.0020}$ (near stoichiometry), $P = 0$

The magnetoresistance of $Nb_{0.9980}Fe_{2.0020}$ is shown in Figure 6.19 for several temperatures below 50 K. The magnetoresistance curves show a peak close to zero field. However hysteresis with increasing magnitude towards lower temperature is observed in both field directions. In general, the magnetoresistance drops rapidly at low fields and flattens off at higher fields. These sudden onset of GMR has been postulated to be at the critical field of the modulated phase [82].

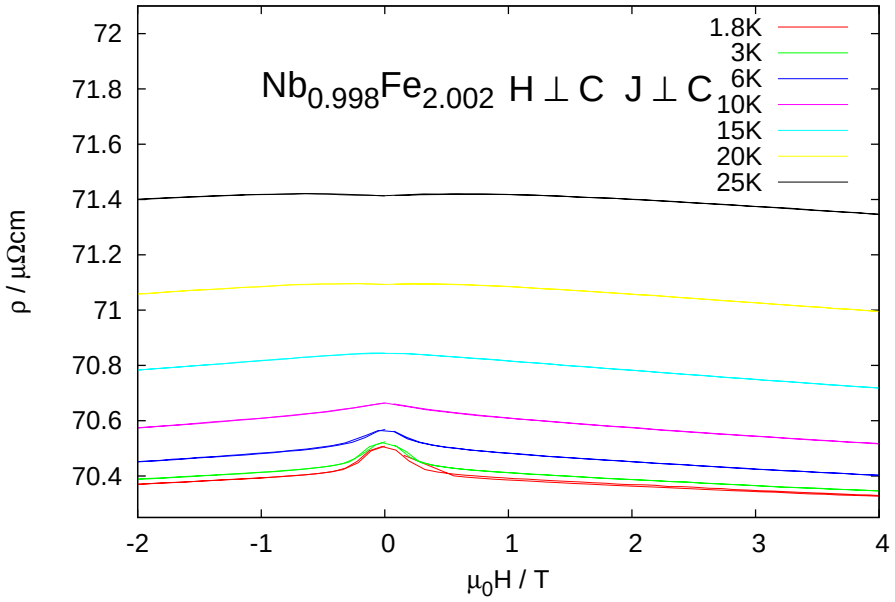

Figure 6.19: Magnetoresistance measurements of $Nb_{1-y}Fe_{2+y}$ with y=0.0020 performed on a sample mounted with $H \perp c$ and $J \perp c$. A sharp upturn in the resistivity with decreasing fields is seen below 15 K.

6.6.2 $Nb_{0.9980}Fe_{2.0020}$ (near stoichiometry), $P > 0$

The results for the low pressure magnetoresistance for $Nb_{0.9980}Fe_{2.0020}$ are presented in Figure 6.20. The results for the higher pressure measurements are presented in Figure 6.21. Due to the reduced signal to noise ratio in these measurements data was only taken to 2 T. The results from these two plots show a similar signature to the zero pressure data, Figure 6.19 a rapid drop in magnetoresistance is seen at low fields. The onset of this feature is seen decrease in field for increasing pressures.

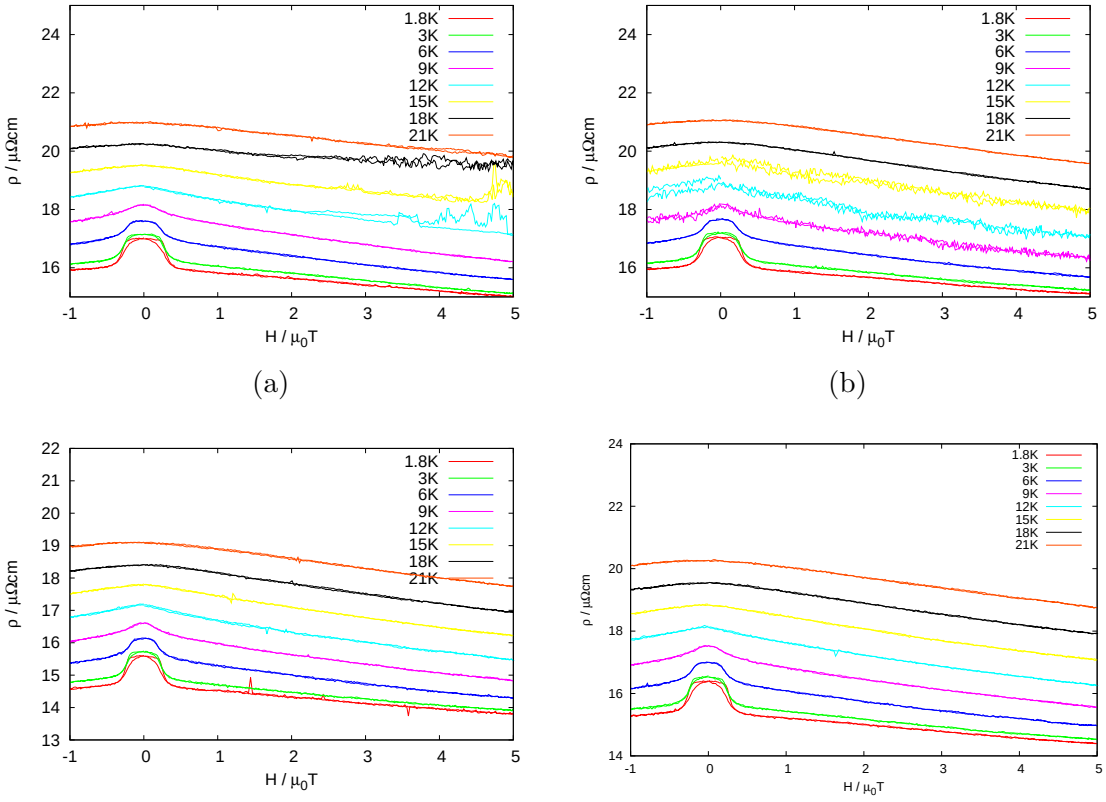

Figure 6.20: Magnetoresistance curves of $Nb_{1-y}Fe_{2+y}$ for y=0.002 measured in a piston cylinder cell with $H//c$ and $J//c$. (a) 0.54 GPa, (b) 0.71 GPa, (c) 0.83 GPa, (d) 0.98 GPa

To determine the modulated phase transition temperature as a function of magnetic field, $T_0(H)$ the positions of the minima in the field derivative, $\frac{d\rho}{dH}$ of the magnetoresistance

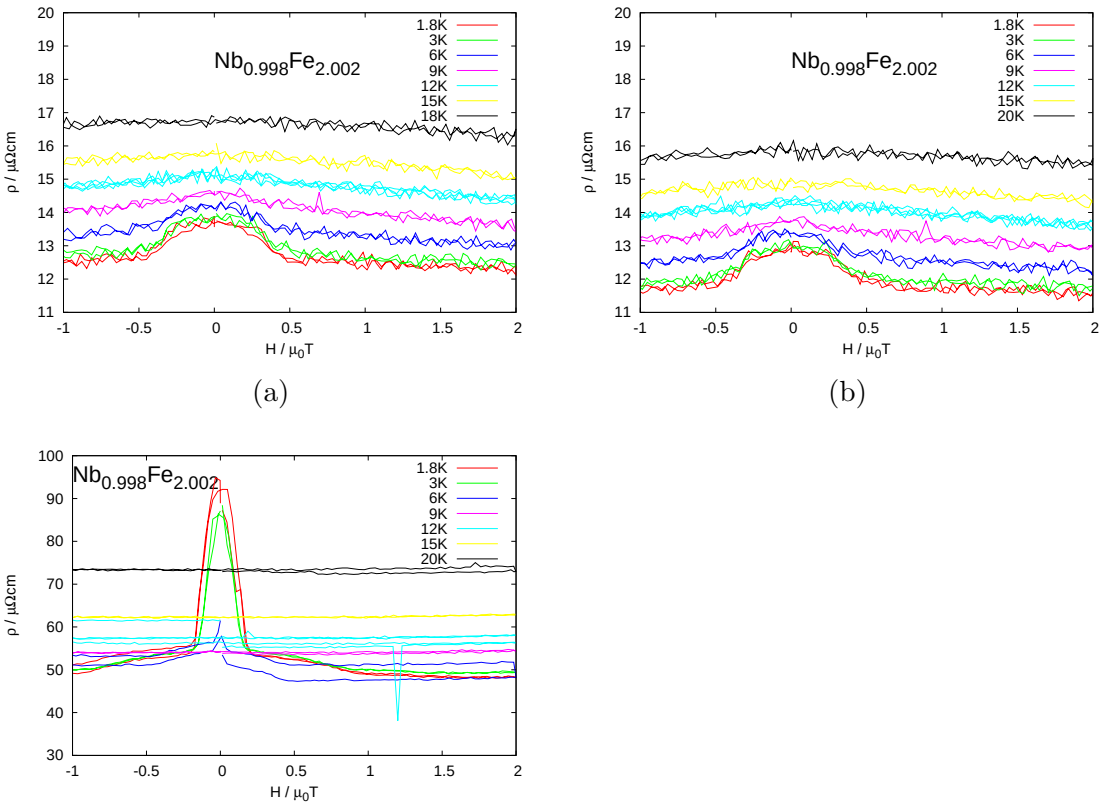

Figure 6.21: Magnetoresistance curves of $Nb_{1-y}Fe_{2+y}$ for y=0.002 measured in a piston cylinder cell with $H//c$ and $J//c$. (a) 1.02 GPa, (b) 1.13 GPa and (c) 1.75 GPa.

is used. The transition temperature was taken as the midpoint of the step. A magnetic phase diagram of the resultant $T_0(H)$ is presented in Figure 6.22. This shows that the modulated phase is being suppressed with increase pressure. To try to determine the critical fields a linear fit has been used for each pressure (fitted over the entire data range). The calculated critical fields are then plotted in Figure 6.23. This shows that the critical pressure is well above the range of the piston cylinder cell and using a straight line fit an estimation of the critical pressure is determined to be 4.2 ± 0.5 GPa.

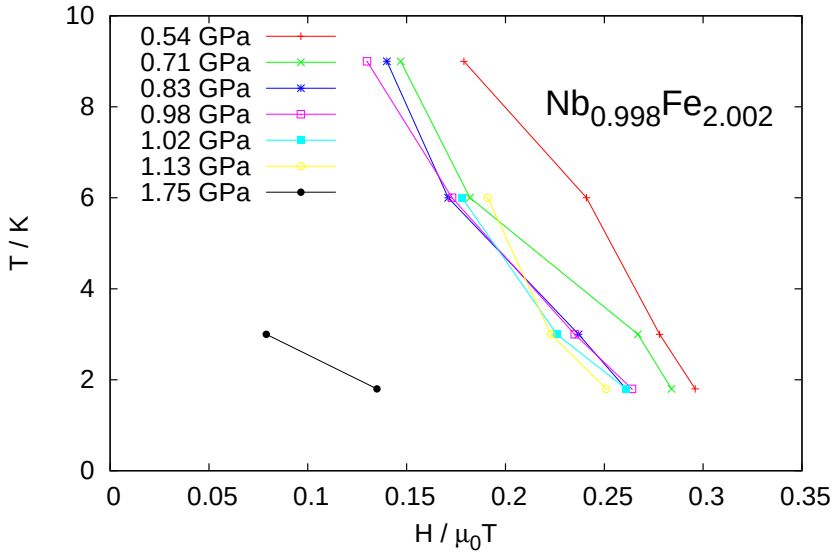

Figure 6.22: Phase diagram for the modulated phase transition temperature as a function of pressure and applied magnetic field of $Nb_{1-y}Fe_{2+y}$ for y=0.002 for $H \perp c$ $J \perp c$.

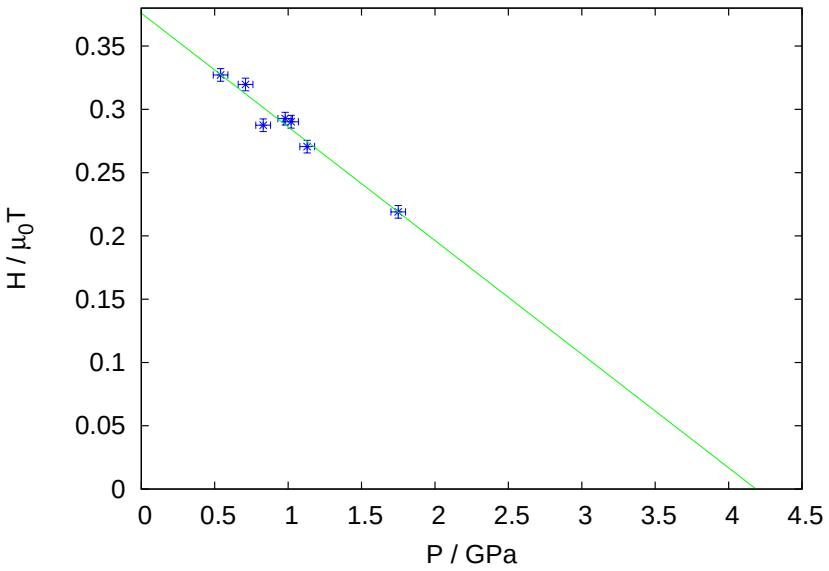

Figure 6.23: Phase diagram for the critical field of the modulated phase transition extrapolated to 0 K as a function of pressure for $Nb_{0.9980}Fe_{2.0020}$ for $H \perp c$ $J \perp c$.

6.6.3 $Nb_{0.9853}Fe_{2.0147}$ (iron rich) , $P = 0$

The magnetoresistance of $Nb_{0.9853}Fe_{2.0147}$ is shown in Figure 6.24 for several temperatures below 50 K. Similar to the results for y=0.002 (Figure 6.19) the magnetoresistance curves show a peak close to zero field, the magnetoresistance dropping off rapidly at low fields and flattens off at higher fields. These are seen as distinct minima in the derivative of the magnetoresistance, $\frac{d\rho}{dH}$, which are shown in Figure 6.25. For $H//c$ the positions of the minima at the different temperatures are similar for both current directions. For $H \perp c$ there are differences however this is due to a crystal misalignment with the $J//c$ case. Therefore only the features in $J \perp c$ data are used in the $H \perp c$ phase diagram (Section 6.7.1).

Temperature sweeps of the resistivity in fixed magnetic fields in both crystallographic orientations are shown in Figure 6.26.

A kink relating to the ferromagnetic transition can be seen in the first two fields for $H \perp C$, 6.26(b). No signal can be seen at 3 T. For data with $H//c$ a peak is difficult to distinguish in any field data. This can be understood recallng that the ferromagnetic ordering in iron rich $NbFe_2$ is of the Ising type ordering in the c direction. It can be assumed that in the high field paramagnetic phase that more of the moments are aligned with the external H field. Therefore there will be a smaller change between the two magnetic phases and therefore a smaller change in the resistivity, reducing the size of the kink. The residual resistivity as a function of field in both orientations is presented in Figure 6.27. This shows that the residual resistivity decreases in both field orientations however an initial more rapid decrease is seen in the $H//c$ case.

6.6.4 $Nb_{0.9853}Fe_{2.0147}$ (iron rich), $P > 0$

Magnetoresistance measurements were taking in a Bridgman anvil cell with orientation $J \perp c$ and with $H//c$. These measurements were only performed at 1.8 K. The results are shown in Figure 6.28(a). Similar to the zero pressure magnetoresistance data a peak is seen at low fields with a sharp drop followed by a more shallow drop. The derivative can again be studied to determine if a minima is seen. This is shown in Figure 6.29. The lowest

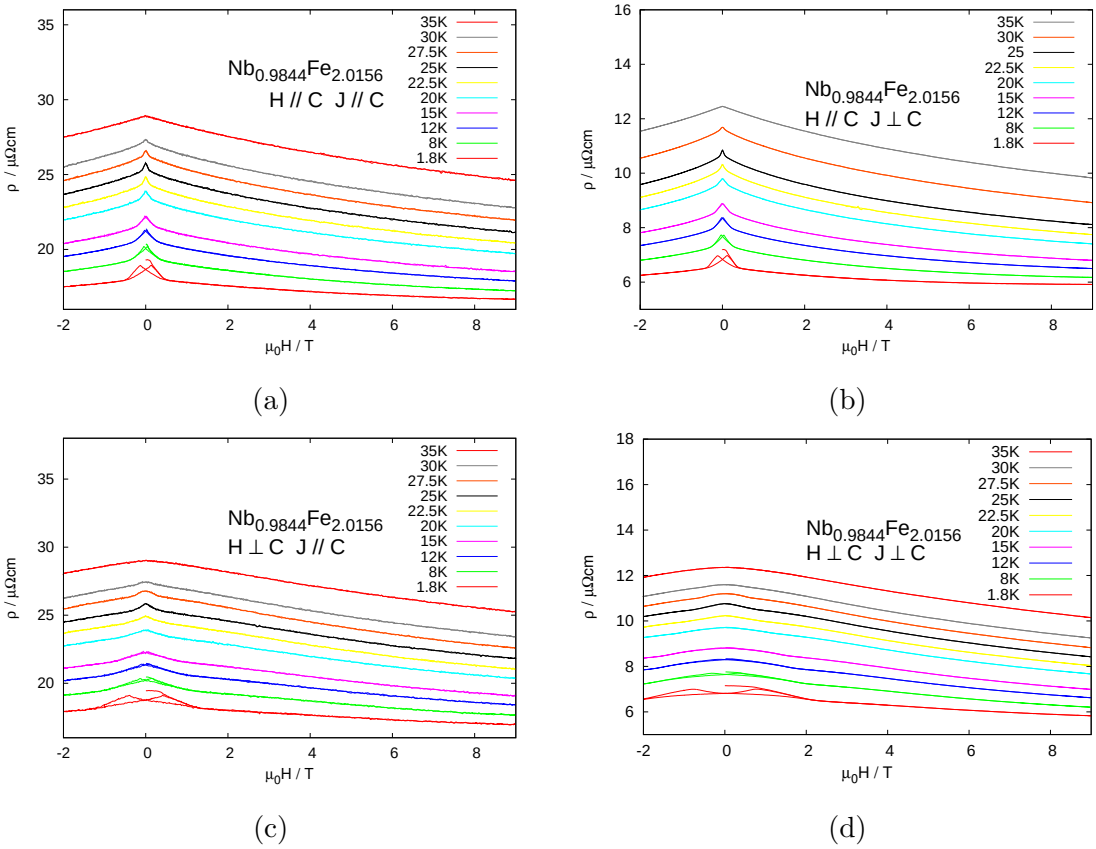

Figure 6.24: Magnetoresistance of y=0.0156 for fixed temperature. (a) $H//c$ $J//c$, (b) $H//c$ $J \perp c$, (c) $H \perp c$ $J//c$, (d) $H \perp c$ $J \perp c$. The onset of the rapid decrease in magnetoresistance is seen to decrease in field with increasing temperature. Hysteresis is seen at 1.8 K for both field orientations.

pressure shows a minimum at 0.19 T. This is similar to the zero pressure results for the magnetoresistance (Figure 6.24) and shows a small decrease between the zero pressure and 1.8 GPa. Beyond the first pressure a clear minimum can not be determined. In looking at the relative change (in magnetoresistance between 0 T and 9 T) between the zero pressure and high pressure data the zero pressure data has a relative change of 12.2% (Figure 6.24) compared to the 4.6% drop of the lowest measured pressure. The reason for this large discrepancy is unknown. Studying the relative change in magnetoresistance between 0 and 9 T as function of pressure shows an interesting feature. Initially the percentage drop increases as pressure increases however above 2.1 GPa the relative change decreases. The

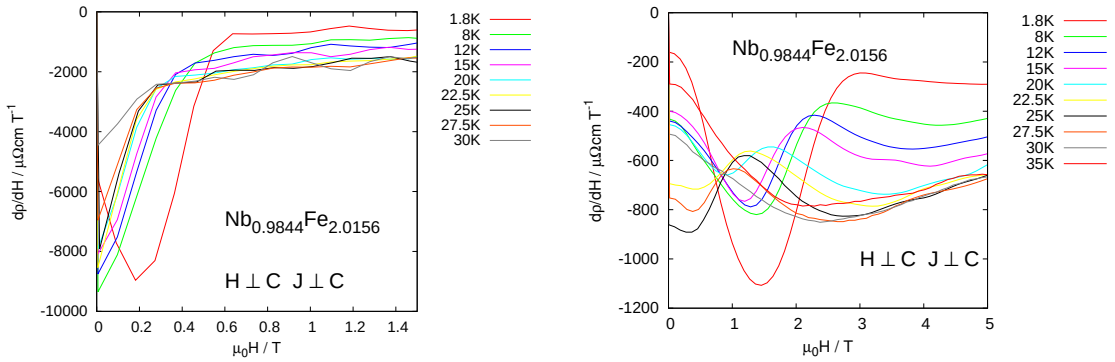

(a) (b)

Figure 6.25: Magnetic field Derivative of the resistivity of $Nb_{1-y}Fe_{2+y}$ for y=0.0156 at various temperatures. (a) shows results for $H//c$ $J//c$. A minima can be determined for 1.8 K. Above this temperature the minima decreases in field but the position of the minima can not be determined. (b) shows results for $H \perp c$ $J \perp c$. This shows a minima at 1.4 T at a temperature of 1.8 K. The minima is seen to decrease in field with increasing temperature and is not seen above 25 K.

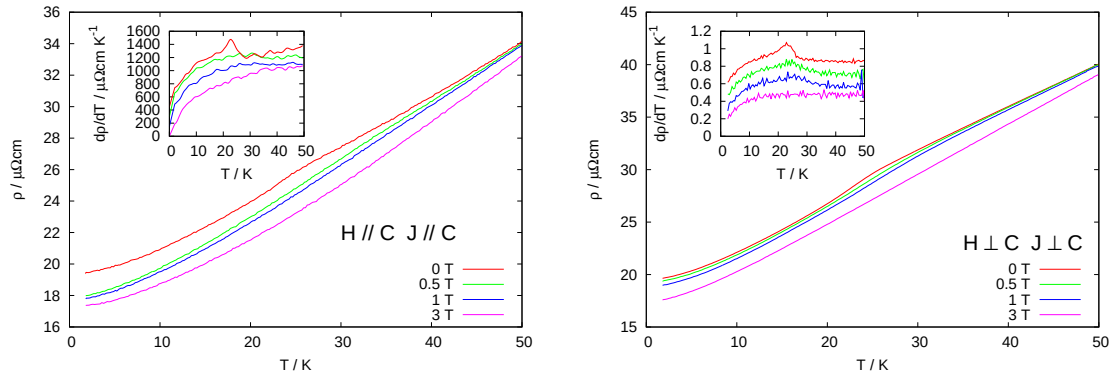

(a) (b)

Figure 6.26: Resistivity as a function of temperature for of $Nb_{1-y}Fe_{2+y}$ for y=0.0156 under fixed magnetic fields. (a) shows $H//c$ $J//c$. (b) shows $H \perp c$ $J \perp c$. The insert in the graph shows the temperature derivative of the data which has been offset for clarity. A step can be seen in the insert of both graphs relating to the ferromagnetic transition. In (b) this can be seen to increase in temperature with increasing field. No step is seen in (a) when a field is applied.

piston cylinder pressure measurements of the polycrystalline sample, P10 [1] are again used for comparison. The data for the polycrystalline magnetoresistance at 1.8 K has been replotted in the same style as in Figure 6.28(a) to allow a direct comparison between

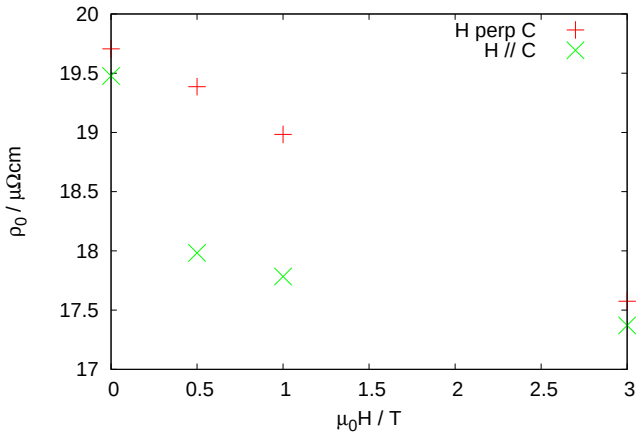

Figure 6.27: The residual resistivity ρ_0 of Figure 6.26 as a function of field for $H \perp c$ $J \perp c$ and $H//c$ $J//c$. Results show a decrease in residual resistivity as the field increases.

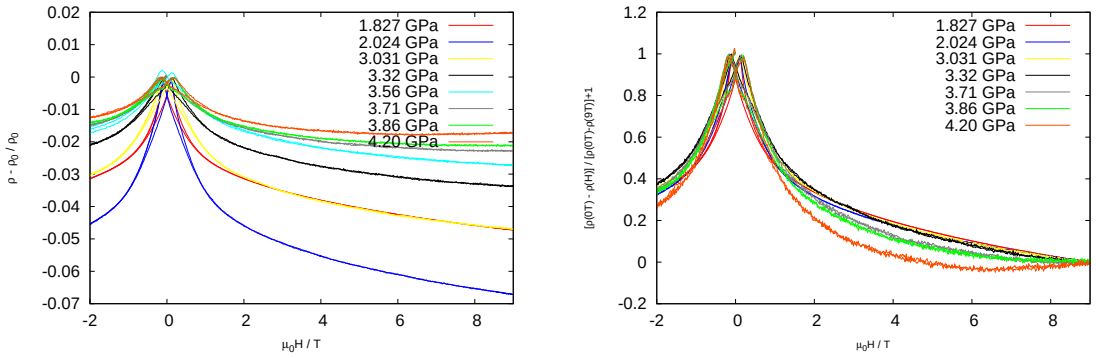

(a) (b)

Figure 6.28: Magnetoresistance at 1.8 K of $Nb_{0.9853}Fe_{2.0147}$ with $H//c$ and $J \perp c$ performed in a Bridgman anvil cell. (a) shows the magnetoresistance normalised to the maximum of the hysteresis. (b) shows $(\rho(0T) - \rho(H)) / (\rho(0T) - \rho(9T)) + 1$. It can be seen from (a) that the difference in resisitivity between 0 T and 9 T first increases with increasing pressure then decreases.

the polycrystal and single crystal data. The results are shown in Figure 6.30 which shows an increasing relative change up to the highest measured pressure, 2.5 GPa. A shoulder can also be seen at higher fields in several of the runs which is related to the critical field of the ferromagnetic transition, H_C in crystallites with $H \perp c$.

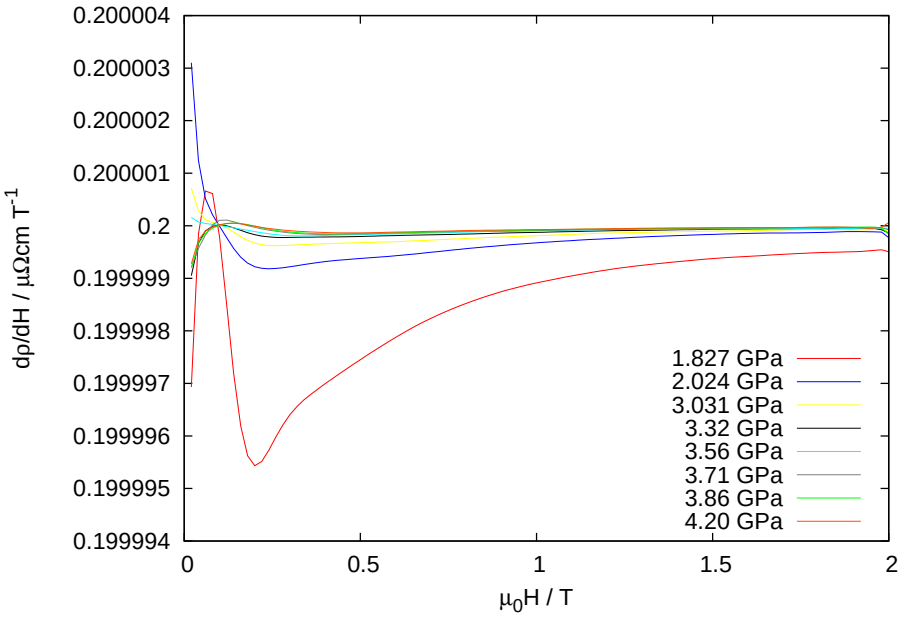

Figure 6.29: The derivative of the magnetoresistance at 1.8 K of $Nb_{0.9853}Fe_{2.0147}$ with $H//c$ and $J \perp c$ for various pressures measured in a Bridgman Anvil cell. A minimum can be seen in the data at 1.8 GPa similar to the zero pressure results 6.25. No further minima are able to be determined.

The relative change between 0 and 9 T from Figures 6.28 and 6.30 are plotted on a single graph for comparison and shown in Figure 6.31. To compare the results together the single crystal data has been scaled around 1.83 GPa using a straight line fit of the polycrystaline data between 1.5-2.5 GPa (the single crystal data is chosen to scale as the results are smaller than expected and the zero pressure and polycrystal results show a similar order of magnitude).

This suggests there is a turning point at around 2.3 ± 0.5 GPa in the change in magnetoresistance between 0 T and 9 T. Further discussion of the significance of this can be found in Section 6.7.1.

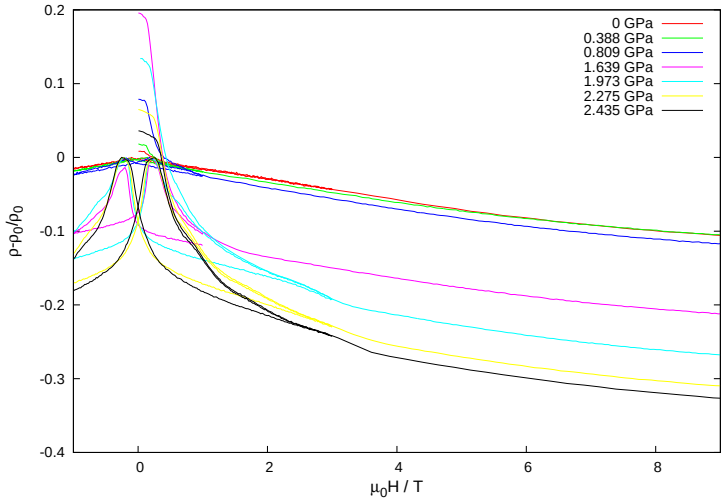

Figure 6.30: Magnetoresistance of polycrystaline at 1.8 K sample P10 for various pressures measured in a piston cylinder cell [82]. The results are normalised to the maximum of the hysteresis. A rapid decrease in magnetoresistance is seen at low fields. The onset of which decreases with applied pressure. A shoulder is also seen at higher pressures relating to the suppression of the ferromagnetic transition.

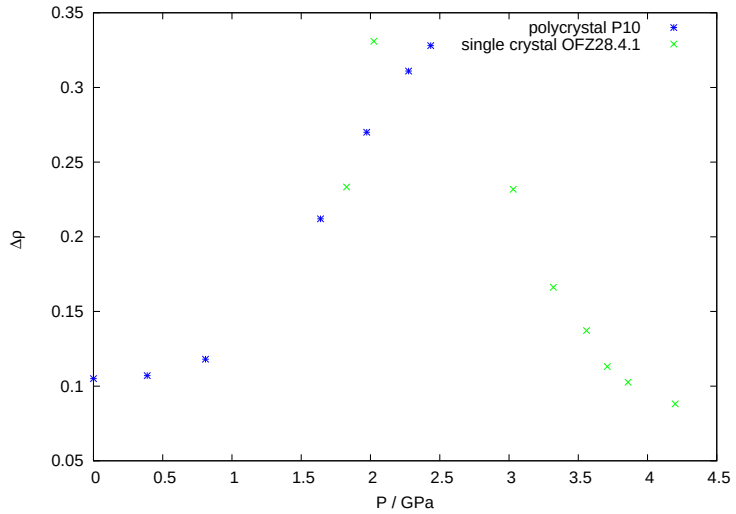

Figure 6.31: The relative change in magnetoresistance between 0 T and 9 T ($\Delta\rho$) as a function of pressure of $Nb_{1-y}Fe_{2+y}$ for y=0.0156 using single crystal, OFZ28.4.1 and polycrystalline, P10 data. The single crystal results have been scaled to the polycrystal results using a straight line fit of the polycrstalline data between 1.5-2.5 GPa. The relative change in magnetoresistance is seen to initially increase with a peak at 2.3 ± 0.5 GPa.

6.7 Discussion

6.7.1 Analysis of Susceptibility and Resistivity Results for $Nb_{0.9853}Fe_{2.0147}$ (iron rich sample)

Using the data presented in the last sections from magnetic susceptibility and resistivity a picture of the magnetic phase diagram of iron rich $NbFe_2$ can be developed. To do this features described in the previous subsections have been collated into a phase diagram, Figure 6.32. Concerning the magnetic susceptibiliy, points are derived from the maxima of the peaks seen in the field sweeps and temperature sweeps (Figures 6.8 and 6.7). The position of shoulders seen the $H \perp c$ field sweeps and a shoulder temperature sweep at 0.1 T are defined by the low field onset. The minima of the derivative of magnetoresistance are also included (6.25). Finally points are included for the position of the kinks seen in the temperature swept resistivity, derived from the maximum of the derivative (6.26).

From the literature the ground state of $Nb_{0.9853}Fe_{2.0147}$ is an Ising ferromagnet however the collation of the data presented offers an alternative interpretation to the phase diagram. Several areas of the phase diagram have been identified. On both sides of the phase diagram the modular transition appears quickly suppressed (purple). This is seen with a simultaneous increase in the ferromagnetic transition temperature. In the ferromagnetic phase a continuation of the modulated phase transition is still observed with a new phase seen at low fields (green) the ground state at zero field. Beyond this transition the Ising ferromagnetic phase is recovered (yellow) in the $H//c$ and $H \perp c$ cases. In the $H \perp c$ the ferromagnetic phase is suppressed at yet higher fields.

Looking more particular at some results, in the $H//c$ data for the temperature dependent magnetic susceptibility (Figure 6.7) a peak at 0.1 T is seen that is four times the magnitude than peaks seen at other fields. This peak appears to exist at the quadruple point between the four phases. Below this field the modulated and ferromagnetic transitions are seen as peaks. Above this field the ferromagnetic transition is seen as a peak and the coexistance phase is seen as a shoulder.

I suggest the potential new phase (green) could manifest as a canting of the ferromag-

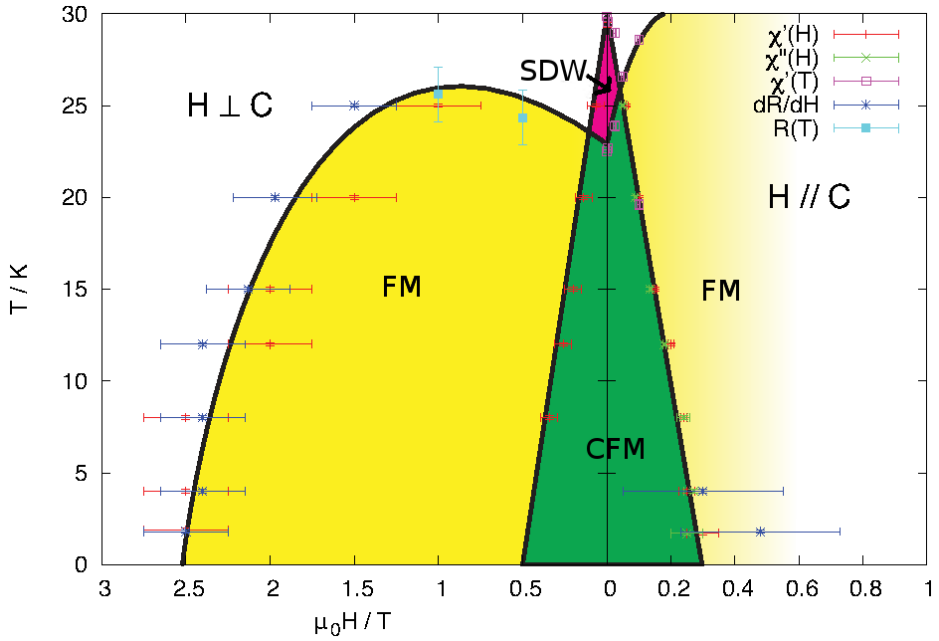

Figure 6.32: A magnetic field dependent phase diagram of $Nb_{0.9853}Fe_{2.0147}$. The legend indicates from which measurements the transition temperatures was derived; either from peaks in the field dependent susceptibility (χ(H)) and the temperature dependent susceptibility (χ(T)), from the minima of the gradients of the magnetoresistance data (dR/dT) (relating to the negative giant magnetoresistance) or, from kinks in the temperature dependent resistivity (R(T)). Guides to the eye have been added and speculative labels added for ease of reference for the ferromagnetic (FM), spin density wave (SDW) and possible canted ferromagnetism (CFM).

netic or ferrimagnetic state (as discussed at the start of this chapter the ferromagnetic phase has been seen to be ferrimagnetic in a 2.5 T field with $H//c$).

The interpretation of the suppression of the modulated phase in the $H//c$ case agrees with previous work [1], which is partially derived from the minima in the derivative of the magnetoresistance. Previous emphasis was placed on the similarity of the minima seen in both field directions of the magnetoresistance results. In our alternative interpretation stronger emphasis has been placed on the similar features seen in the magnetic susceptibility which is a more intrinsic measure for studying magnetic transitions. This means that the $H \perp c$ shows a similar transition which was labeled as the modulated to paramagnetic transition in previous studies and in the new interpretation has been labeled as

the ferromagnetic (ferrimagnetic) to paramagnetic transition.

A Pressure to Chemical Composition Comparison

The phase diagram obtained for the ferromagnetic transition as a function of pressure (Figure 6.18) may be compared to the previous results obtained for the chemical composition phase diagram. The resulting phase diagram, which has the pressure axis reversed to allow comparison to the published stoichiometric phase diagram [47] is shown in Figure 6.33. The combined single crystal and polycrystal measurement for $y = 0.0157 \pm 0.0001$ is plotted on the lower axis while the stoichiometric data is plotted on the upper axis. The data seems to show good agreement between the phase diagrams obtained via pressure and chemical tuning. A doping to pressure ratio may be obtained measured is $(0.01/42.0) = (2.4 \pm 0.3) \times 10^{-3}$ GPa^{-1}. Due to the good agreement between the chemical composition and pressure phase diagram it can be assumed that the electronic disorder introduced by chemically doping of $NbFe_2$ is a small contribution to the magnetic ordering. Two possible regions of the ferromagnetic transition can be been with the change between the two seen around 2 GPa. Above 2 GPa this is characterised with a linear suppression of the transition temperature with increasing pressure/Nb%. Fitting a straight line a critical pressure for the suppression of the ferromagnetic transition is determined to be 6.7 GPa. This value relates to a doping of $y = 0$ which agrees well with results from the chemical composition phase diagram [47].

6.7.2 Power Law Dependence of the resistivity results of of $Nb_{1-y}Fe_{2+y}$ for y=0.0156 (iron rich)

A power law may be fitted to the resistivity data as discussed in subsection 3.2.1. The power law dependence for zero pressure has been previously shown to have non-Fermi liquid behaviour over all temperature ranges below 50 K for both $J \perp c$ and $J//c$ [1]. A $T^{3/2}$ power law relation below T_C is found. Below 5 K a trend is seen towards higher power laws, close to T^2 or $T^{5/3}$ suggesting either a return to Fermi liquid behaviour or 3D ferromagnetic fluctuations. Based on previous measurements by Moroni et. al. [47]

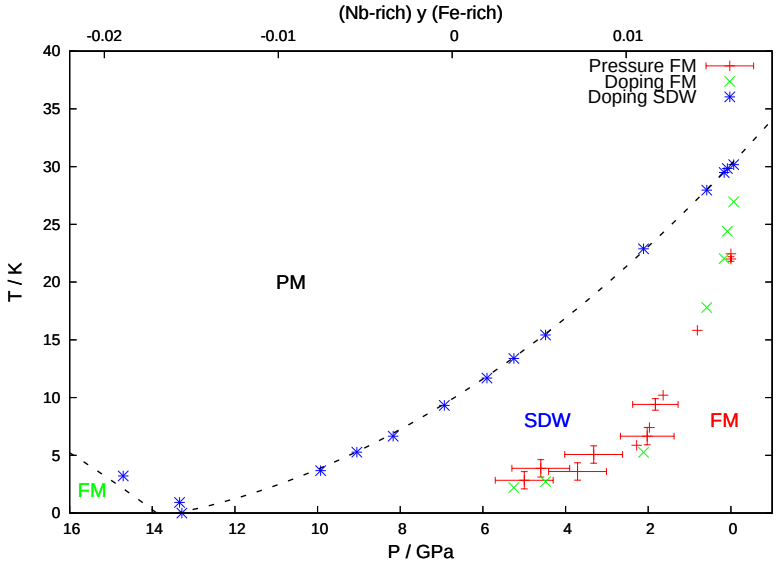

Figure 6.33: Pressure phase diagram (lower axis) compared to chemical composition phase diagram (upper axis) of $Nb_{1-y}Fe_{2+y}$. Legend indicates if data is derived from chemically doped $NbFe_2$ [47] or from pressure measurements [1]. Labels indicate ferromagnetic phase (FM) and modulated phase (SDW). Results show good agreement between pressure and doping phase diagram. A doping pressure ratio can be derived of $(2.4 \pm 0.3) \times 10^{-3}$ (Nb%)GPa^{-1}

where Fermi Liquid behaviour is seen at the lowest temperatures, T^2 seems the most likely possibility. At T_C a jump in the power law is seen and the onset of a large peak in the effective scattering cross section above which the temperature dependence is linear for the $J \perp c$ case and $n = 1.1 \pm 0.1$ for the $J//c$ orientation. To look at the trend of the power law dependence of the data obtained from the pressure measurements several temperature regions were studied. Presented below are the power laws obtained from fits over a region of 2 K to 5 K.

To test the validity of this fit over the region of 2 K to 5 K plots of difference between the resistivity and the power law obtained T^n are shown in Figures 6.34 with representative plots from several pressure regions. In all pressures below 5 K the difference in fit and data is less than 0.005 $\mu\Omega$cm for the choice of ρ_0. The power laws determined from this method are presented as a function of pressure in Figure 6.35. The error from this plot is determined from the error in ρ_0 as this was the largest contribution to the error (ρ_0 was

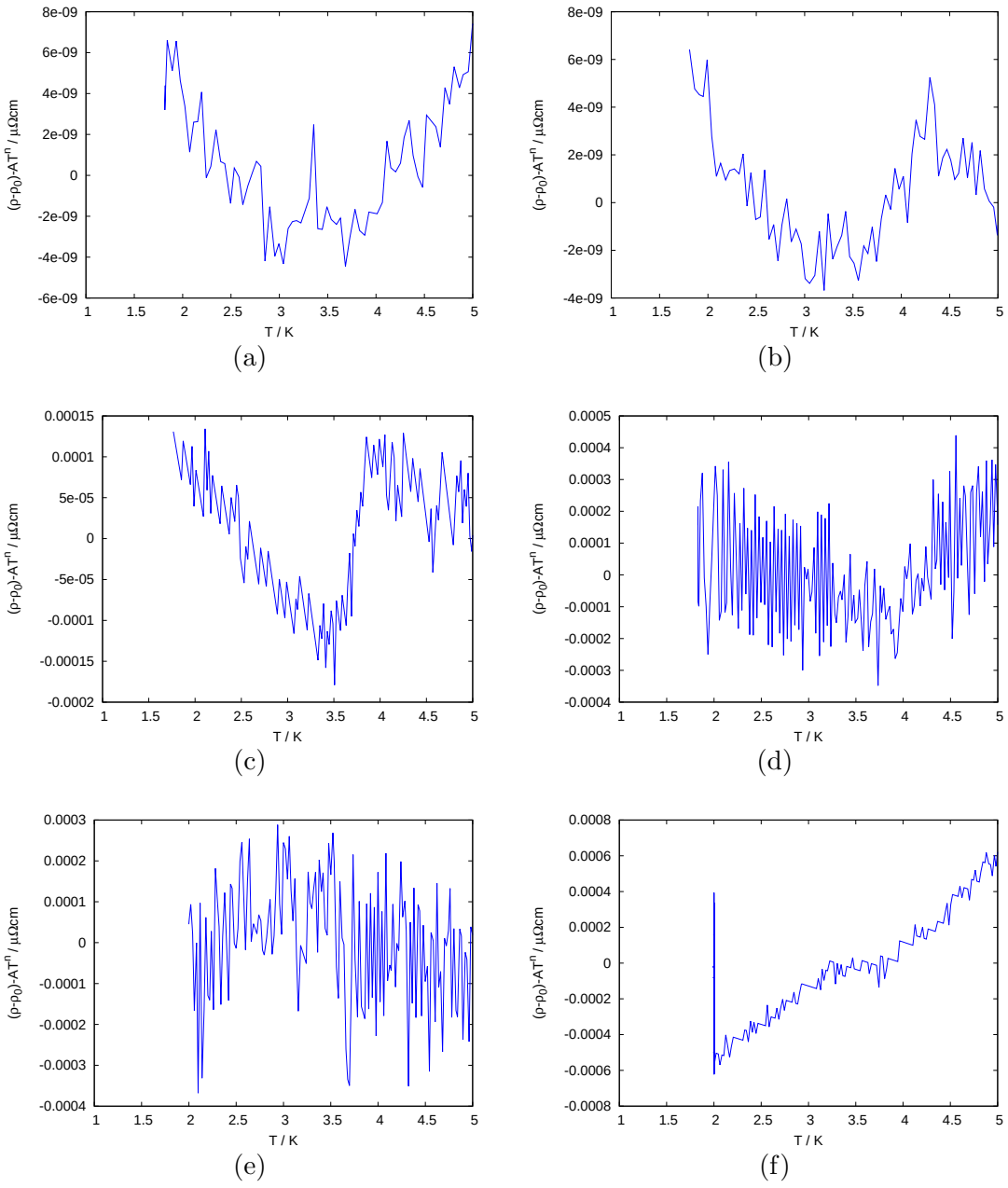

Figure 6.34: Difference between resistivity for various pressures of y=0.0156 (taken in a Bridgman anvil cell) and the fitted power law T^n taken between 2-5 K. (a)2.02 GPa, (b)3.71 GPa, (c) 4.60 GPa, (d) 5.53 GPa, (e) 12.05 GPa, and (f) 15.21 GPa

determined using a least square fit of the low temperature data). The power law results

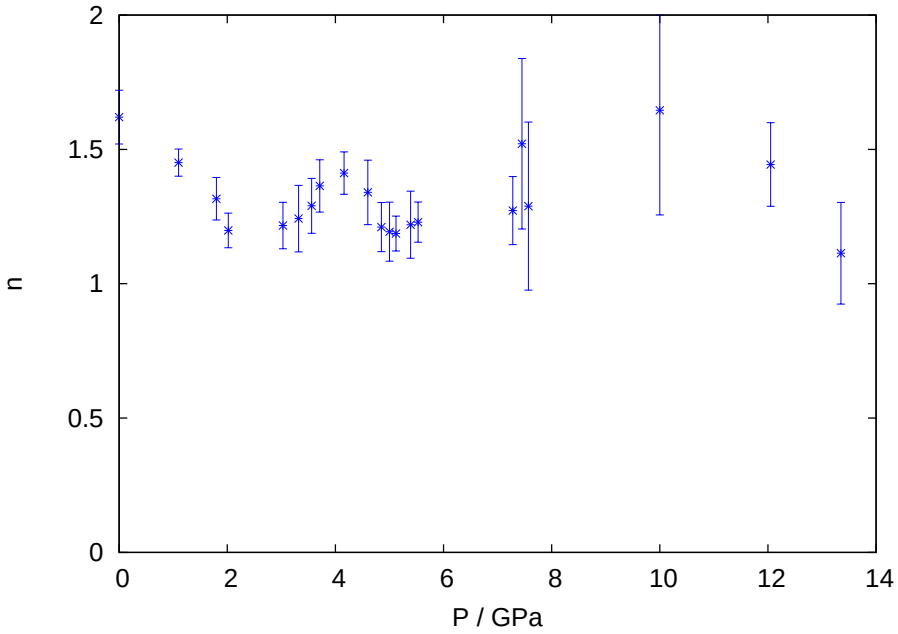

Figure 6.35: Power law dependence of the resistivity under pressure of y=0.0156. Fitting performed between 2-5 K.A general power law between 1-1.7 is seen over all pressure, showing non-Fermi liquid behaviour.

show that non-Fermi liquid behaviour is observed at all pressures measured. Between 2 ± 0.5 GPa and 6 ± 1 GPa a general power law of $T^{1.35}$ is seen. Below 2 ± 0.5 GPa an increase in the power law dependence is seen. Above 6 ± 1 GPa the noise at low temperature mean the error in the power law is larger. Therefore no trend can be determined.

6.7.3 Power Law Analyses of of $Nb_{1-y}Fe_{2+y}$ for y=0.002 (near stoichimetry)

Data on stoichiometric $Nb_{0.9980}Fe_{2.0020}$ has been analysed in a similar fashion. The same fitting region of 2-5 K is used as in the analysis of y=0.0156. The results are shown in Figure 6.7.3 with the difference between the resistivity data and the determined power law shown in Figure 6.36. The results show non-Fermi liquid behavior is seen over the entire pressure region measured with $T^{1.8}$.

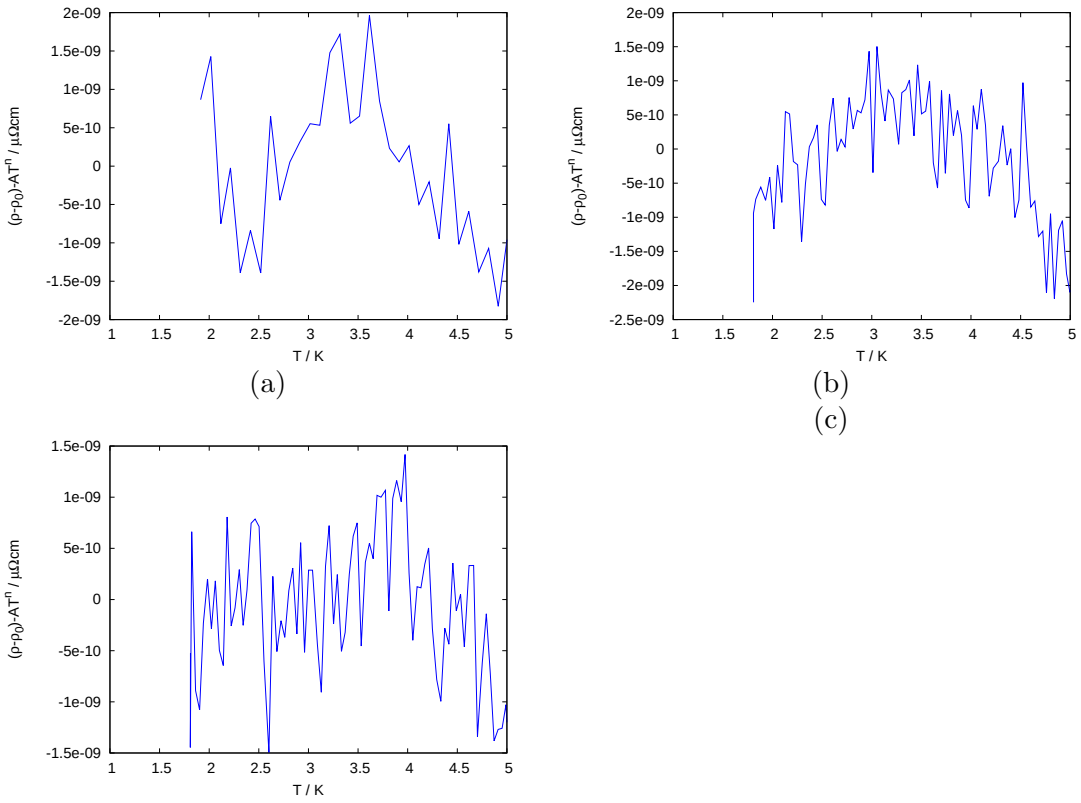

Figure 6.36: Difference between resistivity for various pressures of y=0.002 (taken in a piston cylinder cell) and the fitted power law T^n taken between 2-5 K. (a)0.54 GPa, (b)0.71 GPa and (c) 0.98 GPa

6.7.4 Comparison of of $Nb_{1-y}Fe_{2+y}$ $y = 0.002$ (near stoichimetry) and $y0.0156$ (iron rich)

Comparison can now be made between the two sampes with different stoichiometries measured using the pressure to chemical composition ratio determined from the ferromagnetic suppression of y=0.0156 (subsection 6.7.1). Therefore presented in Figure 6.7.4 are the results from Figure 6.35 for y=0.0156 with the results from y=0.002, Figure 6.7.3 offset by 6.72 GPa. No real comparison can be made between the regions overlapping between the two stoichiometries as the error is so large in the y=0.0156 run at high pressures. the increase in n of approximately 0.5 between the low pressure 0.0156 results and the

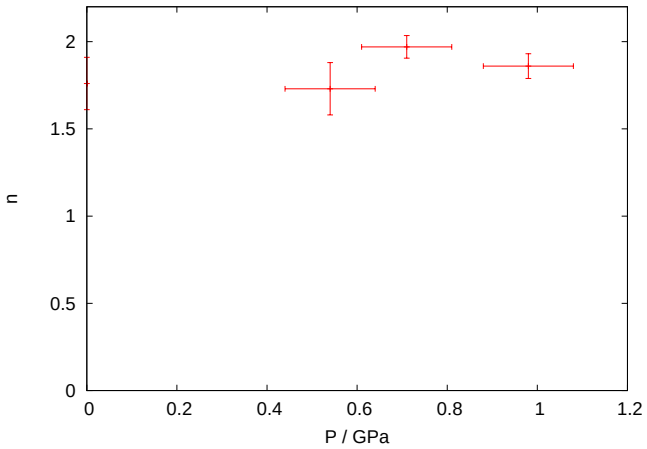

Figure 6.37: The resistivity power law dependence under pressure of $Nb_{0.9980}Fe_{2.0020}$.

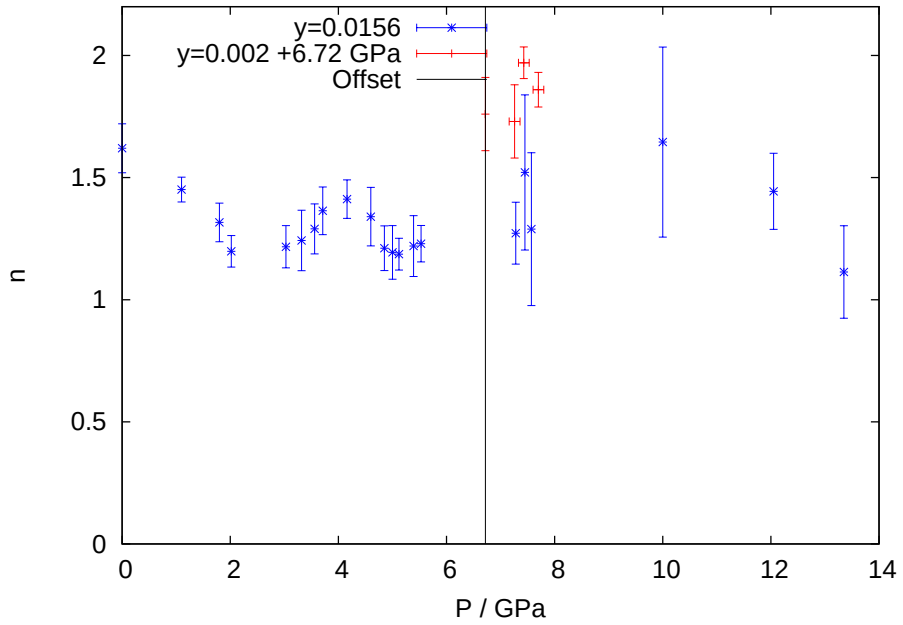

Figure 6.38: Power law comparison of stoichiometric and iron rich $NbFe_2$ using pressure doping relation determined in Subsection 6.7.1

results from y=0.002 suggest there is an increase in n around the ferromagnetic quantum phase transition. The high pressure y=0.0156 results seem to suggest a trend towards a decreasing n as the modulated quantum phase transition. Over the entire pressure region

measured both samples show non-Fermi liquid like power laws.

6.8 Conclusion

Results from y=0.0156 sample showed that the ground state of iron rich $NbFe_2$ may not be a simple Ising ferromagnet but instead could be a co-existance state between the Ising Ferromagetic state (seen under applied magnetic field) and the modulated state. This could manifest as a canting of the ferromagnetic state. Results from y=0.0156 under hydrostatic pressure shows that the (canted) ferromagnetic ground state is suppressed below 2 K by 5 GPa and the rate of suppression is in good agreement with previous pressure measurements of polycrystalline samples [1]. Comparison was also made with previous chemical doping measurements of the phase diagram. Good agreement was found between the pressure phase diagram and the chemical doping phase diagram for the ferromagnetic state. No comparison was made of the modulated phase. This suggests that the main contribution to the suppression of the ferromagnetic state in the chemical doping phase diagram is changes in lattice parameter. A relation between the pressure and Nb concentration was determined to be $(2.4 \pm 0.1) \times 10^{-3}$ (Nb%)GPa^{-1}. Measurements for of $Nb_{1-y}Fe_{2+y}$ y=0.002 under pressure have shown that the modulated phase is suppressed with increasing pressure. A phase diagram of the critical fields for the modulated phase as a function of pressure was used to determine an estimate for the critical pressure of the modulated phase. This was determined to be 4.2 ± 0.2 GPa.

Chapter 7

Conclusions and outlook

I this thesis measurements on itinerant d-elctron antiferromagnets ($FePt_3$ and Mo_3Sb_7) and ferromagnets (of $Nb_{1-y}Fe_{2+y}$) have been presented. The general ain of these studies was to pressure tume these systems towards magnetic quantum phase transitions and to explore the physics associated with the quantum phase transitions.

7.1 $FePt_3$

$FePt_3$ is a rare example of a transition metal 3D antiferromagnet with a second order phase transition. The resistivity measurements in a Bridgman anvil cell have resulted in the pressure temperature phase diagram shown in Figure 7.1 The paramagnetic to antiferromagnetic transition, T_N was seen to increase by 35 ± 5 K over 15 GPa. The antiferromagnetic to antiferromagnetic phase transition shows a decrease of 15 ± 5 K over 7 GPa and remains relatively linear above this. Therefore $FePt_3$ has shown a surprisingly weak pressure dependence and the quantum phase transition can not be reached using a Bridgman anvil cell. Analysis of the power law dependence of the low temperature resistivity has shown $n > 2$ in all measurements. This suggests that the electron-electron scattering contribution is weak over the whole pressure range studied.

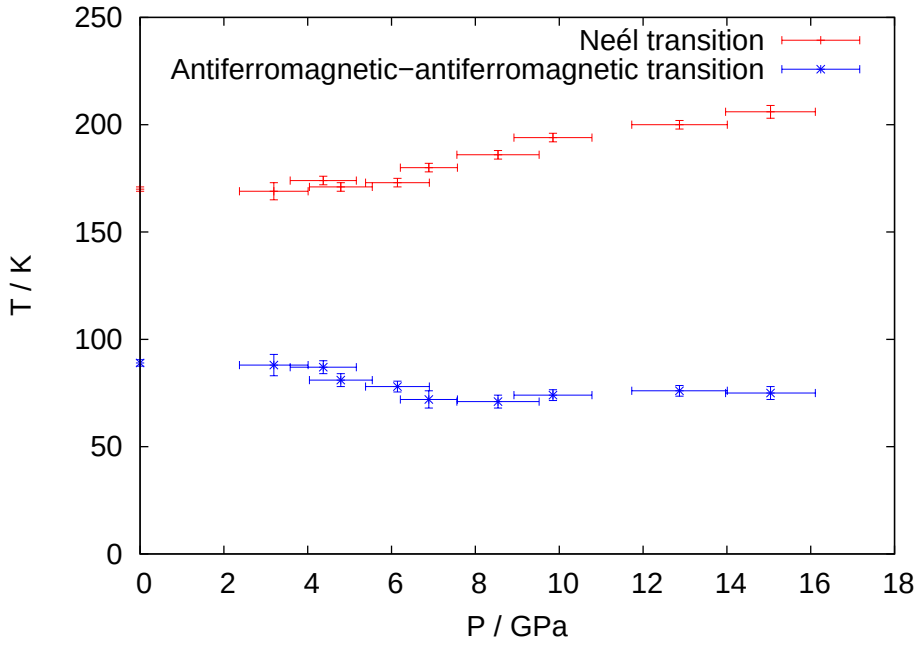

Figure 7.1: Phase diagram of the magnetic transitions of $FePt_3$ as a function of pressure. The Neél transition, T_N shows an increase from 170 K to 205 K. The antiferromagnetic-antiferromagnetic , T_S shows a initial decrease up to 7 GPa and is linear after.

7.2 Mo_3Sb_7

The second candidate system for studying the border of antiferromagnetism at low temperature was Mo_3Sb_7 , which is a superconducting amtiferromagnet at low pressure. Results were obtained using a new technique for measuring magnetic susceptibility in a Bridgman anvil cell which involved the placement of counterwound pick-up and compensation coils in the pressurised region. With this method the phase diagram, which was previously studied up to 2.2 GPa [81] has been extended to 9 GPa. The extended phase diagram is displayed in Figure 7.2 and shows good agreement with previous results at the overlapping low pressures. The extended high pressure results show that the superconducting transition temperature, T_c continues to increase, changing by 1.1 ± 0.2 K over 8.5 GPa in the pressure direction in which the spin density wave is expected to decrease. This matches scenarios [99] for magnetically induced superconductivity, however, the spin density wave

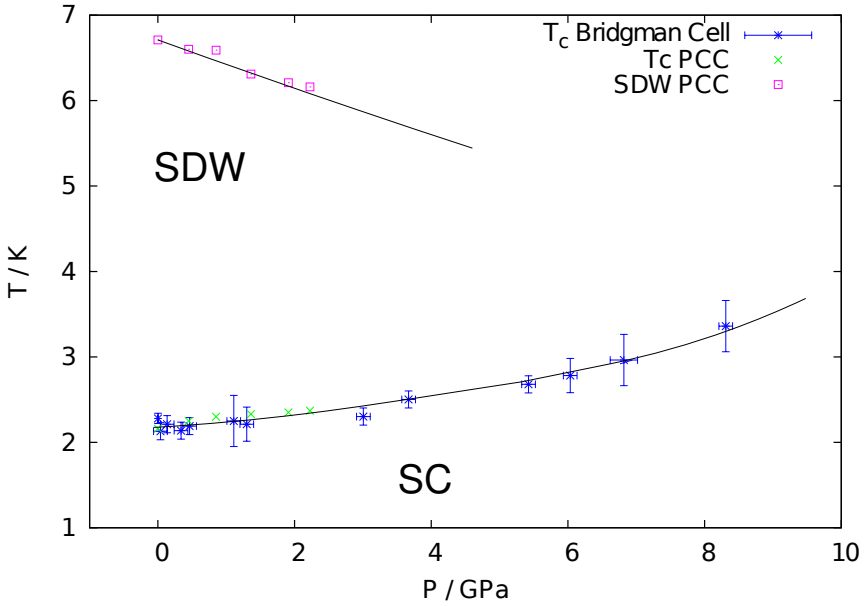

Figure 7.2: Extended pressure-temperature phase diagram of Mo_3Sb_7 showing the pressure dependence of the superconducting and SDW transitions. The susceptibility measurements in a Bridgman anvil cell were performed by the author and compared to the results from resistivity and magnetisation in a piston cylinder cell (PCC) were by V.H. Tran et.al. [81]

transition temperature could not be determined at high pressure.

7.3 $Nb_{1-y}Fe_{2+y}$

IN of $Nb_{1-y}Fe_{2+y}$ the physics at the border of ferromagnetism have been investigated. From composition tuning and pressure tuning of polycrystals it seemed possibble that of $Nb_{1-y}Fe_{2+y}$ is the first case where a ferromagnetic quantum phase transition is masked by an emerging phase of modulated magnetic order. An extension on recently begun studies on single crystals has been presented here.

Two recently grown single crystals were measured at zero pressure and at high pressures. From measurements of the physical properties of an iron rich sample of $NbFe_2$ a field-temperature phase diagram was built up for both $H//c$ and $H \perp c$. The phase diagram shows that a feature, which indicate from the transition between the modulated

phase to paramagnetic phase at higher temperature are seen to extend to the ferromagnetic phase at lower temperature. This is shown in Figure 7.3(a) and suggests a canting of the ferromagnetic state at low field. Further studies of this region are needed to better understand the ground state in the iron rich side of the $NbFe_2$ phase diagram.

Under pressure a phase diagram of the low field ferromagnetic state was developed. The resulting phase diagram has been compared to the chemical composition phase diagram. This is shown in Figure 7.3(b) with the pressure axis reversed along the lower axis and the chemical doping along the top axis. This showed good agreement between the temperature-pressure phase diagram and the temperature-doping phase diagram and a ratio between doping and pressure was determined to be $(2.4 \pm 0.1) \times 10^{-3}$ GPa^{-1}. A fit was taken and a critical pressure for the low field ferromagnetic state was determined to be 6.7 ± 0.2 GPa which relates to a composition near stoichiometry which is in agreement with the literature [47].

Results from the magnetoresistance of $Nb_{0.9980}Fe_{2.0020}$ have shown the evolution of the modulated phase in field and pressure. Using a linear fit the critical field for each pressure was determined. These showed a linear decrease in the critical field with increasing pressure. Extrapolating a critical pressure for the modulated phase was determined 4.2 ± 0.5 GPa. This in reasonable agreement with the compositional value expected, which would be 5.4 ± 0.1 GPa.

Power law analysis for both the iron rich and stoichiometric samples showed non-Fermi liquid behavior over all pressures measured. The low pressure power law for $Nb_{0.9853}Fe_{2.0147}$ shows a decrease from 1.6 ± 0.1 to 1.3 ± 0.1 up to 2.0 ± 0.5 GPa. An exponent of $n = 1.35 \pm 0.1$ seen between 2.0 ± 0.5 GPa and 6 ± 1 GPa. Beyond this pressure the noise increases such that no trend is seen however the exponent remains between 1.2 and 1.7. For $Nb_{0.9980}Fe_{2.0020}$ a power law of 1.8 ± 0.1 is seen over the pressure region. This is in good agreement with the literature which sees non-Fermi liquid exponents of $n = 1.5 - 1.7$ from $y = -0.015 - 0.02$ [1].

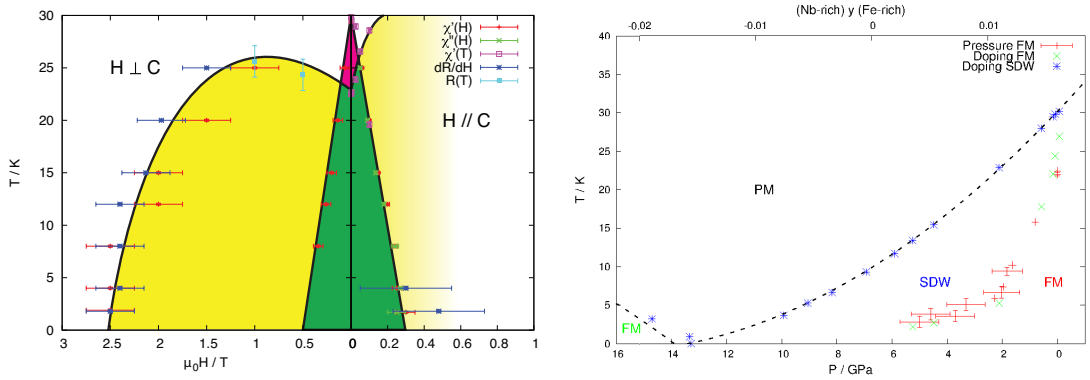

(a) (b)

Figure 7.3: Key results for $NbFe_2$.(a)Temperature-Field phase diagram of iron rich $NbFe_2$ (b)Temperature-Pressure phase diagram (lower axis) compared to chemical composition phase diagram (upper axis) of $NbFe_2$.

Bibliography

[1] W. J. Duncan, *Quantum Phase Transitions in $NbFe_2$ and Ba_2As_2*. PhD thesis, Royal Holloway, University of London, 2010.

[2] A. J. Schofield, "Quantum criticality and novel phases: Summary and outlook," *Physica Status Solidi B-basic Solid State Physics*, vol. 247, pp. 563–569, 2010.

[3] S. Sachdev, "Quantum magnetism and criticality," *Nat Phys*, vol. 4, pp. 173–185, Mar. 2008.

[4] O. Trovarelli, C. Geibel, S. Mederle, C. Langhammer, F. M. Grosche, P. Gegenwart, M. Lang, G. Sparn, and F. Steglich, "$YbRh_2Si_2$: Pronounced non-fermi-liquid effects above a low-lying magnetic phase transition," *Phys. Rev. Lett.*, vol. 85, pp. 626–629, Jul 2000.

[5] H. v. Löhneysen, T. Pietrus, G. Portisch, H. G. Schlager, A. Schröder, M. Sieck, and T. Trappmann, "Non-fermi-liquid behavior in a heavy-fermion alloy at a magnetic instability," *Phys. Rev. Lett.*, vol. 72, pp. 3262–3265, May 1994.

[6] M. C. Aronson, R. Osborn, R. A. Robinson, J. W. Lynn, R. Chau, C. L. Seaman, and M. B. Maple, "Non-Fermi-liquid scaling of the magnetic response in $UCu_{5-x}Pd_x$ ($x = 1, 1.5$)," *Phys. Rev. Lett.*, vol. 75, pp. 725–728, Jul 1995.

[7] N. D. Mathur, F. M. Grosche, S. R. Julian, I. R. Walker, D. M. Freye, R. K. W. Haselwimmer, and G. G. Lonzarich, "Magnetically mediated superconductivity in heavy fermion compounds," *Nature*, vol. 394, pp. 39–43, July 1998.

[8] S. A. Grigera, R. S. Perry, A. J. Schofield, M. Chiao, S. R. Julian, G. G. Lonzarich, S. I. Ikeda, Y. Maeno, A. J. Millis, and A. P. Mackenzie, "Magnetic field-tuned quantum criticality in the metallic ruthenate $Sr_3Ru_2O_7$," *Science*, vol. 294, no. 5541, pp. 329–332, 2001.

[9] L. Landau *Soviet Physics - Journal of Experimental and Theoretical Physics*, vol. 3, p. 920, 1957.

[10] G. R. Stewart, "Non-fermi-liquid behavior in *d*- and *f*-electron metals," *Rev. Mod. Phys.*, vol. 73, pp. 797–855, Oct 2001.

[11] R. P. Smith, M. Sutherland, G. G. Lonzarich, S. S. Saxena, N. Kimura, S. Takashima, M. Nohara, and H. Takagi, "Marginal breakdown of the fermi-liquid state on the border of metallic ferromagnetism," *Nature*, vol. 455, pp. 1220–1223, Oct. 2008.

[12] S. Lefebvre, P. Wzietek, S. Brown, C. Bourbonnais, D. Jrome, C. Mzire, M. Fourmigu, and P. Batail, "Mott transition, antiferromagnetism, and unconventional superconductivity in layered organic superconductors," *Phys. Rev. Lett.*, vol. 85, pp. 5420–5423, Dec. 2000.

[13] Y. Takabayashi, A. Y. Ganin, P. Jegli, D. Aron, T. Takano, Y. Iwasa, Y. Ohishi, M. Takata, N. Takeshita, K. Prassides, and M. J. Rosseinsky, "The disorder-free non-BCS superconductor Cs_3C_{60} emerges from an antiferromagnetic insulator parent state," *Science*, vol. 323, no. 5921, pp. 1585–1590, 2009.

[14] Y. Kamihara, T. Watanabe, M. Hirano, and H. Hosono, "Iron-based layered superconductor La[$O_{1-x}F_x$]FeAs (x=0.05-0.12) with T_c=26 k," *Journal of the American Chemical Society*, vol. 130, pp. 3296–+, Mar. 2008.

[15] M.-H. Fang, H.-D. Wang, C.-H. Dong, Z.-J. Li, C.-M. Feng, J. Chen, and H. Q. Yuan, "Fe-based superconductivity with T_c =31 K bordering an antiferromagnetic insulator in (Tl,K)Fe_xSe_2," *EPL (Europhysics Letters)*, vol. 94, no. 2, p. 27009, 2011.

[16] P. Gegenwart, Q. Si, and F. Steglich, "Quantum criticality in heavy-fermion metals," *Nat Phys*, vol. 4, pp. 186–197, Mar. 2008.

[17] A. Schroder, "Onset of antiferromagnetism in heavy-fermion metals," *Nature*, vol. 407, pp. 351–355, 2000.

[18] J. Custers, "The break-up of heavy electrons at a quantum critical point," *Nature*, vol. 424, pp. 524–527, 2003.

[19] H. Kotegawa, A. Harada, S. Kawasaki, Y. Kawasaki, Y. Kitaoka, Y. Haga, E. Yamamoto, Y. Ōnuki, K. M. Itoh, E. E. Haller, and H. Harima, "Evidence for uniform coexistence of ferromagnetism and unconventional superconductivity in UGe_2: A ^{73}Ge-NQR study under pressure," *Journal of the Physical Society of Japan*, vol. 74, no. 2, pp. 705–711, 2005.

[20] D. Aoki, A. Huxley, E. Ressouche, D. Braithwaite, J. Flouquet, J.-P. Brison, E. Lhotel, and C. Paulsen, "Coexistence of superconductivity and ferromagnetism in URhGe," *Nature*, vol. 413, pp. 613–616, Oct. 2001.

[21] T. Akazawa, H. Hidaka, H. Kotegawa, T. C. Kobayashi, T. Fujiwara, E. Yamamoto, Y. Haga, R. Settai, and Y. Ōnuki, "Pressure-induced superconductivity in UIr," *Journal of the Physical Society of Japan*, vol. 73, no. 11, pp. 3129–3134, 2004.

[22] K. Shimizu, T. Kimura, S. Furomoto, K. Takeda, K. Kontani, Y. Onuki, and K. Amaya, "Superconductivity in the non-magnetic state of iron under pressure," *Nature*, vol. 412, pp. 316–318, July 2001.

[23] V. H. Tran, R. T. Khan, P. Winiewski, and E. Bauer, "Pressure studies on the superconductor Mo_3Sb_7," *Journal of Physics: Conference Series*, vol. 273, no. 1, p. 012088, 2011.

[24] M. Brando, W. J. Duncan, D. Moroni-Klementowicz, C. Albrecht, D. Grüner, R. Ballou, and F. M. Grosche, "Logarithmic fermi-liquid breakdown in $NbFe_2$," *Phys. Rev. Lett.*, vol. 101, p. 026401, Jul 2008.

[25] M. Gutzwiller, "Correlation of electrons in a narrow band," *Phys. Rev.*, vol. 137, pp. 1726–1735, 1965.

[26] P. Fazckas, *Electron Correlation and Magnetism.* World Scientific, 1999.

[27] J. Hertz, "Quantum critical phenomena," *Phys. Rev. B*, vol. 14, pp. 1165–1184, 1976.

[28] A. J. Millis, "Effect of a nonzero temperature on quantum critical points in itinerant fermion systems," *Phys. Rev. B*, vol. 48, pp. 7183–7196, Sep 1993.

[29] T. Moriya, *Spin fluctuations in itinerant electron magnetism.* Springer-Verlag, Berlin, 1985.

[30] G. Lonzarich, "The magnetic equation of state and heat capacity in weak itinerant ferromagnets," *Journal of Magnetism and Magnetic Materials*, vol. 5457, Part 2, pp. 612–616, Feb. 1986.

[31] S. L. Sondhi, S. M. Girvin, J. P. Carini, and D. Shahar, "Continuous quantum phase transitions," *Rev. Mod. Phys.*, vol. 69, pp. 315–333, Jan. 1997.

[32] G. Lonzarich, *Electron; a centenary volume.* Cambridge University Press, 1997.

[33] P. G. Niklowitz, F. Beckers, G. G. Lonzarich, G. Knebel, B. Salce, J. Thomasson, N. Bernhoeft, D. Braithwaite, and J. Flouquet, "Spin-fluctuation-dominated electrical transport of Ni_3Al at high pressure," *Phys. Rev. B*, vol. 72, p. 024424, Jul 2005.

[34] M. Uhlarz, C. Pfleiderer, and S. Hayden, "Quantum phase transitions in the itinerant ferromagnet," *Physica B: Condensed Matter*, vol. 359361, pp. 1174–1176, Apr. 2005.

[35] S. S. Saxena, P. Agarwal, K. Ahilan, F. M. Grosche, R. K. W. Haselwimmer, M. J. Steiner, E. Pugh, I. R. Walker, S. R. Julian, P. Monthoux, G. G. Lonzarich, A. Huxley, I. Sheikin, D. Braithwaite, and J. Flouquet, "Superconductivity on the border of itinerant-electron ferromagnetism in UGe_2," *Nature*, vol. 406, pp. 587–592, Aug. 2000.

[36] U. Karahasanovic, F. Krüger, and A. G. Green, "Quantum order-by-disorder driven phase reconstruction in the vicinity of ferromagnetic quantum critical points," *Phys. Rev. B*, vol. 85, p. 165111, Apr 2012.

[37] J. Bardeen, L. N. Cooper, and J. R. Schrieffer, "Microscopic theory of superconductivity," *Phys. Rev.*, vol. 106, pp. 162–164, Apr 1957.

[38] G. Goll, *Unconventional superconductors: experimental investigation of the order-parameter symmetry*. Springer Verlag, 2006.

[39] L. H. Greene, "High-temperature superconductors: Playgrounds for broken symmetries," *AIP Conference Proceedings*, vol. 795, no. 1, pp. 70–82, 2005.

[40] Quantum Desing, *PPMS hardware manual*.

[41] R. Bachmann, J. F. J. DiSalvo, T. H. Geballe, R. L. Greene, R. E. Howard, C. N. King, H. C. Kirsch, K. N. Lee, R. E. Schwall, H.-U. Thomas, and R. B. Zubeck, "Heat capacity measurements on small samples at low temperatures," *Review of Scientific Instruments*, vol. 43, no. 2, pp. 205–214, 1972.

[42] P. F. Sullivan and G. Seidel, "Steady-state, ac-temperature calorimetry," *Phys. Rev.*, vol. 173, pp. 679–, Sept. 1968.

[43] M. I. Eremets, *High Pressure Experimental Methods*. Oxford University Press Inc., New York, 1996.

[44] D. Walker, D. Carpenter, and C. Hitch, "Some simplifications to multianvil devices for high pressure experiments," *American Mineralogist*, vol. 75, pp. 1020–1028, 1990.

[45] J. Xu, H. Mao, R. Hemley, and E. Hines, "The moissanite anvil cell: a new tool for high-pressure research," *J. Phys.: Condens. Matter*, vol. 14, pp. 11543–11548, 2002.

[46] A. Jayaraman, "Diamond anvil cell and high-pressure physical investigations," *Reviews of Modern Physics*, vol. 55, pp. 65–108, 1983.

[47] D. Moroni, *Unconventional Magnetism and Quantum Criticality in the Hexagonal Laves Phase $NbFe_2$*. PhD thesis, Royal Holloway University of London, 2006.

[48] P. Bridgman, "The resistance of 72 elements, alloys and compounds to 100,000 kg cm^{-2}," *Proceedings of the American Academy of Arts and Sciences*, vol. 81, p. 165, 1952.

[49] N. Lotter and J. Wittig, "10 GPa pressure cell for the investigation of high-T_c superconductors," *Journal of Physics E: Scientific Instruments*, vol. 22, no. 7, p. 440, 1989.

[50] H. Hall, *High pressure methods in High temperature technology.* McGraw-Hill, 1960.

[51] F. Bundy, *Modern Very High Pressure Techniques.* Butterworth, London, 1962.

[52] P. Seiden, "Pressure dependence of the superconducting transition temperature," *Physical Review*, vol. 179, pp. 458–462, 1969.

[53] J. Franck and W. Johnson, "Pressure dependence of the energy gap of superconductiong Pb," *Physical Review Letters*, vol. 20, pp. 379–381, 1969.

[54] B. Bireckoven and J. Wittig, "A diamond anvil cell for the investigation of superconductivity under pressures of up to 50 GPa: Pb as a low temperature manometer," *Journal of Physics E: Scientific Instruments*, vol. 21, no. 9, p. 841, 1988.

[55] A. Eiling and J. S. Schilling, "Pressure and temperature dependence of electrical resistivity of Pb and Sn from 1-300k and 0-10 GPa-use as continuous resistive pressure monitor accurate over wide temperature range; superconductivity under pressure in Pb, Sn and In," *Journal of Physics F: Metal Physics*, vol. 11, no. 3, p. 623, 1981.

[56] T. Smith, S. Chu, and M. Maple, "Superconducting manometers for high pressure measurement at low temperature," *Cryogenics*, vol. 9, p. 53, 1969.

[57] P. L. Alireza and S. R. Julian, "Susceptibility measurements at high pressures using a microcoil system in an anvil cell," *Review of Scientific Instruments*, vol. 74, no. 11, pp. 4728–4731, 2003.

[58] D. D. Jackson, C. Aracne-Ruddle, V. Malba, S. T. Weir, S. A. Catledge, and Y. K. Vohra, "Magnetic susceptibility measurements at high pressure using designer diamond anvils," *Review of Scientific Instruments*, vol. 74, no. 4, pp. 2467–2471, 2003.

[59] P. L. Alireza and G. G. Lonzarich, "Miniature anvil cell for high-pressure measurements in a commercial superconducting quantum interference device magnetometer," *Review of Scientific Instruments*, vol. 80, no. 2, p. 023906, 2009.

[60] A. S. Ruetschi and D. Jaccard, "Adaptation of the Bridgman anvil cell to liquid pressure mediums," *Review of Scientific Instruments*, vol. 78, p. 123901, Dec. 2007.

[61] L. G. Khvostantsev, V. N. Slesarev, and V. V. Brazhkin, "Toroid type high-pressure device: History and prospects," *High Pressure Research*, vol. 24, p. 371, 2004.

[62] N. Môri, T. Nakanishi, M. Ohashi, N. Takeshita, H. Goto, o. S. Yom, and Y. Okayama, "A technique for precise magneto-transport measurements at low temperatures under pressure up to 8 GPa.," *Physica B*, vol. 265, p. 263, 1999.

[63] T. Nakanishi, N. Takeshita, and N. Môri, "A newly developed high-pressure cell by using modified bridgman anvils for precise measurements in magnetic fields at low temperatures.," *Review of Scientific Instruments*, vol. 73, p. 1828, 2002.

[64] E. Colombier and D. Braithwaite, "Simple adaptation of the bridgman high pressure technique for use with liquid media," *Review of Scientific Instruments*, vol. 78, p. 093903, 2007.

[65] A.-S. Rüetschi, *High pressure, quasi-hydrostaticity and multiprobes: instrumental development and studies of organic conductors and the $LaAlO_3/SrTiO_3$ interface.* PhD thesis, Université De Genève, 2009.

[66] T. Itou, K. Kanoda, K. Murata, T. Matsumoto, K. Hiraki, and T. Takahashi, "Collapse of charge order in a quasi-one-dimensional organic conductor with a quarter-filled band.," *Physical Review Letters*, vol. 93, p. 216408, 2004.

[67] S. Ramakrishnan, S. Sudaram, R. Pandit, and G. Chandra, "An AC susceptometer from 1.5 to 300 K," *J. Phys. E: Sci. Instrum*, vol. 28, p. 650, 1985.

[68] G. E. Bacon and J. Crangle, "Chemical and magnetic order in platinum-rich Pt+Fe alloys," *Proceedings of the Royal Society of London. Series A. Mathematical and Physical Sciences*, vol. 272, pp. 387–405, Mar. 1963.

[69] Y. Tsunoda, D. Tsuchiya, and Y. Higashiyama, "Crossover of spin correlations in $Pt_{100-x}Fe_x$ (16 <= x ¡= 25) alloys," *Journal of the Physical Society of Japan*, vol. 72, pp. 713–717, Mar. 2003.

[70] S. Yano and Y. Tsunoda, "Simple cubic antiferromagnet Pt_3Fe alloy under uniaxial pressure," *Journal of Magnetism and Magnetic Materials*, vol. 310, pp. 1841–1843, Mar. 2007.

[71] N. Kourov *Soviet Physics - JETP*, vol. 52, p. 969, 1980.

[72] J. Crangle, "Magnetic susceptibility of the alloy Pt3Fe between 20 and 900 degrees absolute," *Nature*, vol. 181, pp. 644–645, Mar. 1958.

[73] H. Okabe, S. Yano, T. Muranaka, and J. Akimitsu, "Magnetic and structural phase transitions in Mo_3Sb_7," *Journal of Physics: Conference Series*, vol. 150, no. 5, p. 052196, 2009.

[74] Z. Bukowski, D. Badurski, J. Stepien-Damm, and R. Troc, "Single crystal growth and superconductivity of Mo_3Sb_7," *Solid State Communications*, vol. 123, no. 6, pp. 283–286, 2002.

[75] V. M. Dmitriev, L. F. Rybaltchenko, L. A. Ishchenko, E. V. Khristenko, Z. Bukowski, and R. Tro, "Energy gap and upper critical field of the new magnetic superconductor Mo_3Sb_7 found by the andreev reflection method," *Superconductor Science and Technology*, vol. 19, no. 6, p. 573, 2006.

[76] V. H. Tran, A. D. Hillier, D. T. Adroja, and Z. Bukowski, "Muon-spin-rotation study of the superconducting properties of Mo_3Sb_7," *Phys. Rev. B*, vol. 78, p. 172505, Nov 2008.

[77] V. Tran, W. Miller, and Z. Bukowski, "Low-temperature specific heat of the superconductor Mo_3Sb_7," *Acta Materialia*, vol. 56, pp. 5694–5700, Nov. 2008.

[78] C. Candolfi, B. Lenoir, A. Dauscher, C. Bellouard, J. Hejtmánek, E. Šantavá, and J. Tobola, "Spin fluctuations and superconductivity in Mo_3Sb_7," *Phys. Rev. Lett.*, vol. 99, p. 037006, Jul 2007.

[79] A. Junod, T. Jarlborg, and J. Muller, "Heat-capacity analysis of a large number of $A15$-type compounds," *Phys. Rev. B*, vol. 27, pp. 1568–1585, Feb 1983.

[80] V. H. Tran and Z. Bukowski, "Synthesis and characterization of the superconductor Mo_3Sb_7," *Acta Physica Polonica A*, vol. 114, p. 67, 2008.

[81] V. H. Tran, R. T. Khan, P. Wisniewski, and E. Bauer, "Pressure-induced spin-density-wave transition in superconducting Mo_3Sb_7," *ArXiv e-prints*, July 2009.

[82] W. J. Duncan, O. P. Welzel, D. Moroni-Klementowicz, C. Albrecht, P. G. Niklowitz, D. Gruner, M. Brando, A. Neubauer, C. Pfleiderer, N. Kikugawa, A. P. Mackenzie, and F. M. Grosche, "Quantum phase transitions in $NbFe_2$ and $Ca_3Ru_2O_7$," *Physica Status Solidi B-basic Solid State Physics*, vol. 247, pp. 544–548, Mar. 2010.

[83] J. M. Zeleya, S. Gama, C. A. Ribiero, and G. Effenberg, "The iron-niobium phase diagram," *Z. Metallkd*, vol. 84, no. 5, pp. 160–164, 1993.

[84] W. Brckner, K. Kleinstck, and G. E. R. Schulze, "Atomie arrangement in the homogeneity range of the Laves phases $ZrFe_2$ and $TiFe_2$," *Phys. Stat. Sol. (b)*, vol. 23, no. 2, pp. 475–480, 1967.

[85] A. W. Smith, J. A. Rogers, and R. D. Rawlings, "The homogeneity range and defect structure of the laves phase $NbFe_2$," *phys. stat. sol. (a)*, vol. 15, no. 2, pp. K119–K122, 1973.

[86] A. W. Smith and R. D. Rawlings, "A Mössbauer effect study of the laves phase $NbFe_2$," *phys. stat. sol. (a)*, vol. 22, no. 2, pp. 491–499, 1974.

[87] M. Shiga and Y. Nakamura, "Magnetic properties of stoichiometric and off-stoichiometric $NbFe_2$," *Journal of the Physical Society of Japan*, vol. 56, no. 11, pp. 4040–4046, 1987.

[88] Y. Yamada and A. Sakata, "Weak antiferromagnetism in $NbFe_2$," *Journal of the Physical Society of Japan*, vol. 57, pp. 46–49, 1988.

[89] M. R. Crook and R. Cywinski, "Magnetic transitions in $Nb_{1y}Fe_{2+y}$," *Journal of Magnetism and Magnetic Materials*, vol. 140-144, pp. 71–72, 1995.

[90] Y. Yamada, H. Nakamura, Y. Kitaoka, K. Asayama, K. Koga, A. Sakata, and T. Murakami, "NMR study of weak antiferromagnetism in $NbFe_2$," *Journal of the Physical Society of Japan*, vol. 59, no. 8, pp. 2976–2985, 1990.

[91] M. Brando, D. Moroni-Klementowicz, C. Albrecht, and F. Grosche, "Quantum criticality in $NbFe_2$," *Physica B: Condensed Matter*, vol. 378380, pp. 111–112, May 2006.

[92] M. R. Crook and R. Cywinski, "Spin fluctuations and magnetic order in $Nb_{1x}Zr_xFe_2$," *Hyperfine Interactions*, vol. 85, pp. 203–208, 1994. 10.1007/BF02069422.

[93] T. D. Haynes, I. Maskery, M. W. Butchers, J. A. Duffy, J. W. Taylor, S. R. Giblin, C. Utfeld, J. Laverock, S. B. Dugdale, Y. Sakurai, M. Itou, C. Pfleiderer, M. Hirschberger, A. Neubauer, W. Duncan, and F. M. Grosche, "Ferrimagnetism in Fe-rich $NbFe_2$," *Phys. Rev. B*, vol. 85, p. 115137, Mar 2012.

[94] A. Subedi and D. J. Singh, "Band structure and itinerant magnetism in quantum critical $NbFe_2$," *Phys. Rev. B*, vol. 81, p. 024422, Jan 2010.

[95] Y. Yamada, J. Armitage, R. Graham, and P. Riedi, "Pressure dependence of magnetic properties of $Nb_{1-y}Fe_{2+y}$," *Journal of Magnetism and Magnetic Materials*, vol. 104107, Part 2, no. 0, pp. 1317 – 1318, 1992. ¡ce:title¿Proceedings of the International Conference on Magnetism, Part II¡/ce:title¿.

[96] C. Albrecht, *High Pressure Study of Magnetic Quantum Phase Transitions in $NbFe_2$ and $Ca_3Ru_2O_7$*. PhD thesis, Royal Holloway, University of London, 2008.

[97] A. Neubauer, J. Boeuf, A. Bauer, B. Russ, H. v. Lohneysen, and C. Pfleiderer, "Ultra-high vacuum compatible image furnace," *Review of Scientific Instruments*, vol. 82, no. 1, p. 013902, 2011.

[98] J. Inoue and M. Schimizu, "Electronic structure and magnetic properties off-stoichiometric $NbFe_2$," *Journal of Magnetism and Magnetic Materials*, vol. 79, pp. 265–269, 2004.

[99] M. Palumbo and P. Muzikar, "Magnetic-field-induced superconductivity," *EPL (Europhysics Letters)*, vol. 20, no. 3, p. 267, 1992.